Université de Montréal

Topology, Quantum Dots, and Open Systems

—

Probing topological edge states via the decoherence dynamics of quantum dots

par

Nicolas Delnour

Département de Physique
Faculté des arts et des sciences

Mémoire présenté en vue de l'obtention du grade de
Maître ès sciences (M.Sc.)
en Physique

25 août 2021

Université de Montréal

Faculté des arts et des sciences

Ce mémoire intitulé

Topology, Quantum Dots, and Open Systems

—

Probing topological edge states via the decoherence dynamics of quantum dots

présenté par

Nicolas Delnour

a été évalué par un jury composé des personnes suivantes :

William Witczak-Krempa
(président-rapporteur)

Richard MacKenzie
(directeur de recherche)

Philippe St-Jean
(membre du jury)

Résumé

Nous proposons, par voie théorique, une sonde ayant la capacité de détecter et de caractériser les états de surface d'une chaîne Su-Schrieffer-Heeger (SSH). Cette sonde consiste d'un qubit interagissant avec un environnement, et exploite le phénomène de la décohérence afin de retirer de l'information sur l'environnement. Une approximation de faible couplage permet de démontrer analytiquement que le taux de décohérence du qubit est proportionnel à la densité d'états locale de l'environnement. Dans le cas d'un environnement possédant des états discrets, une mesure de la densité d'états locale peut être équivalente à une mesure de l'amplitude d'un état, permettant donc une caractérisation spatiale des états de l'environnement. Un système tripartite consistant d'un qubit couplé à une chaîne SSH discrète muni de canaux conducteurs aux extrémités est étudié afin de valider l'utilité de la sonde pour inférer et caractériser les états de surface. L'espace des paramètres de la sonde est discuté en détail. En étudiant l'impact du couplage des canaux conducteurs, nous notons l'émergence d'états de type-surface sur des sites interdits ainsi que dans des phases topologiques ne supportant pas d'états de surface dans le modèle SSH isolé. Ces excitations, que nous appelons *états fantômes*, apparaissent dû à un décalage des frontières de la chaîne SSH.

mots clés : matériaux topologiques, modèle Su-Schrieffer-Heeger (SSH), états de surface, décoherence, qubit, sonde, états émergents

Abstract

We propose a novel probe with the ability to detect topological edge states in low-dimensional materials. This probe, consisting of a qubit interacting with a system of interest, utilizes the dynamics of decoherence to study the qubit's environment. We show analytically that, under a weak-coupling approximation, the decoherence rate of the qubit is proportional to the local density of states of the environment. In studying environments featuring finite subsystems with discrete states, the local density of states mapped by the qubit probe can extract state amplitude profiles, resulting in a full spatial characterization of states. We explicitly study a tripartite system consisting of a qubit coupled to a finite SSH chain with conducting leads attached to each end and demonstrate the probe's ability to infer the presence of, and characterize, edge states. The parameter space of the probe is studied. Notably, we show the lead coupling strength effectively shifts the SSH chain boundaries resulting in emergent edge-type states, dubbed *ghost states*, with support on sites which are forbidden in an isolated SSH chain for a given topological phase.

keywords: topological materials, Su-Schrieffer-Heeger (SSH) model, edge states, decoherence, qubit, probe, emergent excitations and states

Contents

List of Figures

List of abbreviations

BZ	Brillouin Zone
DOS	Density of states
DD	Double (quantum) dot
LDOS	Local density of states
PHS	Particle hole symmetry
SD	Single (quantum) dot
SSH model	Su-Schrieffer-Heeger model
TRS	Time reversal symmetry
TLS	Two-level system (qubit, double quantum dot)

Acknowledgements

As many others probably were, I was thoroughly unprepared for the challenges and difficulties working from home in a pandemic would present. I would be lying if I wrote here that I succeeded in going above and beyond my goals. In truth, I struggled to reconcile my passion for scientific research with the motivational drain that depression combined with social isolation fostered in me. With the end of this degree in sight, and after reflecting on the past two years, I want to express genuine gratitude to the many who helped me complete this journey.

First and foremost, I am profoundly grateful to Richard MacKenzie for the opportunity to learn and work under his supervision. I thank him for his availability and patience in answering my questions. Through many discussions which led to fruitful advances in my research, I found in him a brilliant researcher but also a kind and humble soul. I count myself lucky to have had his support over the course of my degree.

For their invaluable help over dozens of meetings and discussions, I thank our collaborators Hichem Eleuch and Michael Hilke. I also thank Michel Côté and Tami Pereg-Barnea for useful exchanges, as well as the many other professors who inspired me through their teaching on the beauty of the inner workings of our natural world.

To my friends Louis, William, Charles, Alice, Joseph, Oreste, Marc-Antoine, and Louis-Philippe (as ordered by a random sequencer, no favorites here), thank you for sharing your strength with me in moments I had none left. Thank you for the good times, *votre amitié vaut de l'or*.

To my family, thank you for your unconditional love and support over the years.

Introduction

The elemental constituent of a quantum computer is a qubit; a two-state/two-level system possessing quantum behaviour. Coherence can be thought of in the context of waves by defining that two waves are coherent if they share the same frequency and differ only by a constant phase. A more general view in this context is to describe coherence as an ensemble of correlations between the states in a given system. A coherent qubit is one which can, in principle, be used for computation. Once technologically feasible, quantum computers promise a tremendous increase of power and speed compared to conventional classical computers. This speed-up can be attributed to the fact that qubits can exist in a superposition of their two states, resulting in the ability to store vastly more information than classical bits. Unfortunately, open quantum systems, to which qubits are no exception in the real-world, inevitably decay and undergo decoherence. As a result of this, a qubit is reduced, computationally, to nothing more than a classical bit. Designing a quantum computer then becomes a task of slowing down the inevitable: suppressing the decoherence rate to give time for the extraction of meaningful information prior to the destruction of qubit superpositions. Such methods include, but are not limited to, cryogenic cooling for noise reduction and error correction codes. In principle, a purely isolated qubit will remain coherent for an infinite amount of time and decoherence is the direct consequence of interactions with an environment. Works by Leggett *et al.* have shown the substantial impact an environment of bosons or electrons can have on the physics mediating a two-level system [1].

Straying from this pragmatic preamble where we have used notions from the field of quantum computing to introduce decoherence, this work will have at its focus the intimate relationship between the decoherence of a two-level system and its environment. To be concrete, rather than striving to minimize the decoherence rate, we will investigate how the environment affects the decoherence dynamics of a qubit and how these dynamics can be used, in reverse, to probe properties of the qubit's surroundings. In effect, we propose a novel quantum sensor, which we will dub the decoherence probe in this work, which utilizes as its mechanism of action the natural measurement induced from interactions with an environment. As a case study, we will demonstrate the decoherence probe's efficacy as a topological edge state detector.

Efforts toward further miniaturization of technological components has naturally led to an increase in the research of low-dimensional (1-d and 2-d) materials. Due to their constrained dimensions, low-dimensional materials host interesting collective behaviours, some of which are linked to an interplay of topology and wavefunctions [2]. The subject of topological materials (which is not constrained to low-dimensional materials in general) has taken the world of condensed matter physics by storm in the past couple of decades, and this, for good reason; these materials host peculiar states with exotic and interesting properties – topological edge states. It is then natural to ask how one can go about finding real-world signatures of topology through these edge states. Common methods for studying topological edge states include Angle-Resolved PhotoEmission Spectroscopy (ARPES), a powerful method to probe the momentum-space band structure of a material, and charge transport/transmission probes which typically involve a study of the conductance through a sample. Consider the simple case of a transport measurement on a bulk insulator. A large conductance is an indication of non-insulating behaviour – possibly a conducting mode propagating on the edges of the sample [3, 4]. Transmission probes can prove highly useful for studying edge states in lower-dimensional systems but cannot easily discern how the edge states are distributed along the boundaries of a system: for example, no difference is observed in the transmission measurement of a localized mode on the left or right boundary of a 1-d chain [5]. These are the most common methods for probing topological materials but engineered/synthetic materials (or metamaterials) can also feature topological order and offer a much wider variety of probes than condensed matter systems. Such topological metamaterials include cold atom systems [6], topological photonics systems [7, 8, 9], and even mechanical systems [10]. The decoherence probe presented in this work aims to offer superior position-basis diagnostics for low-dimensional (1-d and 2-d) topological materials, and could also be applied to certain synthetic topological materials. For definiteness, we consider the simple topological insulator described by the Su-Schrieffer-Heeger (SSH) model. This 1-d model hosts topological edge states in certain configurations and we will show how the decoherence probe can provide a complete spatial characterization of these states.

This work is structured as follows. In Chapter 1, we introduce the SSH model and give a detailed analysis of single-particle electronic excitations, followed by a discussion of the model's topological features. Chapter 2 is dedicated to notions of decoherence and time evolution of quantum systems. We notably demonstrate a general expression for the decoherence rate of a qubit in the limit of weak coupling to the environment. With the goal of using decoherence dynamics as the mechanism of action for our proposed probe, we create a toy system dubbed the tripartite system in Chapter 3. This tripartite system consists of a qubit coupled to an environment with topological features of interest: a finite SSH chain to which we attach a semi-infinite lead at each end to model an environment. The Green's functions for the combined SSH chain and leads are then derived to obtain explicit analytical

expressions for the decoherence rate of the qubit in this tripartite system. Chapter 4 sees a proof-of-concept application of the decoherence probe to the tripartite system, highlighting the probe's ability to study topological edge states. Further properties of the probe and observed emergent features are discussed. Chapter 5 presents concluding remarks as well as open questions to be addressed in future work.

Chapter 1

The Su-Schrieffer-Heeger Model

The Su-Schrieffer-Heeger (SSH) model, named after the three authors who introduced it in a seminal paper in 1979 to describe conducting polymers [11], has remained relevant for its interesting properties such as the existence of solitons [11, 12] and charge fractionalization [13, 14]. In more recent years, the SSH model has become a paradigm for topological materials [15]; its one-dimensional nature means it is one of the simplest possible examples of a topological insulator and has gained pedagogical merit for these reasons. Fig. 1.1 illustrates an SSH chain.

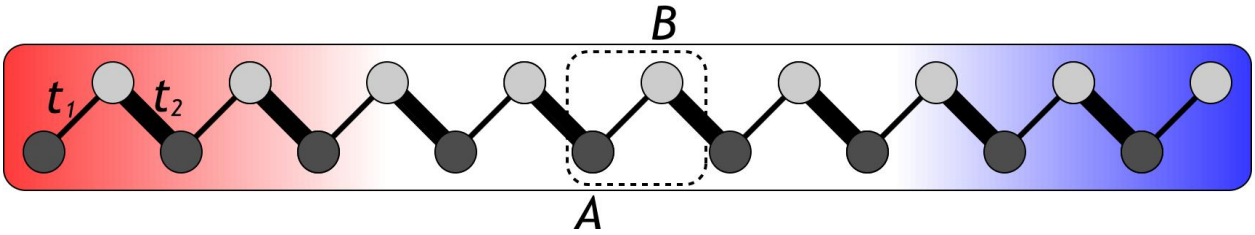

Figure 1.1 – SSH chain for 18 sites with alternate hopping parameters t_1 and t_2. A unit cell is indicated by the dashed region encompassing two sites, with the dark (light) site corresponding to the sublattice site A (B).

1.1. The Hamiltonian, eigenenergies, and eigenstates

In this section, we will study the solutions to the SSH Hamiltonian and analyze features of the model that will be of interest in what follows. The SSH model is a tight-binding model describing a single spinless (or spin polarized) fermion's displacement along a dimerized one-dimensional chain. It is a two-band model typically studied at half-filling such that the Fermi energy is in the gap. In the context of the SSH model, the terms electron and fermion will often be interchanged. The dashed region in Fig. 1.1 is called the unit cell and one could reproduce a chain of any length by translating the dashed region over and over; the unit cell is the periodic structure of the lattice. These unit cells are also referred to as

dimers because the SSH model was originally proposed to describe polyacetylene, a polymer made up of a sequence of dimers. A dimerized material can be viewed as composed of two staggered interlaced sublattices, A and B, as highlighted in Fig. 1.1. The dimerized nature of this model is also often referred to, in the context of tight-binding models, as having staggered hopping amplitudes (i.e. alternating tunneling amplitudes corresponding to the bond strengths from the overlap of neighbouring electronic orbitals along the lattice). This also leads to a distinction between the two hopping parameters; the inter-cell hopping term and the intra-cell hopping term can now be clearly defined.

We choose to not identify a particular hopping parameter t_1 or t_2 to be associated to inter/intra-cell term. This means that while we draw t_1 (t_2) with a thinner (thicker) line, this is not a representation of the strength of inter/intra-cellular hopping parameters. For the simplicity of schematics, an alternate representation of the SSH chain as featured in Fig. 1.2 will be used throughout this work.

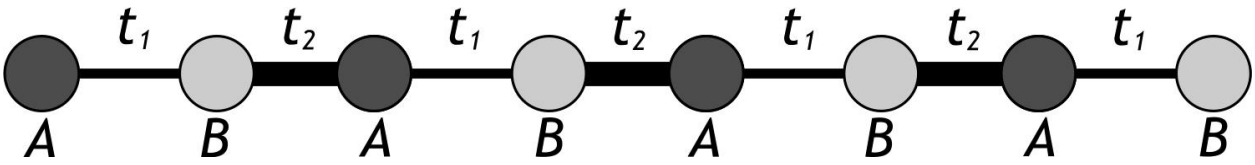

Figure 1.2 – Alternate visualization of an SSH chain for N = 8 with alternate hopping parameters t_1 and t_2 shown by thin and thick lines, respectively. This simpler representation of the model is what will be used for the rest of the work. t_1 and t_2 are considered arbitrary parameters with the possibility of $t_1 > t_2$ or $t_1 < t_2$. The thin and thick lines do not represent the strength of the coupling and only serve as labels for t_1 and t_2.

From here on, we derive well-known results of the SSH model for review, following closely the formalism and approach of a co-authored publication [5]. Unless stated explicitly, this section will consider a finite SSH chain with an even number of sites, N, leading to a discrete energy spectrum. The total number of unit cells will be labelled M; clearly $N = 2M$ to account for the two sites per unit cell. We can write the Hamiltonian described above as

$$H_{\text{SSH}} = t_1 \sum_{m=1}^{M} \Big(|m,B\rangle\langle m,A| + h.c. \Big) + t_2 \sum_{m=1}^{M-1} \Big(|m+1,A\rangle\langle m,B| + h.c. \Big), \tag{1.1.1}$$

for which we will now find the energy eigenvalues and eigenstates. The hopping parameters t_1 and t_2 are assumed real and positive in this work. Converting the SSH Hamiltonian in

matrix form,

$$H_{\text{SSH}} = \begin{pmatrix} 0 & t_1 & & & & \\ t_1 & 0 & t_2 & & & \\ & t_2 & 0 & t_1 & & \\ & & t_1 & 0 & \ddots & \\ & & & \ddots & \ddots & t_1 \\ & & & & t_1 & 0 \end{pmatrix}, \tag{1.1.2}$$

we search for solutions of the Schrödinger equation $(H_{\text{SSH}} - E)\,|\psi\rangle = 0$. Note that, as we are considering here an even chain, t_1 is the first and last hopping parameter. Translational invariance by an even number of sites suggests the following ansatz,

$$|\psi\rangle = \sum_{n=1}^{N} \psi_n |n\rangle = \sum_{m=0}^{M-1} \Big(A|2m+1\rangle + B|2m+2\rangle\Big) e^{i2mk}, \tag{1.1.3}$$

where $m \in \{0,1,...,M-1\}$ denotes the unit cell. A given unit cell m contains two sites denoted by $n \in \{1,...,N\}$ such that $|n_{\text{odd}}\rangle = |2m+1\rangle$ denotes the odd sites and $|n_{\text{even}}\rangle = |2m+2\rangle$ denotes the even sites. A and B are coefficients to be determined, as is the wave number k. The upper bound in (1.1.3) is $M-1$ so the last entry is $e^{i2(M-1)k} = e^{i(N-2)k}$. We can then express the Schrödinger equation as

$$(H_{\text{SSH}} - E)\,|\psi\rangle = \begin{pmatrix} -E & t_1 & & & & \\ t_1 & -E & t_2 & & & \\ & t_2 & -E & t_1 & & \\ & & t_1 & -E & \ddots & \\ & & & \ddots & \ddots & t_1 \\ & & & & t_1 & -E \end{pmatrix} \begin{pmatrix} A \\ B \\ Ae^{i2k} \\ Be^{i2k} \\ \vdots \\ Ae^{i(N-2)k} \\ Be^{i(N-2)k} \end{pmatrix} = 0. \tag{1.1.4}$$

Note that all but the first and last equations in (1.1.4) lead to expressions of the form

$$\begin{aligned} t_1\psi_{n-1} - E\psi_n + t_2\psi_{n+1} &= 0\,, \\ t_2\psi_{n-1} - E\psi_n + t_1\psi_{n+1} &= 0\,, \end{aligned} \tag{1.1.5}$$

for n even and odd, respectively. These will henceforth be referred to as the bulk equations. This system of equations arises from the periodicity of the Brillouin Zone (BZ) over a two-site unit cell. Due to the oscillatory term differing by e^{i2k} for every unit cell, this pair of equations can always be reduced to the following:

$$\begin{aligned} t_2 B - EAe^{i2k} + t_1 Be^{i2k} &= 0, \\ t_1 Ae^{i2k} - EBe^{i2k} + t_2 Ae^{i4k} &= 0. \end{aligned} \tag{1.1.6}$$

Putting this pair in matrix form, we have

$$\begin{pmatrix} -E & t_1 + t_2 e^{-i2k} \\ t_1 + t_2 e^{i2k} & -E \end{pmatrix} \begin{pmatrix} A \\ B \end{pmatrix} = 0. \tag{1.1.7}$$

A nontrivial solution requires the determinant to be equal to zero, which leads us to a simple generalization of the dispersion for a linear tight-binding chain, $E = 2t \cos 2k$:

$$E^2 = (t_1 + t_2 e^{-i2k})(t_1 + t_2 e^{i2k}) = t_1^2 + t_2^2 + 2t_1 t_2 \cos 2k. \tag{1.1.8}$$

The ansatz (1.1.3) is invariant under a phase shift $k \to k + \pi$ so we can choose k to be in the range $(-\pi/2, \pi/2]$. From (1.1.8), there exist positive- and negative-energy solutions which will form two bands. For a given energy solution, (1.1.8) has two equal and opposite solutions for k. We define k to be the positive solution, with all solutions labelled with $\pm k$. The positive and negative bands are symmetric as a result of the chiral symmetry of the Hamiltonian (discussed further in Section 1.2.4). It is useful to take a closer look at the different possible dispersion relations for various values of t_1 and t_2 as can be seen in Fig. 1.3.

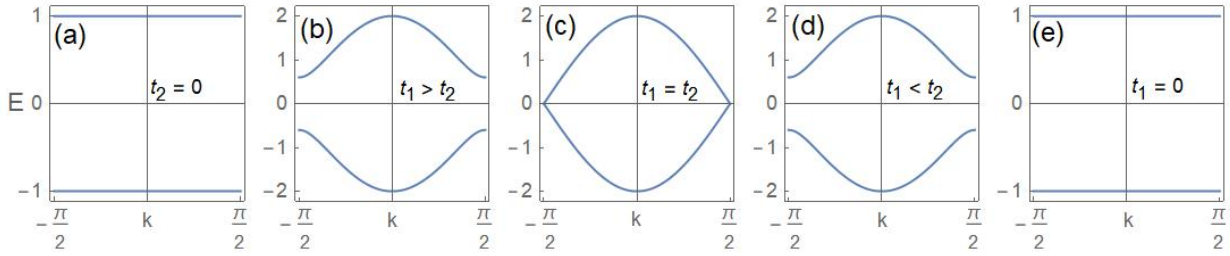

Figure 1.3 – Dispersion relation (1.1.8) for various choices of parameters t_1 and t_2: (a) t_1=1, t_2=0 ; (b) t_1=1.3, t_2=0.7; (c) t_1=1, t_2=1; (d) t_1=0.7, t_2=1.3; (e) t_1=0, t_2=1. We acknowledge this figure is heavily inspired by Fig. 1.2 of [15].

The cases where one of the hopping parameters is set to 0 (Fig. 1.3(a) and Fig. 1.3(e)) breaks the chain down into a series of disconnected dimers. It is of interest to note that the case where t_1=t_2 in Fig. 1.3(c) shows closure of the band gap and describes a conductor due to the crossing of the valence band with the conduction band at $k = \pm\, \pi/2$ (equivalent to a linear tight-binding chain). In order to open the gap, it is clear that $t_1 \neq t_2$ as shown in Fig. 1.3(b) and Fig. 1.3(d); staggered hopping parameters are necessary to describe an insulator. While the staggered hopping parameters can be shown to originate from a Peierls instability as the system attempts to minimize its energy [16], this provides an interesting *post hoc* visualization for the staggering of t_1 and t_2. The energy gap separating the two bands, 2Δ, can be expressed simply in terms of the hopping parameters:

$$\Delta = |t_1 - t_2|. \tag{1.1.9}$$

Returning to the search for the eigenstates, one can see that the following A and B satisfy (1.1.7):

$$\begin{pmatrix} A \\ B \end{pmatrix} = \begin{pmatrix} t_1 + t_2 e^{-i2k} \\ E \end{pmatrix}. \tag{1.1.10}$$

Additionally, the first equality of (1.1.8) allows us to also write

$$(t_1 + t_2 e^{\pm i2k}) = |E| e^{\pm i2\varphi} \tag{1.1.11}$$

by introducing a phase φ where $0 < \varphi < \pi/2$, so (1.1.10) can be written

$$\begin{pmatrix} A \\ B \end{pmatrix} = \begin{pmatrix} |E| e^{-i2\varphi} \\ E \end{pmatrix}. \tag{1.1.12}$$

The above is simplified further by multiplying by $e^{i\varphi}/|E|$ to obtain

$$\begin{pmatrix} A \\ B \end{pmatrix} = \begin{pmatrix} e^{-i\varphi} \\ \pm e^{i\varphi} \end{pmatrix}, \tag{1.1.13}$$

where here and in what follows, the upper (lower) sign corresponds to the solution of positive (negative) energy.

The most general solution $|\psi_\pm\rangle$ is then obtained by substituting (1.1.13) into the ansatz (1.1.3) and combining results for (k, φ) and $(k, \varphi) \to (-k, -\varphi)$, where C_+ and C_- are constants corresponding to the positive and negative solutions of k and φ.

$$\begin{aligned} |\psi_\pm\rangle = \sum_{m=0}^{M-1} \Big\{ &\left(C_+ e^{-i\varphi} e^{i2mk} + C_- e^{i\varphi} e^{-i2mk}\right) |2m+1\rangle \\ &\pm \left(C_+ e^{i\varphi} e^{i2mk} + C_- e^{-i\varphi} e^{-i2mk}\right) |2m+2\rangle \Big\} \end{aligned} \tag{1.1.14}$$

Rewriting the Schrödinger equation (1.1.4) as a matrix eigenvalue equation from (1.1.14), we now solve for C_+ and C_- up to a normalization factor.

$$(H_{\text{SSH}} - E) \begin{pmatrix} C_+ e^{-i\varphi} + C_- e^{i\varphi} \\ \pm(C_+ e^{i\varphi} + C_- e^{-i\varphi}) \\ C_+ e^{-i\varphi} e^{i2k} + C_- e^{i\varphi} e^{-i2k} \\ \pm(C_+ e^{i\varphi} e^{i2k} + C_- e^{-i\varphi} e^{-i2k}) \\ \vdots \\ C_+ e^{-i\varphi} e^{i(N-2)k} + C_- e^{i\varphi} e^{-i(N-2)k} \\ \pm(C_+ e^{i\varphi} e^{i(N-2)k} + C_- e^{-i\varphi} e^{-i(N-2)k}) \end{pmatrix} = 0 \tag{1.1.15}$$

Taking the first and last components of (1.1.15), which will be referred to as the surface/boundary/edge equations, we have

$$\begin{aligned} -E(C_+ e^{-i\varphi} + C_- e^{i\varphi}) \pm t_1(C_+ e^{i\varphi} + C_- e^{-i\varphi}) = 0 \\ \mp E(C_+ e^{i\varphi} e^{i(N-2)k} + C_- e^{-i\varphi} e^{-i(N-2)k}) + t_1(C_+ e^{-i\varphi} e^{i(N-2)k} + C_- e^{i\varphi} e^{-i(N-2)k}) = 0, \end{aligned} \tag{1.1.16}$$

or, in matrix form,

$$\begin{pmatrix} -Ee^{-i\varphi} \pm t_1 e^{i\varphi} & -Ee^{i\varphi} \pm t_1 e^{-i\varphi} \\ \mp Ee^{i\varphi}e^{i(N-2)k} + t_1 e^{-i\varphi}e^{i(N-2)k} & \mp Ee^{-i\varphi}e^{-i(N-2)k} + t_1 e^{i\varphi}e^{-i(N-2)k} \end{pmatrix} \begin{pmatrix} C_+ \\ C_- \end{pmatrix} = 0. \tag{1.1.17}$$

The system of equations (1.1.17) can be considerably simplified using (1.1.11), a relation which will be often used in this work, yielding

$$\begin{pmatrix} e^{i\varphi}e^{-i2k} & e^{-i\varphi}e^{i2k} \\ e^{-i\varphi}e^{iNk} & e^{i\varphi}e^{-iNk} \end{pmatrix} \begin{pmatrix} C_+ \\ C_- \end{pmatrix} = 0. \tag{1.1.18}$$

Again, a nontrivial solution requires taking the determinant and setting it equal to zero. Using (1.1.11), and defining the ratio of hopping parameters $r \equiv t_1/t_2$, we find the following transcendental expression (from here on we will use the shorthand notation $\sin(Ak) = s_A$):

$$rs_{N+2} + s_N = 0. \tag{1.1.19}$$

The quasi-momenta k satisfying the above relation, inserted in (1.1.8), return the discrete energies of the finite SSH chain; the edge equations lead to a discrete energy spectrum, as opposed to infinite SSH chains with no boundary conditions which feature continuous energy bands. Moving towards explicit solutions to the Schrödinger equation, we can see from (1.1.18) that the constants C_+ and C_- can be written

$$\begin{pmatrix} C_+ \\ C_- \end{pmatrix} = \begin{pmatrix} e^{-i\varphi}e^{i2k} \\ -e^{i\varphi}e^{-i2k} \end{pmatrix}, \tag{1.1.20}$$

which in (1.1.14) gives, after some simplification,

$$|\psi_\pm\rangle = \sum_{m=0}^{M-1} \left\{ \sin\left[(2m+2)k - 2\varphi\right] |2m+1\rangle \pm \sin\left[(2m+2)k\right] |2m+2\rangle \right\}. \tag{1.1.21}$$

Again, the sign $\pm$ acting on even sites corresponds to positive- and negative-energy solutions. Note in the above that the shorthand notation for the sine wave was omitted to avoid confusion with the variables k and φ. Expanding the exponential of $\sin[(2m+2)k-2\varphi]$ for $m = N/2$ we find the exact boundary condition given in (1.1.19) and therefore $\sin[(N+2)k-2\varphi] = 0$. This implies that $2\varphi{=}(N+2)k \bmod \pi$ and we find that $\sin[(2m+2)k-((N+2)k \bmod \pi)]{=}\sin[(N-2m)k \bmod \pi]$. Here, $\bmod \pi$ at most changes the sign, which turns out to be the sign of $\sin(Nk)$ so (1.1.21) becomes

$$\left|\psi_\pm^{\text{bulk}}\right\rangle = \sum_{m=0}^{M-1} \left\{ sgn(s_N) s_{N-2m} |2m+1\rangle \pm s_{2m+2} |2m+2\rangle \right\}. \tag{1.1.22}$$

These position-basis solutions are oscillatory and will be referred to as bulk states. Bulk states describe the conventional condensed matter plane-wave solutions on a periodic lattice.

They can come in symmetric or antisymmetric forms and, due to the chiral-symmetric band structure, will always come in $\pm E$ pairs. An example of two bulk states is shown in Fig. 1.4.

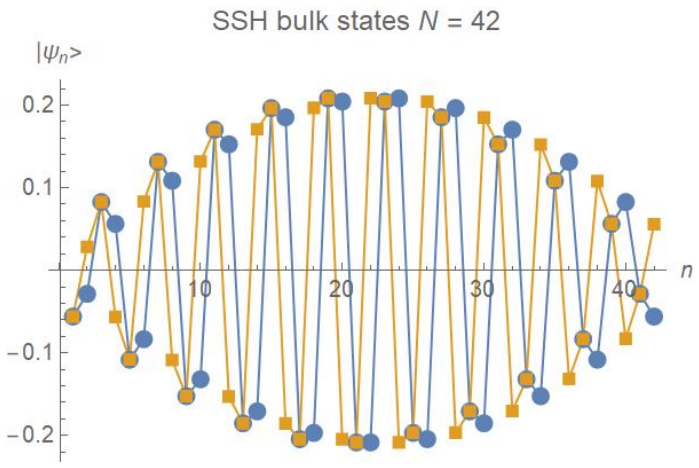

Figure 1.4 – A pair of SSH bulk states for $N = 42$. As expected, the electrons are delocalized throughout the bulk.

1.1.1. Counting more carefully

Let us verify the eigensolutions found above represent a complete set of solutions and see in what instances this completeness fails. As H_{SSH} is an $N \times N$ Hamiltonian, it is expected that N solutions are required for a complete set. The number of eigensolutions can be seen by examining (1.1.19) as a function of k, assumed real for the moment, and determining the number of solutions. While (1.1.19) cannot be solved analytically, graphical solutions are straightforward as can be seen in Fig. 1.5 where $N = 6$. The relation (1.1.19) clearly depends on the parameter r and, as we will see, so do the number of solutions. Let us define here a parameter r_C on which the number of solutions depends:

$$r_C = \frac{N}{N+2}. \tag{1.1.23}$$

This expression is demonstrated in [17] but was rederived independently in [5]. For $r > r_C$, as is shown in Fig. 1.5(a), there are N solutions in the range $(-\pi/2,\pi/2)$. Thus, we have a complete set of solutions corresponding to pairs of energy eigenstates with states described by (1.1.22).

On the other hand, if $r < r_C$, we find two fewer solutions, as illustrated in Fig. 1.5(b). Missing solutions can be found by allowing k to take complex values of the form $k = \pi/2 + i\kappa$ and substituting into (1.1.19). We find κ must satisfy

$$r = \frac{\sinh(N\kappa)}{\sinh((N+2)\kappa)}. \tag{1.1.24}$$

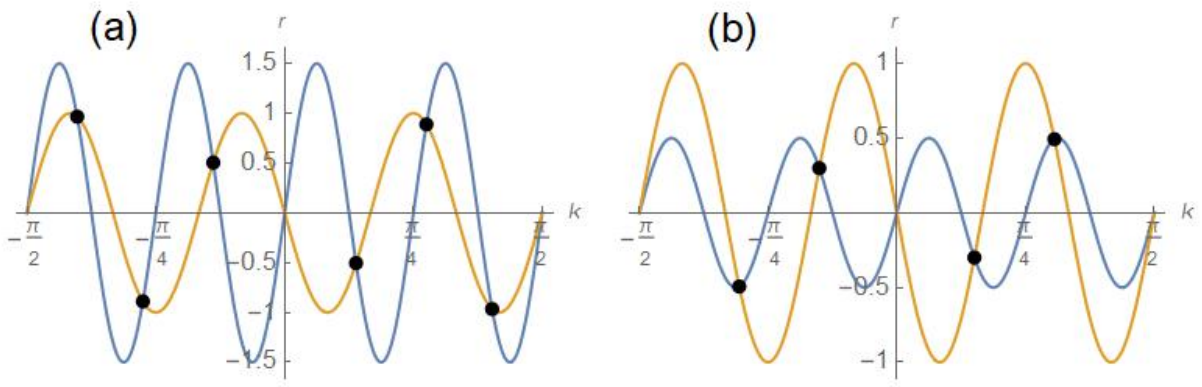

Figure 1.5 – Graphical solutions to the boundary condition (1.1.19) for $N = 6$. The blue curve is $r\sin((N+2)k)$ and the orange curve is $\sin(Nk)$. The case for $r > r_C$ is shown in (a) and $r < r_C$ in (b).

It can be seen that there exist two solutions for $r < r_C$ and none if $r > r_C$; combined with the bulk solutions mentioned above, we get a total of N solutions, as expected. Using $k = \pi/2 + i\kappa$, with κ defined as the positive solution of (1.1.24), and substituting this into the ansatz (1.1.3), the new solutions for $r < r_C$ can be rewritten in a form similar to (1.1.22). As these states are expressed with hyperbolic sines and are exponentially confined to the chain boundaries, they will be referred to as edge states. We adopt the shorthand notation $\sinh(A\kappa) \to sh_A$.

$$\left|\psi_{\pm}^{\text{edge}}\right\rangle = \sum_{m=0}^{M-1} (-1)^m \left\{ sh_{N-2m}|2m+1\rangle \pm sh_{2m+2}|2m+2\rangle \right\} \tag{1.1.25}$$

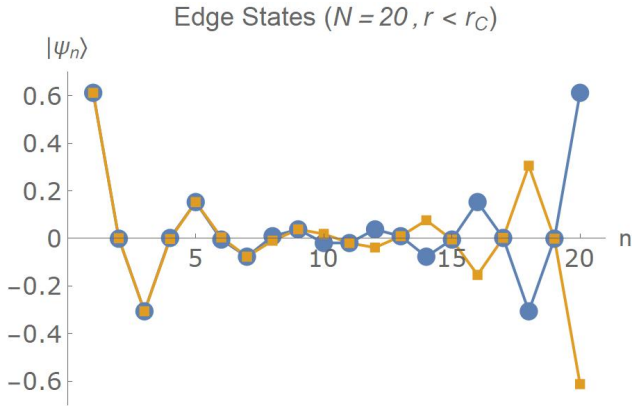

Figure 1.6 – Edge states for a finite SSH chain of length $N = 20$, as described by (1.1.25).

Thus, certain configurations of an even-N SSH chain lead to the emergence of boundary features described by imaginary wavenumbers. In particular, we have found a critical parameter r_C given in (1.1.23) which distinguishes the topological phases of an even-N SSH

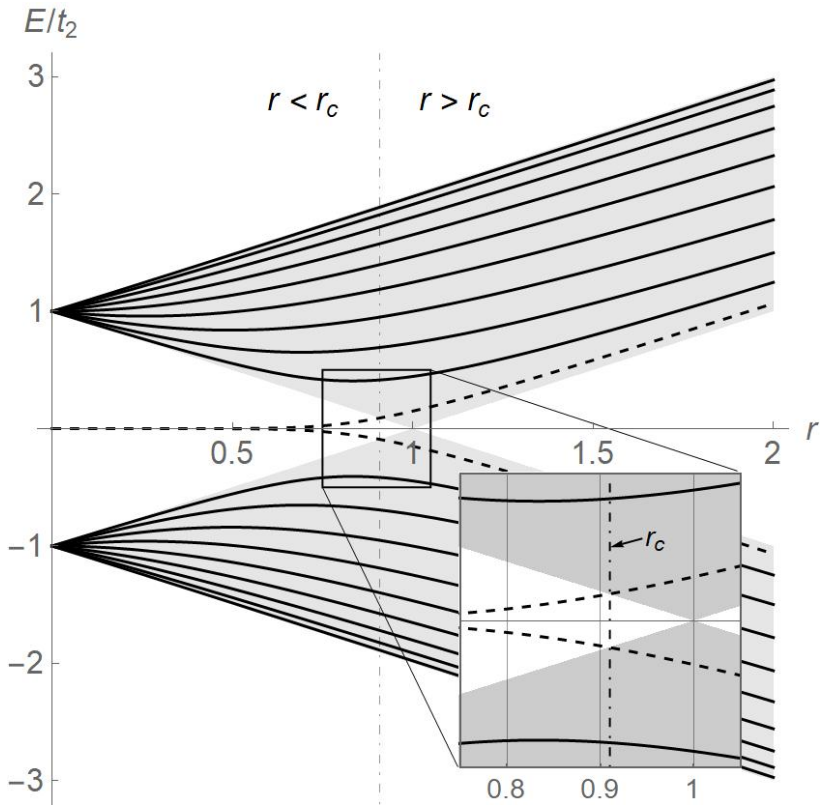

Figure 1.7 – Energy spectrum as a function of r for an SSH chain of length $N = 20$. Note that, as made clear by the magnified inset, the topological phase transition for a finite SSH chain at $r = r_C$ occurs precisely when the dashed line exits the bulk-band region of an infinite SSH chain.

chain and serves as a criteria for the existence of edge states. The pair of edge states existing simultaneously for $r < r_c$ is shown in Fig. 1.6. Note how these edge states come in a symmetric and anti-symmetric pair corresponding to positive and negative energy solutions, respectively. Looking closely, it can be seen that these states have nonzero amplitude for odd sites on the left side of the chain while they are nonzero for even sites on the right edge. These states therefore appear confined to the odd sublattice on the left but hybridize in the bulk and then tend to confinement on the even sublattice on the right edge. This behaviour will be explained in more detail in Section 1.2.4 where the implications of chiral symmetry in the SSH model will be discussed.

With all these fascinating results said and done, we have not yet addressed the energies of these edge states. Recall that we found the dispersion relation (1.1.8) from the bulk Hamiltonian to characterize the energies of bulk states and found a gapped spectrum compatible with an insulator. An approximate expression for the energy of edge states is obtained from (1.1.24) for small r and/or large N (i.e. the limit of very localized states) which yields an

expression for κ which can be substituted in the dispersion relation, yielding

$$E_{\text{edge}} \sim 0 \pm t_2 r^{N/2}\left(1-r^2\right) + \mathcal{O}\left(r^N\right). \tag{1.1.26}$$

Note that the energy tends to zero exponentially with N, indicating that edge states arising on finite even-length chains have small but non-zero energies. The full energy spectrum as a function of r for $N = 20$ is shown in Fig. 1.7, adapted from [5]. Solid lines here represent bulk states while dashed lines represent bulk states which transition to edge states. A vertical dashed line indicates the hopping parameter ratio at which a topological phase transition occurs, $r = r_C$, and the shaded regions show the bands in the thermodynamic limit $N \to \infty$. Perhaps the most important feature, highlighted in the inset in Fig. 1.7, is the departure of states represented by dashed lines from the thermodynamic bulk and tending towards zero energy as r decreases. This crossing from bulk to edge states occurs at $r = r_C$.

1.1.2. Odd-N SSH chain

Expressions for states satisfying the Schrödinger equation of an odd-N SSH chain are obtained similarly to the even-N case and will be presented in less detail below. As N is odd, the final hopping parameter in H_{SSH} becomes t_2 and we write $N = 2M + 1$. Naturally, this implies the odd-parity chain cannot be described by a sequence of complete unit cells. The ansatz (1.1.3) then becomes

$$|\psi\rangle = \sum_{n=1}^{N} \psi_n |n\rangle = \sum_{m=0}^{M} \Big(A|2m+1\rangle + B|2m+2\rangle\Big) e^{i2mk}, \tag{1.1.27}$$

with the condition that $|2M+2\rangle = |N+1\rangle = 0$. The Schrödinger equation can be written

$$\left(H_{\text{SSH}} - E\right)|\psi\rangle = \begin{pmatrix} -E & t_1 & & & & & \\ t_1 & -E & t_2 & & & & \\ & t_2 & -E & t_1 & & & \\ & & t_1 & -E & \ddots & & \\ & & & \ddots & \ddots & t_2 & \\ & & & & t_2 & -E & \end{pmatrix} \begin{pmatrix} A \\ B \\ Ae^{i2k} \\ Be^{i2k} \\ \vdots \\ Be^{i(N-3)k} \\ Ae^{i(N-1)k} \end{pmatrix} = 0. \tag{1.1.28}$$

From the bulk equations, one finds the same dispersion relation (1.1.8). Introducing a phase as defined by (1.1.11), the constants A and B are also identical to the even-N chain. The boundary equations are now

$$\begin{pmatrix} t_2 e^{i\varphi} e^{-i2k} & t_2 e^{-i\varphi} e^{i2k} \\ t_1 e^{i\varphi} e^{i(N-1)k} & t_1 e^{-i\varphi} e^{-i(N-1)k} \end{pmatrix} \begin{pmatrix} C_+ \\ C_- \end{pmatrix} = 0, \tag{1.1.29}$$

where imposing $\det(M) = 0$ yields the following relation which the quasi-momenta k must satisfy:

$$s_{N+1} = 0. \tag{1.1.30}$$

It is easy to verify numerically that the above always has $N-1$ solutions in the interval $(-\pi/2, \pi/2]$. Note that, unlike (1.1.23), this relation is independent of both t_1 and t_2. Additionally, we find from (1.1.29) constants $C_\pm$ identical to the even-N case which yield the following bulk solutions:

$$\left|\psi_\pm^{\text{bulk}}\right\rangle = \sum_{m=0}^{M} \left\{ \left(t_1 s_{2m+2} + t_2 s_{2m}\right)|2m+1\rangle \pm E s_{2m+2}|2m+2\rangle \right\} \quad (N \text{ odd}). \tag{1.1.31}$$

As has just been mentioned, there exist $N-1$ bulk solutions. The missing solution is easily found recalling the SSH model features a symmetric spectrum due to chiral symmetry; eigenvalues must always come in $\pm E$ pairs so, for an odd number of solutions, the last mode is constrained to the only energy that conserves this symmetry and gets pinned to the mid-gap at zero energy. Imposing $E = 0$ in the Schrödinger equation (1.1.28), we find that odd- and even-site terms decouple, with boundary terms which yield $B = 0$. The zero energy solution therefore has support on odd sites only. We find, up to normalization, the following solution for zero-modes:

$$\left|\psi_0^{\text{edge}}\right\rangle = \sum_{m=0}^{M} \left(\frac{-t_1}{t_2}\right)^m |2m+1\rangle = \sum_{m=0}^{M} (-r)^m |2m+1\rangle \quad (N \text{ odd}). \tag{1.1.32}$$

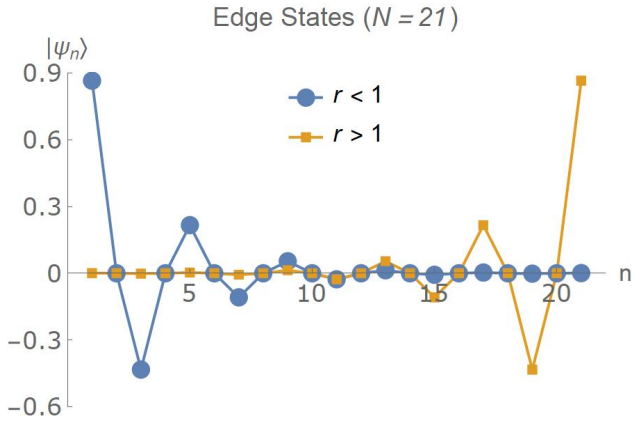

Figure 1.8 – Edge states for a finite SSH chain of length $N = 21$, as described by (1.1.32).

Evidently from the above, $\left|\psi_0^{\text{edge}}\right\rangle$ describes a mode localized at the boundaries of the SSH chain; for all $r \neq 1$, there exists a single edge state on the left (right) if $r < 1$ ($r > 1$),

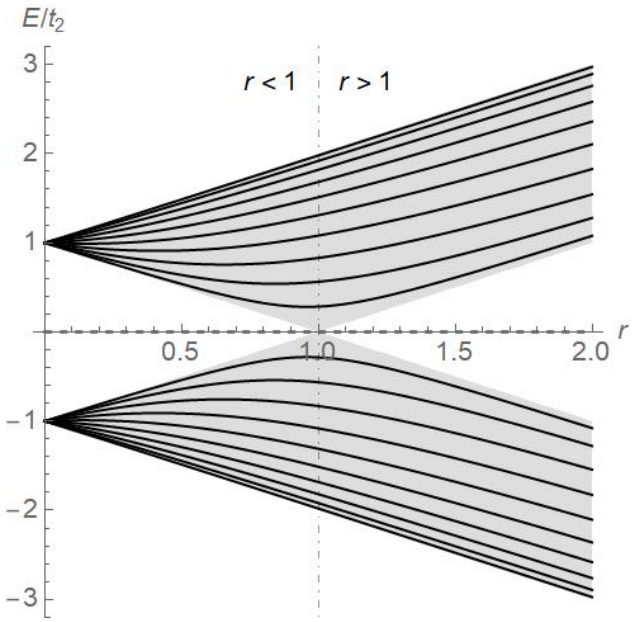

Figure 1.9 – Energy spectrum as a function of r for an SSH chain of length $N = 21$. Note that, unlike the even-N chain, there always exists a localized state except at the critical transition parameter, $r = 1$, where the state crosses the thermodynamic bulk.

as can be seen in Fig. 1.8 for an SSH chain of length $N = 21$. While this purely exponential localization is valid for $E = 0$, a feature of the odd-N-chain edge state, one notices a near-exponential behaviour for the previously discussed even-N chain edge states when the energy is sufficiently small (i.e. $E \to 0$). The full energy spectrum in Fig. 1.9 confirms previous findings, with the dashed line representing the edge state always confined to the mid-gap for all values of r. As before, the solid lines represent bulk states and the shaded region shows the bulk bands in the thermodynamic limit.

1.1.3. Summary of the finite SSH model solutions

We have seen that certain configurations of an SSH chain lead to the appearance of edge states. Whereas for N even r_C marks the transition between zero or two edge states, for N odd $r = 1$ marks the transition between a left and right edge state. The distinction of N being even or odd is therefore of paramount importance in our prediction of edge states for finite SSH chains. In both cases, the hopping parameter ratio $r = t_1/t_2$ serves as a useful quantity to define the topological phases and classify the resulting states. We summarize the results for even-N and odd-N SSH chains below.

N even
with $r_C = \frac{N}{N+2}$
— $r > r_C$; N bulk solutions and no edge states
— $r < r_C$; N-2 bulk solutions and 2 edge states

N odd
$\forall\ r$ there exist $N-1$ bulk solutions and 1 zero-energy edge state
— $r < 1$, left edge state
— $r > 1$, right edge state

Thus far, we have discussed the solutions to the SSH model and have found that distinct edge states can arise for certain topological phases. It turns out that topology is a useful tool to quantify, classify, and describe these states, commonly referred to as topological edge states. The alert reader will note the words *topology* and *topological* have been sprinkled around with no justification. We now provide a foundation for this vocabulary.

1.2. Topology in Condensed Matter Physics

The field of topological materials arguably came into existence with the discovery of the quantum Hall effect, where conducting electrons travel along the periphery of a two-dimensional bulk insulator subject to a magnetic field in plateaus of quantized conductance due to the system's momentum-space topological structure [18]. These electronic states are called topological surface states or topological edge states, and behave differently than states occupying the bulk. These behaviours have fascinated the condensed matter physics community and, in recent years, the field has grown significantly both on the theoretical and experimental fronts. Topological materials are a classification of materials that can feature topological states: states confined to exist on the system boundaries (edges, perimeter, surface) which are robust to deformations and disorder [19]. There is a rich diversity of such materials ranging from topological superconductors to topological insulators [20, 21] and considerable technological interest in these materials has arisen due to the robustness of surface states. Depending on the model, edge states are predicted to yield emergent quasiparticles with exotic properties such as Majorana zero-modes [22], which are anti-particle partners to themselves, and helical Dirac fermions [23], which behave as massless relativistic particles.

The SSH model is one of the simplest Hamiltonians we can write which exhibits topological features. For this reason, many texts use the SSH model as an example while introducing notions of topology in condensed matter physics. Inspired heavily by the first chapter of [15],

I will directly discuss the topology of the SSH model, presenting necessary concepts of topological materials as we go. The purpose of this section, although not central to the remainder of this thesis, is to understand the implications of topology in condensed matter physics.

1.2.1. An illustration of the topological properties of the SSH model

As we have seen, solutions to the SSH model feature not only bulk modes but highly localized modes at the boundaries of the chain, called edge modes. While these states have been introduced by finding missing solutions when considering only real wavenumbers, there is a much deeper topological justification to the existence of these states called the bulk-boundary correspondence. The correspondence shows that, while edge states are distinct from bulk states, they emerge from bulk properties. An elementary proof of this correspondence applied to the SSH model can be found in [24]. We will begin work below with an even ($N = 2M$) finite SSH chain in the thermodynamic limit (N large). For this particular section, it is advantageous to reexpress H_{SSH} in the more conventional bra-ket formalism:

$$H_{\text{SSH}} = t_1 \sum_{m=1}^{M} \Big(|m,B\rangle\langle m,A| + h.c. \Big) + t_2 \sum_{m=1}^{M-1} \Big(|m+1,A\rangle\langle m,B| + h.c. \Big) \tag{1.2.1}$$

Recall that m is the unit cell index with M being the total number of unit cells. Additionally, recall that we have labelled the sublattice sites A and B. As in the matrix form of H_{SSH}, we can see here that the hopping parameter t_1 then mediates intra-cell hopping of the fermion, while t_2 is the hopping parameter between unit cells – the inter-cell hopping parameter. Note the upper bound $M - 1$ on the inter-cell hopping term required to not *hop out of the chain*.

Of importance for what follows, we note that we are dealing with two Hilbert spaces: $|m, A\,(\text{or}\,B)\rangle = |m\rangle \otimes |A\,(\text{or}\,B)\rangle$. The internal degree of freedom here is the sublattice index A or B, while the external degree of freedom is the unit cell index m such that our system is of the form $\mathcal{H}_{\text{external}} \otimes \mathcal{H}_{\text{internal}}$. Due to the translational invariance of the unit cells in the bulk from Bloch's theorem [25], we can express the external degree of freedom in the plane wave basis (up to normalization) as

$$|m\rangle = \sum_k e^{i2mk} |k\rangle, \tag{1.2.2}$$

such that

$$|m\rangle \otimes |A\,(\text{or}\,B)\rangle \to \sum_k e^{i2mk} |k\rangle \otimes |A\,(\text{or}\,B)\rangle, \tag{1.2.3}$$

which explicitly gives for the bulk (periodic boundary) Hamiltonian;

$$
\begin{aligned}
H_{\text{SSH}} &= \sum_k \Big\{(t_1 + t_2 e^{i2k})|k,A\rangle\langle k,B| + (t_1 + t_2 e^{-i2k})|k,B\rangle\langle k,A|\Big\}, \\
\text{separating reps.} &\rightarrow |k\rangle\langle k| \otimes \Big((t_1 + t_2 e^{i2k})|A\rangle\langle B| + (t_1 + t_2 e^{-i2k})|B\rangle\langle A|\Big).
\end{aligned}
\tag{1.2.4}
$$

We can therefore write the bulk Hamiltonian in the following compact form by defining the 2×2 matrix $\mathcal{H}(k)$;

$$
H_{\text{SSH}} = \sum_k |k\rangle\mathcal{H}(k)\langle k| \qquad \text{with} \quad \mathcal{H}(k) = \begin{pmatrix} 0 & t_1 + t_2 e^{i2k} \\ t_1 + t_2 e^{-i2k} & 0 \end{pmatrix}. \tag{1.2.5}
$$

In expressing $|m\rangle$ in the plane wave basis, a factor of 2 is present in the exponential because we have chosen $k \in (-\pi/2, \pi/2]$. The astute reader will note that $\mathcal{H}(k)$ seems familiar; it is exactly the bulk Hamiltonian found in the Schrödinger equation (1.1.7). Let us reexpress $\mathcal{H}(k)$ in terms of Pauli matrices, $\boldsymbol{\sigma} = (\sigma_x, \sigma_y, \sigma_z)$.

$$
\begin{aligned}
\mathcal{H}(k) &= \boldsymbol{h}(k) \cdot \boldsymbol{\sigma} \\
h_x(k) &= t_1 + t_2 c_{2k} \\
h_y(k) &= -t_2 s_{2k} \\
h_z(k) &= 0
\end{aligned}
\tag{1.2.6}
$$

As $\mathcal{H}(k)$ is periodic over the BZ, one can ask how $\boldsymbol{h}(k)$ behaves as we sweep k through the BZ. The obvious answer is that $\boldsymbol{h}(k)$ will form a closed loop in momentum space due to the Hamiltonian's periodicity and continuity in the BZ. Looking at the form of $\boldsymbol{h}(k)$ above, we see a map to a circle on the plane $\mathbb{R}^2$ punctured at the origin. The origin is excluded because $\boldsymbol{h}(k) = 0$ would imply $t_1 = t_2 = 0$, which is a trivial solution, or $t_1 = t_2$, which closes the band gap at $k = \pi/2$ and no longer describes the insulating SSH model. We will see in Section 1.2.3 that selecting a trajectory $\boldsymbol{h}(k)$ passing through the origin will result in the breaking of a symmetry fundamental to the SSH model. Example trajectories of $\boldsymbol{h}(k)$ are plotted in Fig. 1.10(a) and (b). Note how for $t_1 > t_2$ the circle does not enclose the origin while for $t_1 < t_2$, $\boldsymbol{h}(k)$ winds around the origin. As will be shown shortly, by counting the number of times one winds around the hole at the origin, one can define a topological invariant which will serve to characterize edge states.

1.2.2. Berry phases

Phases in quantum mechanics are often considered unimportant in that a global phase factor will not affect the physical observables of a system. A notable exception to this rule are geometric phases, or Berry phases [26]. Much like in the Aharonov-Bohm effect where a phase originating from a magnetic vector potential $\boldsymbol{A}$ leads to physical observables [27], it is

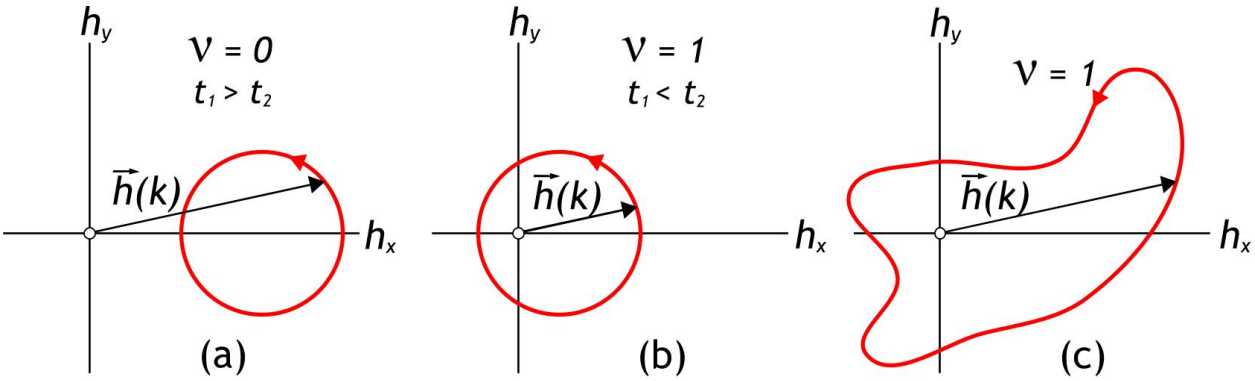

Figure 1.10 – Winding of the bulk Hamiltonian vector $\vec{h}(k)$ through the Brillouin zone for: (a) $t_1 > t_2$ where the trajectory does not encompass the origin, (b) $t_1 < t_2$ where $\vec{h}(k)$ winds around the origin, (c) case with $t_1 < t_2$ for some arbitrary smooth/adiabatic deformation showing winding around the origin exactly once as $\vec{h}(k)$ sweeps the BZ.

possible to define physical geometric phases for topological systems by studying the winding of the Hamiltonian through the BZ. These phases can hold different names for different dimensionalities but of interest to our 1-d system is the Zak phase (or the winding number, which is the Zak phase divided by π) [15].

We will digress a bit on the SSH model to give background on geometric phases following [26]. To begin, we define a Hamiltonian $H(\mathbf{R})$ which depends on parameters $\mathbf{R} = (R_1,\, R_2,...)$. The idea will be to study what happens as $\mathbf{R}$ moves adiabatically along a contour $\mathcal{C}$ in parameter space. The time-independent Schrödinger equation for a discrete state $|\phi_n(\mathbf{R})\rangle$ can be written

$$H(\mathbf{R})|\phi_n(\mathbf{R})\rangle = E_n(\mathbf{R})|\phi_n(\mathbf{R})\rangle. \tag{1.2.7}$$

Now considering that $\mathbf{R}$ is tracing a contour in parameter space $\mathbf{R}(t)$ with adiabatic state evolution given by $|\psi(t)\rangle = e^{-i\theta(t)}|\phi_n(\mathbf{R}(t))\rangle$, where $\theta(t)$ is the time evolution phase, we can write the time-dependent Schrödinger equation

$$H(\mathbf{R}(t))|\psi(t)\rangle = i\frac{d}{dt}|\psi(t)\rangle, \tag{1.2.8}$$

which we reexpress with instantaneous solutions as

$$E_n(\mathbf{R}(t))|\phi_n(\mathbf{R}(t))\rangle = \left(\frac{d\,\theta(t)}{dt}\right)|\phi_n(\mathbf{R}(t))\rangle + i\frac{d}{dt}|\phi_n(\mathbf{R}(t))\rangle. \tag{1.2.9}$$

Taking the scalar product with $\langle\phi_n(\mathbf{R}(t))|$ and then integrating with respect to time, we find the following expression for the dynamical phase $\theta(t)$.

$$\theta(t) = \int_0^t E_n\left(\mathbf{R}\left(t'\right)\right)dt' - i\int_0^t \left\langle \phi_n\left(\mathbf{R}\left(t'\right)\right)\left|\frac{d}{dt'}\right|\phi_n\left(\mathbf{R}\left(t'\right)\right)\right\rangle dt' \tag{1.2.10}$$

In the above, while the first term is obvious, the second term comes as a surprise. The second term is the Berry phase, or in 1-d the Zak phase, labelled γ_n. We can express our

time-evolved state in terms of the Berry/Zak phase as

$$|\psi(t)\rangle = \exp\Big\{ -i\int_0^t E_n(\mathbf{R}(t'))dt'\Big\}\exp\Big\{i\gamma_n(t)\Big\}|\phi_n(\mathbf{R}(t))\rangle. \tag{1.2.11}$$

Eliminating the explicit temporal dependence of the integral in (1.2.10) and replacing it with the variation in parameter space $d\mathbf{R}$, we have

$$\gamma_n = i\int_{\mathbf{R}(0)}^{\mathbf{R}(t)} \langle\phi_n(\mathbf{R})\,|\nabla_{\mathbf{R}}|\,\phi_n(\mathbf{R})\rangle\, d\mathbf{R}. \tag{1.2.12}$$

The Berry potential, defined as the integrand of (1.2.12), is written $\boldsymbol{A}_n(\mathbf{R}) = i\langle\phi_n(\mathbf{R})\,|\nabla_{\mathbf{R}}|\,\phi_n(\mathbf{R})\rangle$. Now that we have defined the geometric phase and its associated potential, let us find γ_n for the SSH model considering the parameter $\mathbf{R} \to k$ as it moves along a closed contour in momentum space.

We have already found the eigenvector solutions to the bulk SSH Hamiltonian earlier; see (1.1.12). Note that the only parameter here is φ which in turn depends on k. We will rewrite the solution slightly differently here including a normalization factor;

$$|\phi_k^{\pm}\rangle = \frac{1}{\sqrt{2}}\begin{pmatrix} \pm e^{-i2\varphi(k)} \\ 1 \end{pmatrix}, \quad \text{with} \quad \varphi(k) = \frac{1}{2}\arctan\left(\frac{t_2\sin 2k}{t_1 + t_2\cos 2k}\right). \tag{1.2.13}$$

The closed-loop path through parameter space of interest here is the cyclic winding of the wavenumber k as it sweeps through the BZ. We study the valence band $|\phi_k^-\rangle$ of the SSH model for definiteness (the $|\phi_k^+\rangle$ band would give the same result up to a sign). Recall that when discussing the band structure of the SSH model, k was defined such that $-\pi/2 < k \leq \pi/2$. We therefore write

$$\gamma_n = i\int_{-\pi/2}^{\pi/2}\langle\phi_k^-|\frac{d}{dk}|\phi_k^-\rangle dk = \int_{-\pi/2}^{\pi/2}\frac{d\varphi(k)}{dk}dk, \tag{1.2.14}$$

and so, because our integrand is symmetric,

$$\gamma_n = 2\int_0^{\pi/2}\frac{t_2^2 + t_1t_2\cos 2k}{t_1^2 + t_2^2 + 2t_1t_2\cos 2k}dk \tag{1.2.15}$$

$$= \left[k + \arctan\left(\frac{(t_1+t_2)\cot(k)}{t_1 - t_2}\right)\right]\Bigg|_0^{\pi/2}. \tag{1.2.16}$$

In the above, we evaluate the lower integration bound $k = 0$ as a limit approaching 0^+ such that the cotangent tends to ∞. Evaluating both bounds, we are then left with

$$\gamma_n = \pi/2 - \arctan\Big(sgn(t_1 - t_2)\infty\Big) = \begin{cases} 0 & \text{if } t_1 > t_2 \\ \pi & \text{if } t_1 < t_2 \\ \text{undefined} & \text{if } t_1 = t_2 \end{cases} \tag{1.2.17}$$

Note that the Zak phase is undefined when $t_1 = t_2$ at the closure of the gap. The phase $\gamma_n = 0$, for $t_1 > t_2$, is called the topologically trivial phase and leads to $e^{i\gamma_n} = 1$ in the time-evolved state (1.2.11). The nontrivial topological phase $\gamma_n = \pi$ occurs when $t_2 > t_1$ and leads to a term $e^{i\gamma_n} = -1$. This geometric phase is of importance and serves as a topological invariant distinguishing distinct phases ($t_1 > t_2$ or $t_1 < t_2$) of a system. The Zak phase has been experimentally validated in an engineered cold-atom SSH analog, confirming this dual topological nature [28]. As was mentioned previously, the winding number ν is often the quantity evoked to highlight the topological nature of the SSH model. This winding number is simply the Zak phase divided by π, such that $\nu = 0$ is the topologically trivial phase and $\nu = 1$ is the nontrivial phase as shown in Fig. 1.11.

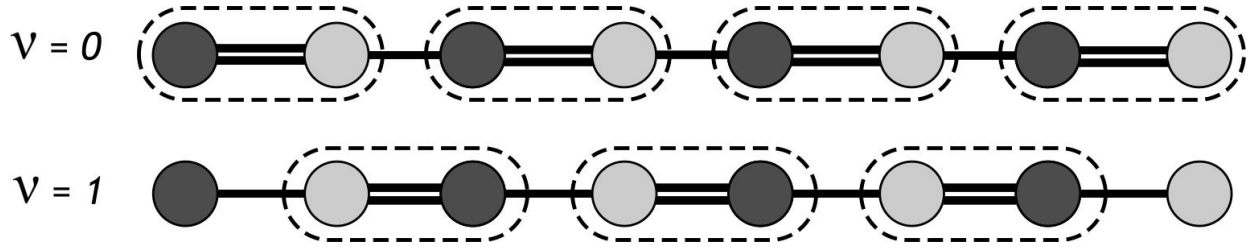

Figure 1.11 – The two topologically distinct phases of an $N = 8$ SSH chain. Note here the different schematic representation of hopping parameters with a double (single) bond indicating the larger (smaller) hopping parameter. We keep the convention of t_1 being the first hopping term. The upper chain is therefore in a trivial topological phase with $t_1 > t_2$ labelled by $\nu = 0$ while the chain below shows a nontrivial topological phase with $t_1 < t_2$ and $\nu = 1$.

This invariant effectively counts the number of times the bulk-momentum-space Hamiltonian vector $\boldsymbol{h}(k)$ winds around holes in its manifold: as one sweeps through all k of the BZ, ν keeps count of the number of times the origin is encircled. As can be seen in Fig. 1.10(a) and (b), the topologically trivial case with $\nu = 0$ never encloses the origin, while the topological phase $\nu = 1$ always wraps around the origin exactly once. SSH edge states arise (for N even in the thermodynamic limit) when $\nu = 1$ and disappear for $\nu = 0$ with the phase transition at $r = 1$ (as $r_C \to 1$ for $N \to \infty$). We also derived for finite systems that, taking N even, a topological phase transition occurs at $r_C = \frac{N}{N+2}$ with support for edge states when $r < r_C$. We further note that, in general, a topological invariant can be defined even if the contour $\boldsymbol{h}(k)$ is out of the plane. Simply put, this can be done by taking the projection of the contour onto the x-y plane and imposing the same criteria of a winding about the origin [29] (this is useful for the addition of on-site σ_z terms, or for considering next-nearest neighbour hopping terms). While the appearance of topological edge states seems to *randomly* coincide with the winding number, a purely bulk-related property, formal and robust proofs of the bulk-boundary correspondence have shown that the two quantities are intimately linked. The existence of these edge states can therefore be tied to this bulk topological invariant

ν in what is known as the bulk-boundary correspondence where bulk properties result in emergent boundary features which are dependent yet distinct of the bulk features.

The topological aspect comes from the fact that while smooth deformations may change the Berry potential locally, these deformations do not affect the value of the integral over the entire BZ. In the *cliché* example; even though a coffee mug and a doughnut appear very different locally, a closed-path integral on the manifold should count the same numbers of holes and hence a mug and doughnut are topologically equivalent. This can be understood visually from Fig. 1.10(c) considering how the trajectory of $\boldsymbol{h}(k)$ is affected by deformations; while the path may no longer be a perfect circle, small changes to $\boldsymbol{h}(k)$ will still trace a closed loop that encloses (or not) the origin.

There is a noteworthy difference in the adiabatic phases introduced by Berry and the topological phases/invariants we are dealing with: in the case of conventional adiabatic Berry phases, it is required that the sweep of parameter space be done slowly in time (at a rate slower than the relaxation rate of the system, such that the system can be described by the instantaneous Schrödinger equation) [26]. On the other hand, the topological invariants we find are independent of time and depend on another type of smoothness – the smoothness of the manifold on which the contour is closed. As such, the deformations are not necessarily time dependent and most often refer to static changes of the Hamiltonian. It is the puncture at the origin of momentum space which, in our topological context, is equivalent to a sharp deformation and where the topological invariant is undefined. Of course, if one imagines an idealized lab system with a "knob" which can modify the appropriate parameters to induce a topological phase transition, then for our characterization of the phases to hold, this deformation must ultimately be adiabatic as our entire description of the physics in the SSH chain relies on the assumption that the system can be described by the instantaneous Schrödinger equation. The important point here is that smooth deformations to our system within a given phase will not jeopardize the existence of edge states as they are described by topological invariants. This leads to the robustness of edge states – where their topological nature protects them against the injection of disorder into the system and/or deformations [15]. We note here that the topological invariant ν as described by (1.2.17) is a property of the bulk-periodic SSH Hamiltonian. To treat disordered configurations where translational invariance is lost, one must resort to more complex invariants such as in [30], where a covariant real-space description of the topological invariant ν is detailed and where it is found that ν (for AIII class models, which includes the SSH model) remains quantized when disorder is turned on up to a certain critical disorder strength. Alternatively, the topology of a model can be characterized using the self-energy in disorder-averaged Green's function descriptions in disordered systems [31, 32]. Robustness to disorder is discussed further in the following section in the context of chiral symmetry.

1.2.3. Chiral symmetry and topological phases

We have just proven the existence of distinct topological phases in the SSH model. We expect that a phase transition will involve a sharp deformation (topologically speaking), as is required to justify distinct phases. Indeed, it appears the only way to go from one phase to another is to force $\boldsymbol{h}(k)$ to take an undefined trajectory passing by the origin ($t_1 = t_2$), closing the SSH model's gap. Obviously, forcing the system through $t_1 = t_2$, the SSH model reduces to a simple linear chain. In the context of passing $\boldsymbol{h}(k)$ trajectories through the origin, the topological phase can be understood as the twisting/exchange of the SSH model bands in going from one phase to another. Therefore, the phase transition cannot occur smoothly and justifies distinct phases.

Rather than focusing on continuous deformations of the system's parameters, let us consider how discrete symmetries play a role in topological phase transitions. In particular, we will focus on an important symmetry for the SSH model: chiral symmetry. We define a unitary chiral symmetry operator, $\hat{\mathcal{C}}^2 = 1$, as anti-commuting with the single particle Hamiltonian (1.1.7) and satisfying the relation $\hat{\mathcal{C}}\hat{\mathcal{H}}(k)\hat{\mathcal{C}} = -\hat{\mathcal{H}}(k)$. It is seen that $\hat{\mathcal{C}} = \sigma_z$ satisfies this relation. The anti-commutator is easy to evaluate and confirms that chiral symmetry is a symmetry of our system:

$$\begin{gathered}\hat{\mathcal{C}}\{\hat{\mathcal{C}}, \hat{\mathcal{H}}(k)\} = \hat{\mathcal{C}}^2\hat{\mathcal{H}}(k) + \hat{\mathcal{C}}\hat{\mathcal{H}}(k)\hat{\mathcal{C}} = \hat{\mathcal{H}}(k) - \hat{\mathcal{H}}(k) = 0 \\ \therefore \{\hat{\mathcal{C}}, \hat{\mathcal{H}}(k)\} = 0\end{gathered} \tag{1.2.18}$$

Note that, contrary to the usual canonical commutation relation, we consider the anti-commutator above. This requirement is the result of not working in the fermionic Fock space as well as considering an effective single-particle bulk description of the Hamiltonian, $\hat{\mathcal{H}}(k)$, rather than the full second quantized Hamiltonian [2, 15, 33]. We note that the SSH model can also satisfy commutation and anti-commutation relations with time reversal symmetry (TRS) and particle hole symmetry (PHS) operators, respectively. While these symmetries do play a role in the topological classification of models such as SSH, the impact of chiral symmetry is most apparent and of relevance to us.

Let us now look at a phase transition that does not close the gap and involves instead chiral symmetry. By considering a deformation lifting the contour $\boldsymbol{h}(k)$ out of the x-y plane, we can link the two phases without closing the gap, i.e. without ever passing through the origin. To do so, an on-site potential of the form $H_{\text{pert}} = u\sigma_z$ is added − a perturbation in z to $\boldsymbol{h}(k)$. One can envision tuning a parameter θ from 0 to π, enforcing $t_1 = 1.5 - \cos\theta$, $t_2 = 1$, and $u = \sin\theta$; this takes the contour at $\theta = 0$ and lifts it out of the x-y plane for increasing θ. We see how at $\theta = \pi$, the contour returns in the plane, but has acquired opposite topological phase due to t_1 now being the larger hopping parameter. As such, we have effectively displaced the contour without ever having to go through the origin – instead, we

have broken chiral symmetry. The anti-commutator of the bulk Hamiltonian and the chiral symmetry operator is satisfied specifically because $\mathcal{H}(k)$ can be expressed solely in terms of σ_x and σ_y. The addition of diagonal σ_z components to $\mathcal{H}(k)$ break chiral symmetry. Even if the transformation is done intelligently, ensuring chiral symmetry is restored after the phase transition (as in the above case where $u = 0$ when $\theta = \pi$), the transition still involves symmetry breaking, making this process non-adiabatic [15]. Topological phases defined by different invariants cannot be smoothly connected and require the closure of the band gap and/or the breaking of a symmetry leading to a topological phase transition. These invariants are therefore of topological nature and classify ensembles of continuously-deformable systems.

These same invariants, through the bulk-boundary correspondence, also infer the existence of robust topological edge states which we have studied in the previous section. In the case of the SSH model, we say that the topological edge states are protected from disorder by chiral symmetry. Disorder can be injected in two principle ways; a disorder in the hopping terms ($\sigma_{x,y}$ dependent, hence preserving chiral symmetry), and an on-site disorder (σ_z perturbation which breaks chiral symmetry). In disordered hopping term configurations, it is found that zero-energy topological edge states are robust up to a critical value of disorder strength [34, 35]. Explicit chiral-symmetry-breaking disorder is touchier and edge states show heightened sensitivity to this type of disorder. This is unsurprising, as the topological modes in the SSH model are said to be protected by chiral symmetry. Interestingly, even in systems with on-site disorder, localization persists up to moderate disorder although the edge states drift away from zero energy for increasing disorder. Furthermore, edge states retain their chiral nature (for weak to moderate disorder) even if the on-site potentials breaks the chiral symmetry of the Hamiltonian [36]. This is the robustness of topological edge states. This powerful property has attracted much attention for its technological applications, namely the proposal of topologically protected quantum computing states introduced in [37] which led to an explosion of research on the topic.

1.2.4. Chiral symmetry and eigenstates of the SSH model

Chiral/sublattice symmetry plays a critical role in the SSH model's description and many topological properties hinge off this symmetry. In particular, this symmetry plays a key role in the energy spectrum's symmetry and on the sublattice confinement of zero-energy states. This section is heavily inspired by [15]. As we have discussed earlier, we define chiral symmetry acting on the bulk single-particle Hamiltonian as $\hat{\mathcal{C}}\hat{\mathcal{H}}(k)\hat{\mathcal{C}} = -\hat{\mathcal{H}}(k)$, implying $\{\hat{\mathcal{C}},\hat{\mathcal{H}}(k)\} = 0$, with $\hat{\mathcal{C}}^2 = 1$. Furthermore, chiral symmetry is a local property of the SSH model as it is a symmetry of every unit cell and $\hat{\mathcal{C}}$ cannot create transitions between unit cells: $\langle m',\alpha'|\hat{\mathcal{C}}|m,\alpha\rangle = 0$ for $m \neq m'$. Because an SSH chain is a periodic sequence of unit

cells, the local chiral operator $\hat{\mathcal{C}}$ is the same in every unit cell. We will work below with the single-particle Hamiltonian $\hat{\mathcal{H}}(k)$, which will be written $\hat{\mathcal{H}}(k) \to \hat{H}$ to lighten the notation.

A feature of chiral-symmetric Hamiltonians we now show is the symmetry of the energy spectrum. Looking at the instantaneous spectrum, $\hat{H}\,|\psi_n\rangle = E_n\,|\psi_n\rangle$, consider the action of $\hat{\mathcal{C}}$ on an eigenstate $|\psi_n\rangle$:

$$\hat{H}\,|\psi_n\rangle = E_n\,|\psi_n\rangle \quad \Longrightarrow \quad \hat{H}\hat{\mathcal{C}}\,|\psi_n\rangle = -\hat{\mathcal{C}}\hat{H}\,|\psi_n\rangle = -\hat{\mathcal{C}}E_n\,|\psi_n\rangle = -E_n\hat{\mathcal{C}}\,|\psi_n\rangle\,. \tag{1.2.19}$$

Therefore, if $|\psi_n\rangle$ is a solution of energy E_n, then $\hat{\mathcal{C}}|\psi_n\rangle$ is a solution of energy $-E_n$. We have just shown the energy spectrum of a chiral-symmetric Hamiltonian must also be symmetric.

We now address which sites a given state has support on based on chiral symmetry arguments. For this, it is useful to define the sublattice projection operators,

$$\hat{P}_A = \frac{1}{2}(\mathbb{1} + \hat{\mathcal{C}})\,; \quad \hat{P}_B = \frac{1}{2}(\mathbb{1} - \hat{\mathcal{C}}). \tag{1.2.20}$$

It is easy to see from $\hat{\mathcal{C}} = \sigma_z$ that

$$\hat{P}_A = \begin{pmatrix} 1 & 0 \\ 0 & 0 \end{pmatrix}; \quad \hat{P}_B = \begin{pmatrix} 0 & 0 \\ 0 & 1 \end{pmatrix}, \tag{1.2.21}$$

where the $\hat{P}_{A,B}$ project the state $|\psi_n\rangle$ on the subspace of sublattices A or B, respectively. We can further express the the chiral symmetry operator as a linear combination of sublattice projection operators as $\hat{\mathcal{C}} = \hat{P}_A - \hat{P}_B$. For states of nonzero energy E_n, $|\psi_n\rangle$ and $\hat{\mathcal{C}}\,|\psi_n\rangle$ must be orthonormal, giving these states equal footing on both sublattice sites:

$$\left\langle \psi_n|\hat{\mathcal{C}}|\psi_n \right\rangle = 0 \qquad \Longrightarrow \qquad \left\langle \psi_n \left|\hat{P}_A\right| \psi_n \right\rangle = \left\langle \psi_n \left|\hat{P}_B\right| \psi_n \right\rangle. \tag{1.2.22}$$

This behaviour is in line with bulk states which have support on both sublattice sites A and B. Perhaps less obvious is the direct agreement with the near-zero energy edge states for N even as shown in Fig. 1.6; even for small energies with states that tend towards sublattice confinement, chiral symmetry still imposes support on any site. Hence, we see that near-zero energy edge states hybridize in the bulk to respect chiral symmetry even if the edges appear confined.

The case of $E_n = 0$ is also of interest for our study of edge states. Projecting such a zero energy state $|\psi_n\rangle$ onto a given sublattice with $\hat{P}_{A,B}$, we see

$$\hat{H}\,|\psi_n\rangle = 0 \qquad \Longrightarrow \qquad \hat{H}\hat{P}_{A,B}\,|\psi_n\rangle = \hat{H}\left(|\psi_n\rangle \pm \hat{\mathcal{C}}\,|\psi_n\rangle\right) = 0. \tag{1.2.23}$$

The above reveals the zero-energy projected eigenstates are additionally eigenstates of $\hat{\mathcal{C}}$. The eigenstates $|\psi_n\rangle$ are therefore chiral symmetric partners to themselves and can be chosen to

have support on a single sublattice A or B. This is supported by Fig. 1.8, showing a zero-energy (N odd) edge state with support only on the odd sublattice. We will refer to this zero-mode behaviour as sublattice confinement in the context of SSH chains.

Chapter 2

Decoherence

Having now studied various types of localized excitations in the SSH model, we can finally introduce the decoherence probe which aims to offer an experimental platform to characterize the aforementioned states. Decoherence is a tricky concept to define and is, as the name suggests, best described by what it is no longer: decoherence is the loss of quantum coherence. Let us unpack this a little further.

2.1. A cursory overview of decoherence

The transition from a quantum to classical description of physics has been a topic of interest since the early days of quantum mechanics [38, 39]. Quantum coherence can be loosely defined as an ensemble of correlations within a system which leads to the superposition of states. In the quantum mechanical context, this coherent interference leads to superposition and therefore probabilistic measurement outcomes. Though not used directly in the upcoming work, it is worthwhile spending a bit of time superficially discussing density matrices to gain an appreciation of decoherence. We consider the evolution of a product state following [40] in this section. Let us define a density matrix ρ for a product state consisting of a subsystem S coupled to an environment with states $|\epsilon\rangle$ with $\mathcal{H}_S \otimes \mathcal{H}_{\text{env}}$ the Hilbert space of the composite system, as

$$\rho = |\psi\rangle\langle\psi| \otimes |\epsilon\rangle\langle\epsilon|. \tag{2.1.1}$$

We will now consider the probability of a transition $|\psi\rangle \to |\phi\rangle$ in the subsystem based on whether an interaction with the environment has happened or not. If the transition occurs prior to any interaction with the environment, the latter plays no role in the dynamics and can be *traced out* (partial trace of ρ over the basis of the environment $\mathcal{H}_{\text{env}}$) to give the reduced density matrix for the subsystem, $\rho_S = |\psi\rangle\langle\psi|$. The transition probability $|\psi\rangle \to |\phi\rangle$ is then expressed as

$$\langle\phi|\rho_S|\phi\rangle = \langle\phi|\psi\rangle\langle\psi|\phi\rangle = \sum_i |\psi_i^*\phi_i|^2 + \sum_{i\neq j} \psi_i^*\psi_j\phi_j^*\phi_i\,, \tag{2.1.2}$$

where ψ_i and ϕ_i are coefficients of $|\psi\rangle$ and $|\phi\rangle$ in the subsystem basis $\mathcal{H}_S$. Note we have diagonal terms as well as the off-diagonal interference terms in the basis of the subsystem $\mathcal{H}_S$. Obviously, with no interaction with the environment the subsystem remains isolated and separable, evolving as a pure state.

Consider next the case where the subsystem and environment interact prior to the transition. The interaction introduces entanglement of the two parts which leads, through environment-induced superselection rules [41], to the new reduced density matrix :

$$\rho_S = \sum_{i,j} \psi_i \psi_j^* \langle \epsilon_j | \epsilon_i \rangle |i\rangle\langle j| = \sum_i |\psi_i|^2 |i\rangle\langle i|, \tag{2.1.3}$$

for orthogonal environment states $\langle \epsilon_j | \epsilon_i \rangle = \delta_{ij}$. These environment-induced superselection rules, often referred to as einselection rules, effectively destroy the antidiagonal interference terms in the subsystem's basis [42], yielding the transition probability

$$\langle \phi | \rho_S | \phi \rangle = \sum_i |\psi_i^* \phi_i|^2. \tag{2.1.4}$$

It is then a consequence of considering interactions with the environment that coherent interference terms disappear in the subspace $\mathcal{H}_S$. The loss of off-diagonal components in the reduced density matrix directly implies that these coherences can no longer be observed. While we say we have loss, coherence is certainly not destroyed. In reality, states in the subsystem basis evolve from pure to mixed states as correlation phases are delocalized into the environment basis through interactions [40, 43]. An observer that only has access to the subsystem sees the partial trace of the full density matrix; even though the full density matrix of the composite system ρ is pure, the reduced density matrix loses purity as a result of entanglement with the environment. In this manner, decoherence can be understood as the loss of purity, with a pure state (or product state) evolving into a mixed state (or entangled state). In either case, it remains that the subsystem decoheres from a pure quantum state to a state where a measurements will no longer be sensitive to all of the originally-present coherences. This restriction on the quantum-like behaviour of a quantum system, which amounts to the loss of coherent interference terms, is what we call decoherence.

An isolated system never experiences decoherence as the correlations are conserved within the system. It is only through a coupling to an environment that this *lossiness* occurs. The nature and specific conditions of the environment we are coupling to should then affect the decoherence dynamics of our system, which begs the question: How is decoherence affected when coupling to environments hosting localized topological states? For definiteness, we study how the decoherence of a two-level system (TLS) is affected by these topological states.

2.2. Interlude on Green's functions

We have briefly introduced decoherence by way of the density matrix formalism but, in the remainder of this thesis, we will use and study Green's functions extensively (time-dependent Green's functions for time evolution as well as energy-dependent Green's functions to derive effective descriptions of complex multi-component systems). For this reason, it is useful to review the relevant properties of these mathematical objects. We follow [44] in this section. Simply put, a Green's function is a solution to the following inhomogeneous differential equation subject to some boundary condition

$$[z - L(\boldsymbol{r})]G(\boldsymbol{r}, \boldsymbol{r}'; z) = \delta(\boldsymbol{r} - \boldsymbol{r}'), \tag{2.2.1}$$

where z is a complex constant and $L(\boldsymbol{r})$ is a time-independent, linear, and Hermitian differential operator. We impose that $L(\boldsymbol{r})$ possesses a complete set of eigenfunctions:

$$L(\boldsymbol{r})\phi_n(\boldsymbol{r}) = \lambda_n \phi_n(\boldsymbol{r}). \tag{2.2.2}$$

These equations look more familiar when expressed by way of vector spaces such that (2.2.1) can be written;

$$[z - L]G(z) = \mathbb{1} \quad , \qquad \text{with} \quad L|\phi_n\rangle = \lambda_n|\phi_n\rangle, \tag{2.2.3}$$

where we have used

$$\begin{aligned} \phi_n(\boldsymbol{r}) &= \langle \boldsymbol{r}|\phi_n\rangle, \\ \delta(\boldsymbol{r} - \boldsymbol{r}')L(\boldsymbol{r}) &\equiv \langle \boldsymbol{r}|L\,|\boldsymbol{r}'\rangle, \\ G(\boldsymbol{r}, \boldsymbol{r}'; z) &\equiv \langle \boldsymbol{r}|G(z)\,|\boldsymbol{r}'\rangle. \end{aligned} \tag{2.2.4}$$

The eigenvalues of a Hermitian operator L are real, hence $G(z)$ is analytic in the complex plane except at points or branches of the real z-axis corresponding to eigenvalues of L. In the continuum limit when z is part of the spectrum of L, $G(z)$ is not well defined along the real-axis due to the branch cut arising in (2.2.3). The side limits approaching the branch cut from the complex plane can be defined but are different from one another, leading to the definition of the retarded (advanced) Green's function as approaching the branch cut from positive (negative) complex values. We work with the retarded Green's function and consider an infinitesimal shift from the real axis, $i\epsilon$, with $\epsilon \to 0^+$. Even in the discrete case, the retarded Green's function is necessary to deal with poles along the real axis. We see that the substitutions $L \to H$ and $z \to E + i\epsilon$ recover the retarded Green's function corresponding to the Schrödinger equation:

$$\begin{aligned} [(E + i\epsilon)I - H]G(E) &= \mathbb{1} \\ G(E) &= [(E + i\epsilon)I - H]^{-1}. \end{aligned} \tag{2.2.5}$$

The above expression of the Green's function will be used extensively in the rest of this work. In what follows, the term $i\epsilon$ is implied even though it is not always explicitly written.

2.2.1. Density of states from $G(E)$

Consider a system with an ensemble of eigenvalues E_n. The distribution of these energies is called the density of states (DOS), $N(E)$, where there are $N(E)dE$ states in the interval $E \to E + dE$. For systems with discrete energy levels, the DOS is expressed as

$$N(E) = \sum_n \delta(E - E_n). \tag{2.2.6}$$

As such, $N(E)$ is a sum of delta functions at the eigenvalues of the system. We will now show that the DOS can be expressed in terms of the Green's function. Considering the Laplace transform of the propagator (where the propagator represents the time evolution of a state), one can show the following form of the Green's function:

$$G(E) = \sum_n \frac{|\phi_n\rangle\langle\phi_n|}{E - E_n + i\epsilon}, \tag{2.2.7}$$

where ϕ_n is required to be a complete orthonormal basis set. Taking the trace of (2.2.7) and using the identity

$$\delta(E - E_n) = -\lim_{\epsilon\to+0^+} \frac{1}{\pi}\mathrm{Im}\frac{1}{E - E_n + i\epsilon}, \tag{2.2.8}$$

a result of the Sokhotski–Plemelj theorem applied to Dirac delta functions [45], allows one to express the DOS in terms of the imaginary trace of the Green's function:

$$-\lim_{\epsilon\to+0} \frac{1}{\pi}\mathrm{Im}\{\mathrm{Tr}\, G(E + i\epsilon)\} = \sum_n \delta(E - E_n) = N(E). \tag{2.2.9}$$

We will heuristically write the above up to a constant as

$$N(E) = -\mathrm{Im}\{\mathrm{Tr}\, G(E)\}. \tag{2.2.10}$$

The DOS for an isolated SSH chain ($N = 21$ and $t_1 = 1.1$, $t_2 = 1/t_1$), obtained by numerically evaluating (2.2.10) using $G(E) = (E - H_{\mathrm{SSH}})^{-1}$ with H_{SSH} defined as (1.1.1), is shown in Fig. 2.1. We point out here that this choice of N, t_1, and t_2 results in level spacings of similar energy to the the band gap giving the impression of the absence of a gap; we stress that the edge state at $E = 0$ is confined at the mid-gap, with states of positive/negative energy taking the form of bulk bands.

We now define and find an expression for the local density of states (LDOS) following [46]. The LDOS, labelled $n(E, x)$, is the density of states at a specific position within the system, which therefore must depend on the amplitudes of states at that position;

$$n(E, x) = \sum_n |\phi_n(x)|^2 \delta(E - E_n). \tag{2.2.11}$$

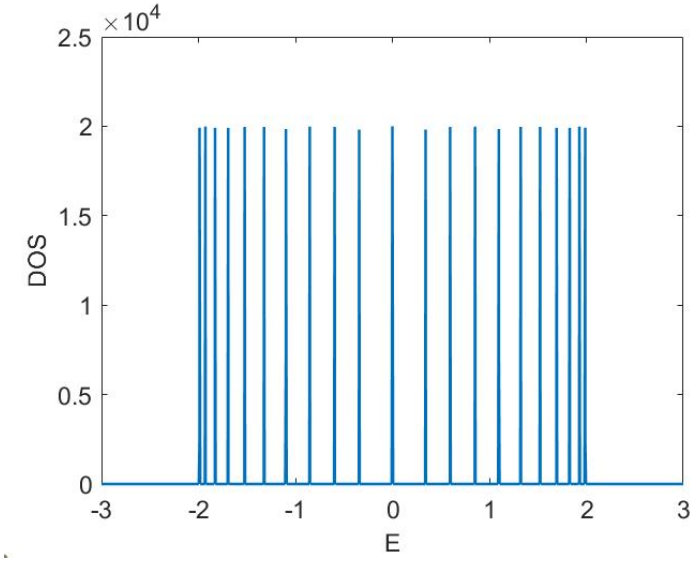

Figure 2.1 – Numerical DOS for a pure SSH chain of length $N = 21$ with $t_1 = 1.1$ and $t_2 = 1/t_1$. Note the peak at $E = 0$ corresponding to the edge state, with nonzero energies corresponding to bulk band states. As we considered a non-interacting and isolated system, the DOS takes the form of delta functions centered at the eigenvalues of the SSH chain. The delta functions do not diverge to infinity due to the energy resolution in the numerical DOS, which would require infinite precision to yield diverging peaks.

Evidently, integration of the LDOS over the whole system must return the DOS, which is easily verified:

$$\int n(E,\, x)dx = \sum_n \delta(E - E_n) \int |\phi_n(x)|^2 dx = N(E). \tag{2.2.12}$$

Above, the normalization condition for states $|\phi_n(x)\rangle$ was used. From (2.2.11), we see that states contribute to the LDOS only where $|\phi_n(x)|^2$ is large. In the case of non-degenerate states, the LDOS gives the profile amplitude of the state. Lastly, by comparison with (2.2.10), we see that

$$n(E,\, x) = -\mathrm{Im}\{G(E,\, x)\}, \tag{2.2.13}$$

where $G(E,x)$ is a diagonal element of the Green's function $G(E)$ corresponding to given position x.

2.2.2. Couplings to environments and broadening

Let us consider a composite system consisting of a finite subsystem coupled to an infinite environment. The environment contains an infinite number of states and leads to a continuous DOS rather than the discrete DOS shown in Fig. 2.1. Looking only at the subsystem, we are neglecting the true DOS of the composite system and in reality are considering the LDOS

integrated over the whole subsystem (which we also call the DOS of the subsystem). Due to hybridization with continuum states from the environment, the subsystem DOS depends both on environment states leaked within the subsystem and the expected subsystem states [47]. These contributions from the environment will lead to broadening in the subsystem DOS, where the broadening is proportional to the coupling with the environment. An SSH chain coupled to two semi-infinite leads, a system we will study in great detail in subsequent chapters (see Fig. 3.1), features broadening and is shown in Fig. 2.2.

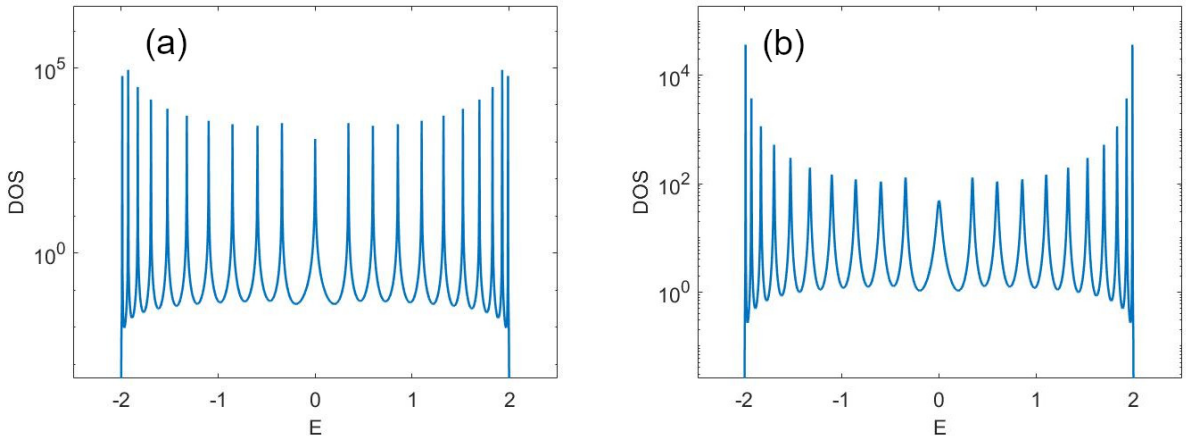

Figure 2.2 – Numerical DOS for an SSH chain of length $N = 21$ with $t_1 = 1.1$ and $t_2 = 1/t_1$ coupled to two semi-infinite leads with coupling parameters $t_L = t_R$ (see Fig. 3.1). We have used a semi-log plot in order to make the broadening more apparent and the relative suppression of certain peaks less drastic. (a) shows the DOS for a coupling strength of $t_L = 0.05$ while for (b) $t_L = 0.25$. As discussed above, coupling to an environment leads to the broadening of the delta functions we previously had. Note the increased broadening and suppression for larger environmental couplings in comparing (a) and (b). See Chapter 3 for a detailed description and treatment of this coupled system.

A final important point, as discussed by [47], is a form of sum rule which states that the total number of states integrated over all energies in the system gives unity. Framed differently, we can say integrating over a broadened peak profile should give the same answer as integrating the delta functions which exists in the isolated system. This implies that, typically, the more a peak is broadened, the more it is suppressed, as can be seen in Fig. 2.2(b) for stronger environment-subsystem coupling in comparison to Fig. 2.2(a). Since the coupled system has finite peaks, we can use the relative peak amplitudes to describe occupation of states in the subsystem.

2.3. Time evolution of an isolated TLS

We begin by studying an isolated two-level system (TLS) for review and comparison purposes. It is worth mentioning that a TLS is a general class of quantum systems and is

equivalent to saying a double quantum dot or a qubit. These terms will be used interchangeably in what follows. We choose to express this Hamiltonian as H_{DD} where the DD (double dot) label is used for concision over H_{TLS} or H_{qubit}. H_{DD} is written in terms of its two basis states $|\epsilon_i\rangle$, $i = 1, 2$, coupled by a parameter τ which is taken to be real and positive:

$$H_{\mathrm{DD}} = \begin{pmatrix} \epsilon_1 & \tau \\ \tau & \epsilon_2 \end{pmatrix}. \tag{2.3.1}$$

The eigenvalues of the above 2×2 matrix, $\lambda_\pm$, are

$$\lambda_\pm = \frac{1}{2}\left(\epsilon_1 + \epsilon_2 \pm \delta\right) = \epsilon_0 \pm \frac{\delta}{2}, \tag{2.3.2}$$

where δ is the energy splitting of the TLS

$$\delta = \sqrt{\left(\epsilon_1 - \epsilon_2\right)^2 + 4\tau^2} = \sqrt{\delta_0^2 + 4\tau^2}. \tag{2.3.3}$$

Above, we have written ϵ_0 as the average energy of the two basis states $(\epsilon_1 + \epsilon_2)/2$ and that we can consider $(\epsilon_1 - \epsilon_2)$ as the energy splitting of the uncoupled basis states which we call δ_0.

With the goal of studying the decoherence of our TLS, we use the time-dependent Green's function to express the probability of a transition; for instance, the probability of the system initially in the state $|\epsilon_1\rangle$ transitioning to $|\epsilon_2\rangle$ at a given later time t is given by [48]

$$P_{1\to 2}(t) = \frac{1}{4\pi^2}\left|G^{12}_{\mathrm{DD}}(t)\right|^2, \tag{2.3.4}$$

with $G^{12}_{\mathrm{DD}}(t)$ the upper-diagonal element of $G_{\mathrm{DD}}(t)$. Much like with the reduced density matrix, the off-diagonal element of the Green's function describes coherences/decoherences. In order to find $G^{12}_{\mathrm{DD}}(t)$, we begin by finding $G^{12}_{\mathrm{DD}}(E)$ which satisfies $G_{\mathrm{DD}}(E) = (E - H_{\mathrm{DD}})^{-1}$. Inversion is straightforward and yields

$$G^{12}_{\mathrm{DD}}(E) = \frac{\tau}{\delta}\left(\frac{1}{E - \lambda_+ + i0^+} - \frac{1}{E - \lambda_- + i0^+}\right). \tag{2.3.5}$$

We then take a Fourier transform adopting a retarded-pole prescription for the residue calculation in order to obtain the retarded ($t > 0$) time-dependent Green's function:

$$\begin{aligned} G^{12}_{\mathrm{DD}}(t) &= \int_{-\infty}^{\infty} dE\, e^{-iEt} G^{12}_{\mathrm{DD}}(E) \\ &= -\frac{2\pi i\tau}{\delta}\left(e^{-i\lambda_+ t} - e^{-i\lambda - t}\right) \\ &= -\frac{4\pi\tau}{\delta} e^{-i\epsilon_0 t}\sin(\delta t/2). \end{aligned} \tag{2.3.6}$$

The result is simply oscillatory, indicating that the TLS transitions periodically between the two states forever with contributions from both frequencies $\lambda_\pm$. It turns out that a purely

periodic time-evolution is a feature of an isolated or closed system; placing the qubit in an environment is what allows decoherence to occur.

2.4. Effective description for a subsystem coupled to environment

We now turn our attention to the study of the time evolution of an open TLS. Recalling the tight-binding models we have worked with previously, we are faced with the reality that coupling a qubit to large (infinite) environment is a daunting task. As the decoherence of the qubit is the point of interest, we adopt a common technique involving an effective description of the environment's impact on the 2×2 subspace of the qubit through the use of self-energies − we derive an effective description of a subsystem coupled to a large, and potentially infinite, system or environment. For definiteness, we will derive below the Hamiltonian and the Green's function for a double dot coupled to a 1-d semi-infinite SSH chain described by H_{SSH}. In particular, we will work with the case of the double dot coupling to the edge of the chain. These results can easily be generalized to various environments and coupling sites afterwards. The Hamiltonian for the full system is

$$H = \begin{pmatrix} \epsilon_1 & \tau & & & & \\ \tau & \epsilon_2 & t_c & & & \\ & t_c & 0 & t_1 & & \\ & & t_1 & 0 & t_2 & \\ & & & t_2 & 0 & t_1 \\ & & & & t_1 & \ddots \end{pmatrix} = \left(\begin{array}{c|c} H_{\text{DD}} & W \\ \hline W^\dagger & H_{\text{SSH}} \end{array}\right) \tag{2.4.1}$$

Here, W is a $2\times\infty$ matrix with $\text{W}_{2,1}{=}t_c$ as the only nonzero entry; the coupling between the double dot and the system. The objective here will be to show we can have

$$\begin{gathered} G = (E-H)^{-1} = \left(\begin{array}{c|c} (E-H'_{\text{DD}})^{-1} & \cdots \\ \hline \cdots & \cdots \end{array}\right) = \left(\begin{array}{c|c} G'_{\text{DD}} & \cdots \\ \hline \cdots & \cdots \end{array}\right) \\ H'_{\text{DD}} = H_{\text{DD}} + t_c^2 G^{(1,1)}_{\text{SSH}} \begin{pmatrix} 0 & 0 \\ 0 & 1 \end{pmatrix}, \end{gathered} \tag{2.4.2}$$

where H'_{DD} and G'_{DD} are effective $2{\times}2$ descriptions of the double dot coupled to a semi-infinite environment.

Let us separate the Hamiltonian in the following way:

$$H = \left(\begin{array}{c|c} H_{\text{DD}} & W \\ \hline W^\dagger & H_{\text{SSH}} \end{array}\right) = \underbrace{\left(\begin{array}{c|c} H_{\text{DD}} & 0 \\ \hline 0 & H_{\text{SSH}} \end{array}\right)}_{H_0} + \underbrace{\left(\begin{array}{c|c} 0 & W \\ \hline W^\dagger & 0 \end{array}\right)}_{V}. \tag{2.4.3}$$

We can look at the block diagonal Hamiltonian matrix, H_0, to find its Green's function;

$$G_0 = (E - H_0)^{-1} = \left(\begin{array}{c|c} (E - H_{\rm DD})^{-1} & 0 \\ \hline 0 & (E - H_{\rm SSH})^{-1} \end{array}\right) = \left(\begin{array}{c|c} G_{\rm DD} & 0 \\ \hline 0 & G_{\rm SSH} \end{array}\right). \tag{2.4.4}$$

Using this information in $G = (E - H)^{-1}$;

$$G = (E - H_0 - V)^{-1} = (G_0^{-1} - V)^{-1}. \tag{2.4.5}$$

We can factor the above into a geometric series expansion:

$$G = (G_0^{-1}(1 - G_0 V))^{-1} = (1 - G_0 V)^{-1} G_0 = (1 + G_0 V + (G_0 V)^2 + \cdots) G_0. \tag{2.4.6}$$

Note here that $G'_{\rm DD}$ we are searching for is a diagonal element of G and only even powers of $G_0 V$ contribute to the diagonal block $-$ $G_0 V$ being purely antidiagonal and $(G_0 V)^2$ being purely diagonal. The first power of $(G_0 V)^2$ gives the following

$$(G_0 V)^2 = \left(\begin{array}{c|c} G_{\rm DD} W G_{\rm SSH} W^\dagger & 0 \\ \hline 0 & G_{\rm SSH} W^\dagger G_{\rm DD} W \end{array}\right). \tag{2.4.7}$$

with the (1, 1) block attributed to $G'_{\rm DD}$ in G. Expressing $G'_{\rm DD}$ in the even powers of the series expansion then yields;

$$\begin{aligned} G'_{\rm DD} &= (1 + (G_{\rm DD} W G_{\rm SSH} W^\dagger) + (G_{\rm DD} W G_{\rm SSH} W^\dagger)^2 + \cdots) G_{\rm DD} \\ &= (1 \text{ - } (\mathrm{G}_{\rm DD} W G_{\rm SSH} W^\dagger))^{-1} (G_{\rm DD}^{-1})^{-1} \\ &= (G_{\rm DD}^{-1} - G_{\rm DD}^{-1} G_{\rm DD} W G_{\rm SSH} W^\dagger)^{-1} = (G_{\rm DD}^{-1} - W G_{\rm SSH} W^\dagger)^{-1}, \end{aligned} \tag{2.4.8}$$

where the product $W G_{\rm SSH} W^\dagger$ gives a 2×2 subset of the Green's function selecting the n^{th} diagonal entry $G^{nn}_{\rm SSH}$ to which the double dot is coupling to. In our particular case of a coupling to the edge of the chain, we extract $G^{11}_{\rm SSH}$;

$$W G_{\rm SSH} W^\dagger = t_c^2 G^{11}_{\rm SSH} \begin{pmatrix} 0 & 0 \\ 0 & 1 \end{pmatrix}, \tag{2.4.9}$$

which allows us to express

$$G'_{\rm DD} = (G_{\rm DD}^{-1} - t_c^2 G^{11}_{\rm SSH} \begin{pmatrix} 0 & 0 \\ 0 & 1 \end{pmatrix})^{-1} = (E - H_{\rm DD} - t_c^2 G^{11}_{\rm SSH} \begin{pmatrix} 0 & 0 \\ 0 & 1 \end{pmatrix})^{-1}. \tag{2.4.10}$$

We can see that we have succeeded in deriving an effective form in agreement with (2.4.2) through an effective Hamiltonian for the double dot, which we finally express by way of the self-energy $\Sigma^{11}_{\rm SSH} = t_c^2 G^{11}_{\rm SSH}$:

$$H'_{\rm DD} = H_{\rm DD} + t_c^2 G^{11}_{\rm SSH} \begin{pmatrix} 0 & 0 \\ 0 & 1 \end{pmatrix} = \begin{pmatrix} \epsilon_1 & \tau \\ \tau & \epsilon_2 + \Sigma^{11}_{\rm SSH} \end{pmatrix}, \tag{2.4.11}$$

$$G'_{\mathrm{DD}} = \begin{pmatrix} E-\epsilon_1 & -\tau \\ -\tau & E-\epsilon_2-\Sigma^{11}_{\mathrm{SSH}} \end{pmatrix}^{-1}. \tag{2.4.12}$$

The above is the form used in [5] where only the surface terms were considered. For a coupling to an arbitrary n^{th} site in a bulk, the above derivation is identical except that the product (2.4.9) will extract G^{nn}_{SSH} due to the only nonzero entry of W being $W_{2,n}$. Taking a step back for more generality, the above derivation holds for any model acting as the environment (or reservoir), where we label the Green's function of this environment G_R, so long as the TLS-environment coupling is local and acts on a single site. Let us recall that the Green's function is a function of energy and write so explicitly as well. Therefore, for a general coupling of a double dot to a reservoir with self-energy $\Sigma^{nn}_R = t_c^2 G^{nn}_R$ we have

$$G'_{\mathrm{DD}}(E) = \begin{pmatrix} E-\epsilon_1 & -\tau \\ -\tau & E-\epsilon_2-\Sigma^{nn}_R(E) \end{pmatrix}^{-1}. \tag{2.4.13}$$

Alternative derivation for G'_{DD}

One could wonder if the use of the geometric series in the above derivation leads to issues; at the poles of the Green's function we have diverging singularities but we need $G_0 V < 1$ in order for the sum rule to hold. A more compact derivation that does not require the use of geometric series is possible using simple matrix algebra, as is detailed in Datta [47]. This tells us that the geometric series is useful to shuffle terms around in our previous approach but $G_0 V < 1$ is by no means a strict condition here. Reexpressing (2.4.2) as

$$G = \begin{pmatrix} G'_{\mathrm{DD}} & G_{\mathrm{DD},R} \\ G^\dagger_{\mathrm{DD},R} & G'_R \end{pmatrix} = \begin{pmatrix} E-H_{\mathrm{DD}} & -W \\ -W^\dagger & E-H_R \end{pmatrix}^{-1}. \tag{2.4.14}$$

We know from elementary linear algebra that if

$$\begin{pmatrix} a & b \\ c & d \end{pmatrix} = \begin{pmatrix} A & B \\ C & D \end{pmatrix}^{-1}, \tag{2.4.15}$$

we can left-multiply by $\begin{pmatrix} A & B \\ C & D \end{pmatrix}$ and obtain a system of equations yielding

$$a = (A - BD^{-1}C)^{-1}, \tag{2.4.16}$$

and therefore, with $B = W$, $C = W^\dagger$, and $D = (E - H_R) = G_R^{-1}$;

$$G'_{\mathrm{DD}} = (E - H_{\mathrm{DD}} - W G_R W^\dagger)^{-1}. \tag{2.4.17}$$

Note the product $WG_RW^\dagger$ is exactly what we encountered previously. Taking W as having only a single nonzero element of value t_c at $W_{2,n}$ and remembering $t_c^2 G_R^{nn} = \Sigma_R^{nn}$, we obtain exactly the same result as (2.4.13):

$$G'_{\mathrm{DD}}(E) = \begin{pmatrix} E-\epsilon_1 & -\tau \\ -\tau & E-\epsilon_2-\Sigma_R^{nn}(E) \end{pmatrix}^{-1}. \tag{2.4.18}$$

2.5. TLS coupled to an environment

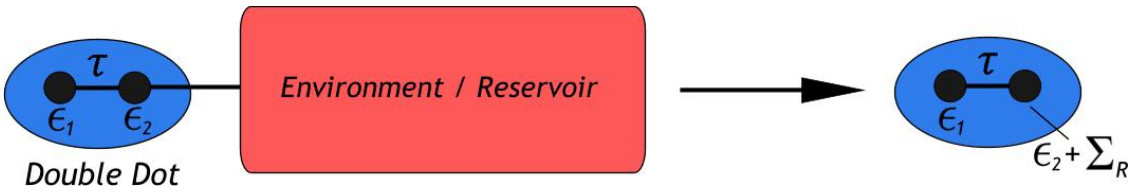

Figure 2.3 – Representation of the effective incorporation of the environment into the 2×2 subspace of the qubit by means of a self-energy Σ_R.

We have just shown, as per equation (2.5.1), that a TLS coupled to an environment has the effective Hamiltonian of the form

$$H'_{\mathrm{DD}}(E) = \begin{pmatrix} \epsilon_1 & \tau \\ \tau & \epsilon_2+\Sigma_R^{nn}(E) \end{pmatrix}, \tag{2.5.1}$$

which can be schematically represented as in Fig. 2.3 for a coupling to an arbitrary site of the reservoir. The self-energy of the environment/reservoir, $\Sigma_R^{nn}(E)$, is a function of E meaning that we now have an explicitly energy-dependent Hamiltonian. Additionally, the self-energy is typically complex so the effective Hamiltonian is non-Hermitian, giving rise to complex energy-dependent eigenvalues. We can solve for these open TLS eigenvalues;

$$\lambda'_\pm(E) = \frac{1}{2}\left(\epsilon_1+\epsilon_2+\Sigma_R^{nn}(E) \pm \delta'(E)\right) = \epsilon_0 + \frac{\Sigma_R^{nn}(E)\pm\delta'(E)}{2}, \tag{2.5.2}$$

where $\delta'(E)$ is the energy splitting of the open TLS

$$\delta'(E) = \sqrt{\left(\epsilon_1-\epsilon_2-\Sigma_R^{nn}(E)\right)^2+4\tau^2} = \sqrt{(\delta_0-\Sigma_R^{nn}(E))^2+4\tau^2}. \tag{2.5.3}$$

The definitions for the average energy of the basis states ϵ_0 and their respective level splitting δ_0 is unchanged from the isolated TLS. Without getting into the implications of an explicitly energy-dependent Hamiltonian and complex eigenvalues, something we address further in Section 4.5, we can qualitatively understand how we expect the open system to behave: looking back at (2.3.6), an application of the residue theorem yields oscillatory exponentials evaluated at the energy-poles, $\lambda_\pm$. Applying this to a complex eigenvalue $\lambda'_\pm(E)$, it becomes clear that imaginary terms will lead to a decay envelope in the time dependent Green's

function. We can attempt to explicitly find $G'^{12}_{\mathrm{DD}}(t)$ by first finding $G'^{12}_{\mathrm{DD}}(E)$:

$$G'^{12}_{\mathrm{DD}}(E) = \frac{\tau}{\delta'(E)}\left(\frac{1}{E-\lambda'_{+}(E)+i0^{+}} - \frac{1}{E-\lambda'_{-}(E)+i0^{+}}\right). \tag{2.5.4}$$

Unlike in the isolated TLS case, the Green's function now has energy-dependent eigenvalues $\lambda'_{\pm}(E)$ and $\delta'(E)$ in both its terms. The Fourier integral takes the corresponding form

$$I_{\pm} \equiv \tau \int_{-\infty}^{\infty} dE \frac{\pm e^{-iEt}}{\delta'(E)\left(E-\lambda'_{\pm}(E)+i0^{+}\right)}, \tag{2.5.5}$$

which cannot be evaluated analytically. We rely here instead on a weak-coupling approximation in order to obtain an analytical form for the time-dependent Green's function.

2.5.1. Decoherence rate approximation

Recall that the self-energy of an environment acting on a TLS is written $\Sigma^{nn}_{R}(E) = t_c^2 G^{nn}_{R}(E)$. Under the approximation that the TLS is weakly coupled to the environment (that is, considering $t_c^2 << 1$), it makes intuitive sense to treat the environment's influence perturbatively. Indeed, a weakly coupled TLS should have eigenvalues $\lambda'_{\pm}(E)$ close to that of an isolated TLS, $\lambda_{\pm}$. There is an additional physical reason why this approximation is of interest: at strong-coupling, decoherence will be an extremely quick process and would be difficult to experimentally work with. A weak coupling between the TLS and its environment allows for a slower decoherence which facilitates experimental accessibility. The entire idea of this derivation is to find an analytical approximation for (2.5.5) in the case of a weakly-coupled TLS and is taken from Appendix A of [48]. We focus on I_{+} for definiteness:

$$I_{+} \equiv \tau \int_{-\infty}^{\infty} dE \frac{e^{-iEt}}{\delta'(E)\left(E-\lambda'_{+}(E)+i0^{+}\right)}. \tag{2.5.6}$$

As alluded to in the previous paragraphs, a small coupling t_c implies that the self-energy will be small and therefore that $\lambda'_{+}(E) \sim \lambda_{+}$ and $\delta'(E) \sim \delta$. From the denominator of I_{+}, it is clear that a pole exists for $E = \lambda'_{+}(E)$. Let us call the energy solution that satisfies this relation, and therefore the energy at the pole, $E^{\star}$. We know, from the residue theorem, that

$$I_{+} = C_{+} e^{-iE^{\star}t}, \tag{2.5.7}$$

where C_{+} is a constant we need not determine for our purposes as we only want the decay rate found in the exponential. We define $\sigma = t_c/2$, and we will expand in powers of σ. Beginning by looking at the limiting case $\sigma = 0$, we explicitly have that $\lambda'_{+}(E) = \lambda_{+}$. If σ is small but nonzero, then a pole dominating the integral can be found at $\lambda'_{+}(E) \sim \lambda_{+}$. Let us now expand $\lambda'_{+}(E)$ and $E^{\star}$ in powers of σ:

$$\begin{aligned} \lambda'_{+}(E) &= \lambda_{+} + \sigma g(E) + \sigma^2 h(E) \\ E^{\star} &= \lambda_{+} + \sigma A + \sigma^2 B \end{aligned} \tag{2.5.8}$$

Because $E^\star$ is the solution to $E = \lambda'_+(E)$, we can Taylor expand up to second order as follows:

$$\begin{aligned} E^\star &= \lambda'_+(E^\star) \\ \lambda_+ + \sigma A + \sigma^2 B &= \lambda'_+(\lambda_+ + \sigma A + \sigma^2 B) \\ &= \lambda_+ + \sigma g(\lambda_+ + \sigma A + \sigma^2 B) + \sigma^2 h(\lambda_+ + \sigma A + \sigma^2 B) \\ &= \lambda_+ + \sigma(g(\lambda_+) + \sigma A g'(\lambda_+) + \ldots) + \sigma^2(h(\lambda_+) + \ldots) \\ &= \lambda_+ + \sigma g(\lambda_+) + \sigma^2 h(\lambda_+) + \sigma^2 A g'(\lambda_+) + \ldots \end{aligned}$$

We see in the last line that we have all the terms of our power expansion for $\lambda'_+(E)$ evaluated at the frequency of the isolated TLS, λ_+, with an additional term of $O(\sigma^2)$ and higher powers. By comparison with the left hand side, we see that $A = g(\lambda_+)$ and so

$$E^\star = \lambda'_+(\lambda_+) + \sigma^2 g(\lambda_+) g'(\lambda_+) + \ldots \tag{2.5.9}$$

Neglecting powers beyond the first order, we are left with the very simple result that for weak couplings, $E^\star \approx \lambda'_+(\lambda_+)$, i.e. we evaluate the open TLS's energy-dependent eigenvalues at the energy of the isolated TLS. We therefore conclude that (2.5.7) can be written $I_+ = C_+ e^{-i\lambda'_+(\lambda_+)t}$. A similar power expansion for the I_- integral gives $I_- = C_- e^{-i\lambda'_-(\lambda_-)t}$, where C_- is an integration constant. Summing both integrals, we obtain an expression for the Fourier transform of (2.5.4)

$$G'^{12}_{\mathrm{DD}}(t) \approx C_+ e^{-i\lambda'_+(\lambda_+)t} + C_- e^{-i\lambda'_-(\lambda_-)t}. \tag{2.5.10}$$

Unlike in the case of the isolated TLS where the frequencies were real and led to oscillatory behaviour, the imaginary contribution to $\lambda'_\pm(\lambda_\pm)$ leads to exponential behaviour. In particular, $-\mathrm{Im}\{\lambda'_\pm(\lambda_\pm)\}$ will be the two terms contributing to decay in $G'^{12}_{\mathrm{DD}}(t)$. The slowest of the two decays will dominate the long time evolution of the system. Expressed in terms of the inverse of the decay constant, τ_ϕ^{nn}, not to be confused with the TLS parameter τ, we find the following expression for the decay rate:

$$(\tau_\phi^{nn})^{-1} \approx \min\Big(-\mathrm{Im}\{\lambda'_\pm(\lambda_\pm)\}\Big). \tag{2.5.11}$$

Upon inspection of $\lambda'_\pm(E)$, (2.5.2), we note that ϵ_0 is strictly real and therefore the imaginary contribution can only come from the self-energy and splitting terms:

$$(\tau_\phi^{nn})^{-1} \approx \min\Big(-\frac{1}{2}\mathrm{Im}\{\Sigma_R^{nn}(\lambda_\pm) \pm \delta'(\lambda_\pm)\}\Big). \tag{2.5.12}$$

Just like in the isolated TLS, the time-dependent Green's function for the open system retains its oscillatory behaviour proportional to the real parts of $\Sigma_R^{nn}(\lambda_\pm) \pm \delta'(\lambda_\pm)$, while the

imaginary parts contribute to decays. This tells us that the system will continue to oscillate but over time will be damped by a decay parameter, corresponding to an exponential-in-time decrease in probability of observing a level transition. In other words, over time the system converges to a single state and is no longer in a superposition; it decoheres due to its coupling to the environment. Specifically, it does so proportionally to the imaginary parts of the self-energy of the environment at the point of coupling Σ_R^{nn}, and the energy splitting of the coupled qubit, δ'. To highlight the dependence on the coupling site, the position indices n are explicitly written in the decoherence rate above. In order to describe this decoherence further, it becomes necessary to consider explicit environment descriptions for Σ_R^{nn}.

Chapter 3

The Environment's Green's Functions

Having derived an expression for the decoherence rate of a TLS weakly-coupled to an environment, the only remaining step is to choose a specific environment and obtain its self-energy for use in (2.5.12). The TLS will be coupled to a finite SSH chain in order to study topological edge states but this is not sufficient to observe decoherence; indeed, this would simply amount to an $(N+2)\times(N+2)$ closed system where state mixing is possible but not decoherence. To make this system truly open, we will add semi-infinite leads acting like dissipative channels therefore connecting our qubit and SSH system to an infinite environment.

3.1. Tripartite System

Let us now consider our mesoscopic system of interest consisting of a finite SSH chain of length N, described by the $N\times N$ Hamiltonian, H_{SSH}, coupled at each end to a semi-infinite lead, H_∞, with strength $t_{L,R}$ corresponding left and right couplings, respectively. It is useful to define the system with two leads for greater generality, where a left (right) lead can be removed by simply setting t_L (t_R)$=0$ afterwards. The coupling matrices W_L and W_R are of size $\infty\times N$ and $N\times\infty$, having as their only nonzero entry $W_{L(\infty,1)}$ and $W_{R(N,1)}$. A double dot is coupled to an arbitrary n^{th} site of the SSH chain through a tunneling parameter t_c acting on the second basis state, ϵ_2. The coupling matrix V_N is of dimensions $N\times N$ with $V_{N(2,n)}$ the only nonzero entry as we choose to express H_{DD} in the standard form with ϵ_2 being at position (2, 2). A schematic representation of this system is shown in Fig. 3.1 and the full Hamiltonian can be written as

$$H=\left(\begin{array}{c|c|c|c} H_{\text{DD}} & 0 & V_N & 0 \\ \hline 0 & H_\infty & W_L & 0 \\ \hline V_N^\dagger & W_L^\dagger & H_{\text{SSH}} & W_R \\ \hline 0 & 0 & W_R^\dagger & H_\infty \end{array}\right), \tag{3.1.1}$$

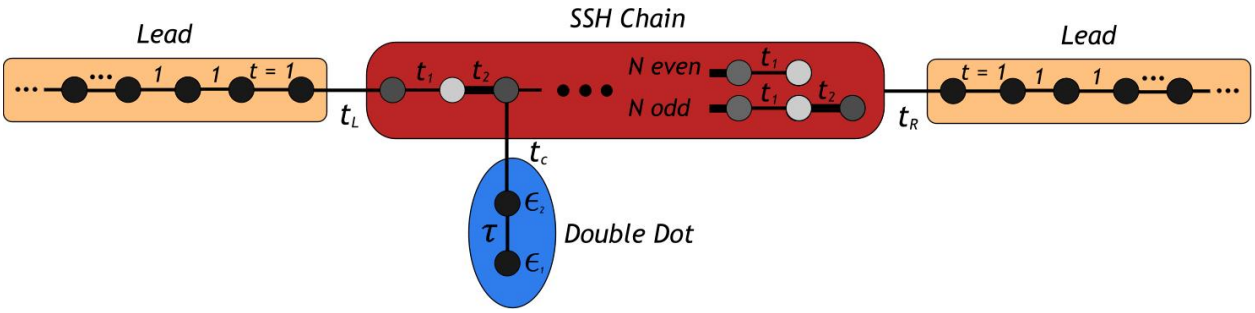

Figure 3.1 – Tripartite system to study the decoherence dynamics of a qubit coupled to a topological material, where the coupling t_c can be taking on any n^{th} site of the SSH chain.

where H_∞, the Hamiltonian for a semi-infinite lead, is given by

$$H_\infty = \begin{pmatrix} 0 & t & & & \\ t & 0 & t & & \\ & t & 0 & t & \\ & & t & 0 & \ddots \\ & & & \ddots & \ddots \end{pmatrix}. \tag{3.1.2}$$

We choose to normalize the energy scale with respect to the semi-infinite leads' hopping term, dividing H through by t, and relabelling the scaled hopping terms (for example, $t_1/t \to t_1$). With this scaling, H_∞ is simply

$$H_\infty \to \begin{pmatrix} 0 & 1 & & & \\ 1 & 0 & 1 & & \\ & 1 & 0 & 1 & \\ & & 1 & 0 & \ddots \\ & & & \ddots & \ddots \end{pmatrix}, \tag{3.1.3}$$

and the leads feature energy bands bound between -2 $< E <$2. We now apply an effective description by way of self-energies step by step for clarity: first we examine the central 2×2 block of H;

$$\left(\begin{array}{c|c} H_\infty & W_L \\ \hline W_L^\dagger & H_{\text{SSH}} \end{array}\right) \to \begin{pmatrix} \Sigma_L & t_1 & 0 & \cdots & 0 \\ t_1 & 0 & t_2 & \ddots & \vdots \\ 0 & t_2 & \ddots & \ddots & 0 \\ \vdots & \ddots & \ddots & 0 & t \\ 0 & \cdots & 0 & t & 0 \end{pmatrix}. \tag{3.1.4}$$

The final entry of the SSH chain t depends on the parity of N. Here, Σ_L is the self-energy due to the left semi-infinite lead expressed in terms of the surface Green's function [5, 48];

$$\Sigma_L(E) = t_L^2 G_\infty^S(E),$$
$$G_\infty^S(E) = \begin{cases} \frac{1}{2}(E - i\sqrt{4-E^2}) & \text{for } E > -2 \\ \frac{1}{2}(E + i\sqrt{4-E^2}) & \text{for } E < -2. \end{cases} \tag{3.1.5}$$

The above Green's function, $G_\infty^S(E)$, is valid strictly for real energies. For complex energies, the expressions remain the same but the conditions on E change. Applying the same self-energy method to the bottom diagonal 2×2 block to account for the right lead and combining the result with (3.1.4), we have for the bottom 3×3 block of H,

$$\left(\begin{array}{c|c|c} H_\infty & W_L & 0 \\ \hline W_L^\dagger & H_{\text{SSH}} & W_R \\ \hline 0 & W_R^\dagger & H_\infty \end{array}\right) \rightarrow \begin{pmatrix} \Sigma_L & t_1 & 0 & \cdots & 0 \\ t_1 & 0 & t_2 & \ddots & \vdots \\ 0 & t_2 & \ddots & \ddots & 0 \\ \vdots & \ddots & \ddots & 0 & t \\ 0 & \cdots & 0 & t & \Sigma_R \end{pmatrix} \tag{3.1.6}$$
$$\equiv H_{\text{SSH},\infty},$$

where the right lead is described by the same surface Green's function $G_\infty^S(E)$, yielding the self-energy $\Sigma_R(E) = t_R^2 G_\infty^S(E)$, with t_R the coupling to the right lead. We can now express H in a more tractable manner, having taken the system from its infinite dimension to a reduced $(N+2)\times(N+2)$ size;

$$H = \left(\begin{array}{c|c} H_{\text{DD}} & V_N \\ \hline V_N^\dagger & H_{\text{SSH},\infty} \end{array}\right). \tag{3.1.7}$$

For example, we can write (3.1.7) for a coupling of the double dot at the first site of the SSH chain as

$$H = \begin{pmatrix} \epsilon_1 & \tau & & & & & & \\ \tau & \epsilon_2 & t_c & & & & & \\ & t_c & \Sigma_L & t_1 & & & & \\ & & t_1 & 0 & t_2 & & & \\ & & & t_2 & 0 & t_1 & & \\ & & & & t_1 & \ddots & \ddots & \\ & & & & & \ddots & \ddots & t \\ & & & & & & t & \Sigma_R \end{pmatrix}. \tag{3.1.8}$$

We see we have a form similar to (2.4.1) but now with additional self-energies. Back to the general case of an arbitrary coupling, a final step in reducing the Hamiltonian to a 2×2

effective description of the double dot gives;

$$H \to H'_{\mathrm{DD}} = \begin{pmatrix} \epsilon_1 & \tau \\ \tau & \epsilon_2 + t_c^2 G^{nn}_{\mathrm{SSH},\infty} \end{pmatrix}. \tag{3.1.9}$$

This form is not surprising and follows directly from (2.5.1) where the environment is an SSH chain of length N with two leads attached to the endpoints, as captured by the self-energy $\Sigma^{nn}_{\mathrm{SSH},\infty} = t_c^2 G^{nn}_{\mathrm{SSH},\infty}$.

3.2. Finding $G^{nn}_{\mathrm{SSH},\infty}(E)$

In what follows, a solution for $G^{nn}_{\mathrm{SSH},\infty}(E)$ is obtained analytically. As this represents a large and tedious calculation, the problem was approached in steps:

(1) Solving for the surface Green's functions of a pure SSH chain, G^{11}_{SSH} and G^{NN}_{SSH}.

(2) Solving for an arbitrary site in a pure SSH chain G^{nn}_{SSH}.

(3) Solving for the full system, $G^{nn}_{\mathrm{SSH},\infty}$, which inludes the addition of lead boundary terms.

These multiple steps were useful for pedagogical reasons and allowed for ample consistency checks along the way. Presented here is only the final result for $G^{nn}_{\mathrm{SSH},\infty}$. Our task is, in principle, simple: find the diagonal elements of $G_{\mathrm{SSH},\infty}$.

$$\begin{aligned} G_{\mathrm{SSH},\infty} &= (E - H_{\mathrm{SSH},\infty})^{-1} \\ (E - H_{\mathrm{SSH},\infty}) G_{\mathrm{SSH},\infty} &= \mathbb{1} \end{aligned} \tag{3.2.1}$$

The subscript (SSH, ∞) will be supressed to lighten notation in what follows. Expressed in matrix form, and for an arbitrary SSH length N keeping in mind $t = t_1$ or t_2 for N even or odd, respectively, (3.2.1) becomes

$$\begin{pmatrix} E-\Sigma_L & -t_1 & & & & & \\ -t_1 & E & -t_2 & & & & \\ & -t_2 & E & -t_1 & & & \\ & & -t_1 & E & \ddots & & \\ & & & \ddots & \ddots & -t & \\ & & & & -t & E-\Sigma_R \end{pmatrix} \begin{pmatrix} G^{11} & G^{12} & & \dots & & G^{1N} \\ G^{21} & G^{22} & \ddots & & & \\ & \ddots & \ddots & & & \\ \vdots & & & & \ddots & \\ & & & \ddots & \ddots & \\ G^{N1} & & & & & G^{NN} \end{pmatrix} = \mathbb{1}. \tag{3.2.2}$$

A useful trick to realize is that we need not solve the full matrix if we instead consider a column vector of G and ensure we select the equivalent column from $\mathbb{1}$;

$$\begin{pmatrix} E-\Sigma_L & -t_1 & & & & & \\ -t_1 & E & -t_2 & & & & \\ & -t_2 & E & -t_1 & & & \\ & & -t_1 & E & \ddots & & \\ & & & \ddots & \ddots & -t & \\ & & & & -t & E-\Sigma_R \end{pmatrix} \begin{pmatrix} G^{1n} \\ G^{2n} \\ \vdots \\ G^{nn} \\ \vdots \\ G^{N-1,n} \\ G^{Nn} \end{pmatrix} = \begin{pmatrix} 0 \\ 0 \\ \vdots \\ 1 \\ \vdots \\ 0 \\ 0 \end{pmatrix}. \tag{3.2.3}$$

We note that (3.2.3) actually contains four distinct configurations stemming from the parity of the SSH chain length, N, and the parity of the column we choose, n, which corresponds to the site we are coupling to. The element G^{nn} is derived for each configuration below. We observe that, structurally, the equation is nearly identical to the Schrödinger equation with the exception of an inhomogeneity at the n^{th} site. We therefore approach this problem with the same translationally invariant ansatz as for the SSH model wavefunctions, applied here to the column vector of G, with the addition of a boundary term at the n^{th} element of the column vector. It is worth keeping in mind that the index n labels the sites of the SSH chain, while the index m serves as the unit cell label. The latter will be used for the following derivations as it is more natural in the context of the ansatz, and $m \to n$ will only be applied to the final result. We derive the odd-N odd-n configuration first in detail. The other configurations are presented in less detail here due to the similarity of the procedure.

3.2.1. N odd n odd

For N odd, we recall that the final entry of our column vector of G, which we'll now call $\boldsymbol{G}$, will be an incomplete unit cell. Additionally, considering n odd implies that n corresponds to sites of the A sublattice and so the boundary term in $\boldsymbol{G}$ will be labelled A_0. Written out,

$\boldsymbol{G}$ takes on the following form:

$$\boldsymbol{G} \equiv \begin{pmatrix} G^{1n} \\ G^{2n} \\ \vdots \\ G^{nn} \\ \vdots \\ G^{N-1,n} \\ G^{Nn} \end{pmatrix} = \begin{pmatrix} C_+e^{-i\varphi} + C_-e^{i\varphi} \\ \pm(C_+e^{i\varphi} + C_-e^{-i\varphi}) \\ C_+e^{-i\varphi}e^{i2k} + C_-e^{i\varphi}e^{-i2k} \\ \pm(C_+e^{i\varphi}e^{i2k} + C_-e^{-i\varphi}e^{-i2k}) \\ \vdots \\ C_+e^{-i\varphi}e^{i(2m-2)k} + C_-e^{i\varphi}e^{-i(2m-2)k} \\ \pm(C_+e^{i\varphi}e^{i(2m-2)k} + C_-e^{-i\varphi}e^{-i(2m-2)k}) \\ 2A_0 \to n^{th} \text{ site} \\ \pm(D_+e^{i\varphi}e^{i2mk} + D_-e^{-i\varphi}e^{-i2mk}) \\ D_+e^{-i\varphi}e^{i(2m+2)k} + D_-e^{i\varphi}e^{-i(2m+2)k} \\ \pm(D_+e^{i\varphi}e^{i(2m+2)k} + D_-e^{-i\varphi}e^{-i(2m+2)k}) \\ \vdots \\ (D_+e^{-i\varphi}e^{i(N-3)k} + D_-e^{i\varphi}e^{-i(N-3)k}) \\ \pm(D_+e^{i\varphi}e^{i(N-3)k} + D_-e^{-i\varphi}e^{-i(N-3)k}) \\ (D_+e^{-i\varphi}e^{i(N-1)k} + D_-e^{i\varphi}e^{-i(N-1)k}) \end{pmatrix}. \tag{3.2.4}$$

Note how in writing this, we can see this is the same ansatz as an even SSH chain (with constants $C_\pm$) attached to another even SSH chain (with constants $D_\pm$), both coupled together by the A_0 term. Note how the second bulk terms ($D_\pm$) describe a different unit cell configuration: $B - AB - ... - AB - A$ compared to the first bulk terms ($C_\pm$) showing a *standard* cell division: $AB - AB - ... - AB$.

We need to solve for the constants $C_\pm$ and $D_\pm$. Looking at the boundary equations of the first bulk, we have

$$(E - \Sigma_L)(C_+e^{-i\varphi} + C_-e^{i\varphi}) \mp t_1(C_+e^{i\varphi} + C_-e^{-i\varphi}) = 0$$
$$\pm E(C_+e^{i\varphi}e^{i(2m-2)k} + C_-e^{-i\varphi}e^{-i(2m-2)k}) - t_1(C_+e^{-i\varphi}e^{i(2m-2)k} + C_-e^{i\varphi}e^{-i(2m-2)k}) = 2t_2A_0,$$

which we can simplify using $|E|e^{\pm i2\varphi} = (t_1 + t_2e^{\pm i2k})$:

$$\begin{gathered}(\pm t_2e^{i\varphi}e^{-i2k} - \Sigma_Le^{-i\varphi})C_+ + (\pm t_2e^{-i\varphi}e^{i2k} - \Sigma_Le^{i\varphi})C_- = 0 \\ e^{-i\varphi}e^{i2mk}C_+ + e^{i\varphi}e^{-i2mk}C_- = 2A_0.\end{gathered} \tag{3.2.5}$$

This yields

$$\begin{pmatrix} C_+ \\ C_- \end{pmatrix} = \frac{EA_0}{i(\Sigma_LEs_{2m} - t_2(t_1s_{2m+2} + t_2s_{2m}))} \begin{pmatrix} \mp t_2e^{-i\varphi}e^{i2k} + \Sigma_Le^{i\varphi} \\ \pm t_2e^{i\varphi}e^{-i2k} - \Sigma_Le^{-i\varphi} \end{pmatrix}. \tag{3.2.6}$$

We now solve for $D_\pm$ using the boundary terms of the second bulk;

$$\pm E(D_+e^{i\varphi}e^{i2mk} + D_-e^{-i\varphi}e^{-i2mk}) - t_2(D_+e^{-i\varphi}e^{i(2m+2)k} + D_-e^{i\varphi}e^{-i(2m+2)k}) = 2t_1A_0$$
$$(E - \Sigma_R)(D_+e^{-i\varphi}e^{i(N-1)k} + D_-e^{i\varphi}e^{-i(N-1)k}) \mp t_2(D_+e^{i\varphi}e^{i(N-3)k} + D_-e^{-i\varphi}e^{-i(N-3)k}) = 0.$$

Simplifying, as for the $C_\pm$ equations using (1.1.11), yields

$$\begin{aligned} t_1 e^{-i\varphi} e^{i2mk} D_+ + t_1 e^{i\varphi} e^{-i2mk} D_- &= 2t_1 A_0 \\ (\pm t_1 e^{i\varphi} - \Sigma_R e^{-i\varphi}) e^{i(N-1)k} D_+ + (\pm t_1 e^{-i\varphi} - \Sigma_R e^{i\varphi}) e^{-i(N-1)k} D_+ &= 0, \end{aligned} \tag{3.2.7}$$

such that we obtain

$$\begin{pmatrix} D_+ \\ D_- \end{pmatrix} = \frac{EA_0}{i(t_1(t_1 s_{N-2m-1} + t_2 s_{N-2m+1}) - \Sigma_R E s_{N-2m-1})} \begin{pmatrix} (\mp t_1 e^{-i\varphi} + \Sigma_R e^{i\varphi}) e^{-i(N-1)k} \\ (\pm t_1 e^{i\varphi} - \Sigma_R e^{-i\varphi}) e^{i(N-1)k} \end{pmatrix}. \tag{3.2.8}$$

Having found expressions for $C_\pm$ and $D_\pm$, we can look back to the n^{th} equation of (3.2.3) combined with our ansatz (3.2.4) to express G^{nn} from $G^{nn} = 2A_0$,

$$\begin{aligned} \mp t_2 G^{n-1,n} + E G^{nn} \mp t_1 G^{n+1,n} &= 1 \\ \mp t_2 (C_+ e^{i\varphi} e^{i(2m-2)k} + C_- e^{-i\varphi} e^{-i(2m-2)k}) + E G^{nn} \mp t_1 (D_+ e^{i\varphi} e^{i2mk} + D_- e^{-i\varphi} e^{-i2mk}) &= 1. \end{aligned} \tag{3.2.9}$$

Plugging in $C_\pm$ and $D_\pm$ above and carrying out some algebra, we find

$$\begin{aligned} G^{nn} = \Bigg[E + \frac{t_2^2 E s_{2m} - t_2 \Sigma_L \left(t_1 s_{2m-2} + t_2 s_{2m}\right)}{E \Sigma_L s_{2m} - t_2 \left(t_1 s_{2m+2} + t_2 s_{2m}\right)} \\ + \frac{t_1^2 E s_{N-2m-1} - t_1 \Sigma_R \left(t_1 s_{N-2m-1} + t_2 s_{N-2m-3}\right)}{E \Sigma_R s_{N-2m-1} - t_1 \left(t_1 s_{N-2m-1} + t_2 s_{N-2m+1}\right)} \Bigg]^{-1}. \end{aligned} \tag{3.2.10}$$

Recall in the above that $\Sigma_{L,R}(E)$ are the left and right lead self-energies. A substitution $n = 2m+1$ (since n is odd within the unit cell) gives an expression in terms of the positional site index n:

$$\begin{aligned} G^{nn}_{\mathrm{SSH},\infty}(E) = \Bigg[E + \frac{t_2^2 E s_{n-1} - t_2 \Sigma_L(E) \left(t_1 s_{n-3} + t_2 s_{n-1}\right)}{E \Sigma_L(E) s_{n-1} - t_2 \left(t_1 s_{n+1} + t_2 s_{n-1}\right)} \\ + \frac{t_1^2 E s_{N-n} - t_1 \Sigma_R(E) \left(t_1 s_{N-n} + t_2 s_{N-n-2}\right)}{E \Sigma_R(E) s_{N-n} - t_1 \left(t_1 s_{N-n} + t_2 s_{N-n+2}\right)} \Bigg]^{-1}, \quad \text{for } N \text{ odd } n \text{ odd}. \end{aligned} \tag{3.2.11}$$

This resolution method, using a column vector $\boldsymbol{G}$, finding the constants $C_\pm$ and $D_\pm$, and using this information in the n^{th} equation to find $G^{nn}_{\mathrm{SSH},\infty}(E)$, is identical for the three other configurations. As such, intermediate steps will be shown more sparingly in what follows.

3.2.2. N odd n even

Given that N is odd here as well, the ansatz for $\boldsymbol{G}$ will look very similar to the previous section with a slight difference due to n being even resulting in two ($C_\pm$ and $D_\pm$) odd-length bulks both structured $AB - AB - ... - AB - A$. As the n^{th} site is now even, it will always

be on sublattice B of the SSH chain and the boundary term will be named B_0.

$$\boldsymbol{G} \equiv \begin{pmatrix} G^{1n} \\ G^{2n} \\ \vdots \\ G^{nn} \\ \vdots \\ G^{N-1,n} \\ G^{Nn} \end{pmatrix} = \begin{pmatrix} C_+e^{-i\varphi} + C_-e^{i\varphi} \\ \pm(C_+e^{i\varphi} + C_-e^{-i\varphi}) \\ C_+e^{-i\varphi}e^{i2k} + C_-e^{i\varphi}e^{-i2k} \\ \pm(C_+e^{i\varphi}e^{i2k} + C_-e^{-i\varphi}e^{-i2k}) \\ \vdots \\ \pm(C_+e^{i\varphi}e^{i(2m-2)k} + C_-e^{-i\varphi}e^{-i(2m-2)k}) \\ C_+e^{-i\varphi}e^{i2mk} + C_-e^{i\varphi}e^{-i2mk} \\ 2B_0 \to n^{th} \text{ site} \\ D_+e^{-i\varphi}e^{i(2m+2)k} + D_-e^{i\varphi}e^{-i(2m+2)k} \\ \pm(D_+e^{i\varphi}e^{i(2m+2)k} + D_-e^{-i\varphi}e^{-i(2m+2)k}) \\ \vdots \\ D_+e^{-i\varphi}e^{i(N-3)k} + D_-e^{i\varphi}e^{-i(N-3)k} \\ \pm(D_+e^{i\varphi}e^{i(N-3)k} + D_-e^{-i\varphi}e^{-i(N-3)k}) \\ D_+e^{-i\varphi}e^{i(N-1)k} + D_-e^{i\varphi}e^{-i(N-1)k} \end{pmatrix} \tag{3.2.12}$$

As before, we solve for the constants in the first bulk looking at the first and $(n-1)^{th}$ equations in (3.2.3):

$$\begin{pmatrix} C_+ \\ C_- \end{pmatrix} = \frac{EB_0}{i(\Sigma_L(t_1 s_{2m} + t_2 s_{2m+2}) - Et_2 s_{2m+2})} \begin{pmatrix} \mp t_2 e^{-i\varphi}e^{i2k} + \Sigma_L e^{i\varphi} \\ \pm t_2 e^{i\varphi}e^{-i2k} - \Sigma_L e^{-i\varphi} \end{pmatrix}. \tag{3.2.13}$$

Solving for the second bulk $D_\pm$ looking at the $(n+1)^{th}$ and N^{th} equations, we find

$$\begin{pmatrix} D_+ \\ D_- \end{pmatrix} = \frac{EB_0}{i(t_1(t_1 s_{N-2m-1} + t_2 s_{N-2m+1}) - \Sigma_R E s_{N-2m-1})} \begin{pmatrix} (\mp t_1 e^{-i\varphi} + \Sigma_R e^{i\varphi})e^{-i(N-1)k} \\ (\pm t_1 e^{i\varphi} - \Sigma_R e^{-i\varphi})e^{i(N-1)k} \end{pmatrix}. \tag{3.2.14}$$

We now find G^{nn} plugging these constants in the n^{th} equation of (3.2.3):

$$\begin{gathered} -t_1 G^{n-1,n} + EG^{nn} - t_2 G^{n+1,n} = 1 \\ -t_1(C_+e^{-i\varphi}e^{i2mk} + C_-e^{i\varphi}e^{-i2mk}) + EG^{nn} - t_2(D_+e^{-i\varphi}e^{i(2m+2)k} + D_-e^{i\varphi}e^{-i(2m+2)k}) = 1, \end{gathered} \tag{3.2.15}$$

leading to

$$\begin{aligned} G^{nn} = \Bigg[E + \frac{t_1 \Sigma_L E s_{2m} - t_1 t_2 \left(t_1 s_{2m+2} + t_2 s_{2m}\right)}{Et_2 s_{2m+2} - \Sigma_L \left(t_1 s_{2m} + t_2 s_{2m+2}\right)} \\ + \frac{t_2 E \Sigma_R s_{N-2m-3} - t_1 t_2 \left(t_1 s_{N-2m-3} + t_2 s_{N-2m-1}\right)}{Et_1 s_{N-2m-1} - \Sigma_R \left(t_1 s_{N-2m-1} + t_2 s_{N-2m-3}\right)} \Bigg]^{-1}, \end{aligned} \tag{3.2.16}$$

which we reexpress in terms of site indices $n = 2m+2$, for n even:

$$G^{nn}_{\mathrm{SSH},\infty}(E) = \Bigg[E + \frac{t_1\Sigma_L(E)Es_{n-2} - t_1t_2\left(t_1s_n + t_2s_{n-2}\right)}{Et_2s_n - \Sigma_L(E)\left(t_1s_{n-2} + t_2s_n\right)} + \frac{t_2E\Sigma_R(E)s_{N-n-1} - t_1t_2\left(t_1s_{N-n-1} + t_2s_{N-n+1}\right)}{Et_1s_{N-n+1} - \Sigma_R(E)\left(t_1s_{N-n+1} + t_2s_{N-n-1}\right)}\Bigg]^{-1}, \quad \text{for } N \text{ odd } n \text{ even.} \tag{3.2.17}$$

3.2.3. N even n odd

Let us express the appropriate ansatz for $\boldsymbol{G}$. Recall here that an even chain of length N has hopping parameter t_1 at the end of the chain. The even parity also changes the power in e^{i2mk} with $N = 2M$ rather than $2M + 1$ which we had for the previous N odd cases; the powers will take on the form $(N - 2)$, $(N - 4)$, ...

$$\boldsymbol{G} \equiv \begin{pmatrix} G^{1n} \\ G^{2n} \\ \vdots \\ G^{nn} \\ \vdots \\ G^{N-1,n} \\ G^{Nn} \end{pmatrix} = \begin{pmatrix} C_+e^{-i\varphi} + C_-e^{i\varphi} \\ \pm(C_+e^{i\varphi} + C_-e^{-i\varphi}) \\ C_+e^{-i\varphi}e^{i2k} + C_-e^{i\varphi}e^{-i2k} \\ \pm(C_+e^{i\varphi}e^{i2k} + C_-e^{-i\varphi}e^{-i2k}) \\ \vdots \\ C_+e^{-i\varphi}e^{i(2m-2)k} + C_-e^{i\varphi}e^{-i(2m-2)k} \\ \pm(C_+e^{i\varphi}e^{i(2m-2)k} + C_-e^{-i\varphi}e^{-i(2m-2)k}) \\ 2A_0 \to n^{th} \text{ site} \\ \pm(D_+e^{i\varphi}e^{i2mk} + D_-e^{-i\varphi}e^{-i2mk}) \\ D_+e^{-i\varphi}e^{i(2m+2)k} + D_-e^{i\varphi}e^{-i(2m+2)k} \\ \pm(D_+e^{i\varphi}e^{i(2m+2)k} + D_-e^{-i\varphi}e^{-i(2m+2)k}) \\ \vdots \\ \pm(D_+e^{i\varphi}e^{i(N-4)k} + D_-e^{-i\varphi}e^{-i(N-4)k}) \\ (D_+e^{-i\varphi}e^{i(N-2)k} + D_-e^{i\varphi}e^{-i(N-2)k}) \\ \pm(D_+e^{i\varphi}e^{i(N-2)k} + D_-e^{-i\varphi}e^{-i(N-2)k}) \end{pmatrix}. \tag{3.2.18}$$

We can note a useful shortcut here: the first bulk above is identical to the first bulk in the case of odd-N with n odd. This means we have

$$\begin{pmatrix} C_+ \\ C_- \end{pmatrix} = \frac{EA_0}{i(\Sigma_LEs_{2m} - t_2(t_1s_{2m+2} + t_2s_{2m}))} \begin{pmatrix} \mp t_2e^{-i\varphi}e^{i2k} + \Sigma_Le^{i\varphi} \\ \pm t_2e^{i\varphi}e^{-i2k} - \Sigma_Le^{-i\varphi} \end{pmatrix}. \tag{3.2.19}$$

The second bulk is analyzed using, again, the $(n+1)^{th}$ and N^{th} equation of (3.2.3) with our ansatz (3.2.18) to obtain

$$\begin{pmatrix} D_+ \\ D_- \end{pmatrix} = \frac{EA_0}{i(Et_2s_{N-2m} - \Sigma_R(t_1s_{N-2m-2} + t_2s_{N-2m}))} \begin{pmatrix} -(t_2e^{i\varphi}e^{-i2k} \mp \Sigma_Re^{-i\varphi})e^{-i(N-2)k} \\ (t_2e^{-i\varphi}e^{i2k} \mp \Sigma_Re^{i\varphi})e^{i(N-2)k} \end{pmatrix}. \tag{3.2.20}$$

The n^{th} equation of (3.2.3) here is

$$\begin{gathered}-t_2G^{n-1,n}+EG^{nn}-t_1G^{n+1,n}=1\\ \mp t_2(C_+e^{i\varphi}e^{i(2m-2)k}+C_-e^{-i\varphi}e^{-i(2m-2)k})+EG^{nn}\mp t_1(D_+e^{i\varphi}e^{i2mk}+D_-e^{-i\varphi}e^{-i2mk})=1,\end{gathered} \tag{3.2.21}$$

which gives, after substituting $n=2m+1$ for n odd,

$$\begin{aligned}G^{nn}_{\mathrm{SSH},\infty}(E)=\Bigg[E+\frac{t_2^2Es_{n-1}-t_2\Sigma_L(E)\left(t_1s_{n-3}+t_2s_{n-1}\right)}{E\Sigma_L(E)s_{n-1}-t_2\left(t_1s_{n+1}+t_2s_{n-1}\right)}\\ +\frac{t_1E\Sigma_R(E)s_{N-n-1}-t_1t_2\left(t_1s_{N-n+1}+t_2s_{N-n-1}\right)}{Et_2s_{N-n+1}-\Sigma_R(E)\left(t_1s_{N-n-1}+t_2s_{N-n+1}\right)}\Bigg]^{-1},\quad \text{for } N \text{ even } n \text{ odd.}\end{aligned} \tag{3.2.22}$$

3.2.4. N even n even

In writing our ansatz for even-N with n even, we note that the first bulk with constants $C_\pm$ is identical to the case of odd-N with n even:

$$\boldsymbol{G}\equiv\begin{pmatrix}G^{1n}\\G^{2n}\\\vdots\\G^{nn}\\\vdots\\G^{N-1,n}\\G^{Nn}\end{pmatrix}=\begin{pmatrix}C_+e^{-i\varphi}+C_-e^{i\varphi}\\ \pm(C_+e^{i\varphi}+C_-e^{-i\varphi})\\ C_+e^{-i\varphi}e^{i2k}+C_-e^{i\varphi}e^{-i2k}\\ \pm(C_+e^{i\varphi}e^{i2k}+C_-e^{-i\varphi}e^{-i2k})\\ \vdots\\ \pm(C_+e^{i\varphi}e^{i(2m-2)k}+C_-e^{-i\varphi}e^{-i(2m-2)k})\\ C_+e^{-i\varphi}e^{i2mk}+C_-e^{i\varphi}e^{-i2mk}\\ 2B_0\to n^{th}\text{ site}\\ D_+e^{-i\varphi}e^{i(2m+2)k}+D_-e^{i\varphi}e^{-i(2m+2)k}\\ \pm(D_+e^{i\varphi}e^{i(2m+2)k}+D_-e^{-i\varphi}e^{-i(2m+2)k})\\ \vdots\\ \pm(D_+e^{i\varphi}e^{i(N-3)k}+D_-e^{-i\varphi}e^{-i(N-3)k})\\ D_+e^{-i\varphi}e^{i(N-1)k}+D_-e^{i\varphi}e^{-i(N-1)k}\\ \pm(D_+e^{i\varphi}e^{i(N-1)k}+D_-e^{-i\varphi}e^{-i(N-1)k})\end{pmatrix}. \tag{3.2.23}$$

We already know $C_\pm$ are identical to (3.2.13) and are given by

$$\begin{pmatrix}C_+\\C_-\end{pmatrix}=\frac{EB_0}{i(\Sigma_L(t_1s_{2m}+t_2s_{2m+2})-Et_2s_{2m+2})}\begin{pmatrix}\mp t_2e^{-i\varphi}e^{i2k}+\Sigma_Le^{i\varphi}\\ \pm t_2e^{i\varphi}e^{-i2k}-\Sigma_Le^{-i\varphi}\end{pmatrix}, \tag{3.2.24}$$

and we find for the second bulk

$$\begin{pmatrix} D_+ \\ D_- \end{pmatrix} = \frac{EB_0}{i(t_2(t_1 s_{N-2m} + t_2 s_{N-2m-2} - E\Sigma_R s_{N-2m-2}))} \begin{pmatrix} -(t_2 e^{i\varphi} e^{-i2k} \mp \Sigma_R e^{-i\varphi}) e^{-i(N-2)k} \\ (t_2 e^{-i\varphi} e^{i2k} \mp \Sigma_R e^{i\varphi}) e^{i(N-2)k} \end{pmatrix}. \tag{3.2.25}$$

The n^{th} equation to solve for G^{nn} yields

$$\begin{gathered} -t_1 G^{n-1,n} + EG^{nn} - t_2 G^{n+1,n} = 1 \\ t_1(C_+ e^{-i\varphi} e^{i2mk} + C_- e^{i\varphi} e^{-i2mk}) + EG^{nn} - t_2(D_+ e^{-i\varphi} e^{i(2m+2)k} + D_- e^{i\varphi} e^{-i(2m+2)k}) = 1, \end{gathered} \tag{3.2.26}$$

which, after replacing m by $n = 2m + 2$;

$$\begin{aligned} G^{nn}_{\mathrm{SSH},\infty}(E) = \Bigg[E + \frac{t_1 \Sigma_L(E) E s_{n-2} - t_1 t_2 \left(t_1 s_n + t_2 s_{n-2}\right)}{E t_2 s_n - \Sigma_L(E) \left(t_1 s_{n-2} + t_2 s_n\right)} \\ + \frac{t_2^2 E s_{N-n} - t_2 \Sigma_R(E) \left(t_1 s_{N-n-2} + t_2 s_{N-n}\right)}{E\Sigma_R(E) s_{N-n} - t_2 \left(t_1 s_{N-n+2} + t_2 s_{N-n}\right)} \Bigg]^{-1}, \quad \text{for } N \text{ even } n \text{ even.} \end{aligned} \tag{3.2.27}$$

3.2.5. Summary of results for $G^{nn}_{\mathrm{SSH},\infty}(E)$

We obtained analytical forms for $G^{nn}_{\mathrm{SSH},\infty}(E)$ which depend on the parity of the chain length and the parity of the sublattice site n. The shorthand notation $\Sigma_{L,R}(E) = \Sigma_{L,R}$ is used below out of space concerns but these are still energy-dependent quantities as given in (3.1.5). Recall we are additionally using the shorthand for $\sin(Ak) = s_A$. The expressions below are arranged such that the second terms stem from the interface between the left lead and the SSH chain. The third terms correspond to the right lead/SSH-interface (as can be deduced by paying attention to which terms contain $\Sigma_{L,R}$). We note there is a recurrence in these terms; the left boundary terms for both odd-n and both even-n expressions are identical, which is expected as the left boundary conditions are unchanged whether N is even or odd. A similar observation can be made for the right boundary terms; the N odd and n odd term has an identical form to the N even and n even term but with $t_1 \leftrightarrow t_2$ due to the SSH lattice terminating on a different hopping term for even or odd chain lengths. Equivalently, notice the N odd and n even right boundary term also has an identical form to the N even and n odd case with $t_1 \leftrightarrow t_2$.

For N odd

$$G^{nn}_{\mathrm{SSH},\infty}(E) =$$

$$\begin{cases} \left[E + \dfrac{t_2^2 E s_{n-1} - t_2\Sigma_L\left(t_1 s_{n-3} + t_2 s_{n-1}\right)}{E\Sigma_L s_{n-1} - t_2\left(t_1 s_{n+1} + t_2 s_{n-1}\right)} + \dfrac{t_1^2 E s_{N-n} - t_1\Sigma_R\left(t_1 s_{N-n} + t_2 s_{N-n-2}\right)}{E\Sigma_R s_{N-n} - t_1\left(t_1 s_{N-n} + t_2 s_{N-n+2}\right)}\right]^{-1} & \text{for } n \text{ odd} \\ \left[E + \dfrac{t_1\Sigma_L E s_{n-2} - t_1 t_2\left(t_1 s_n + t_2 s_{n-2}\right)}{E t_2 s_n - \Sigma_L\left(t_1 s_{n-2} + t_2 s_n\right)} + \dfrac{t_2 E\Sigma_R s_{N-n-1} - t_1 t_2\left(t_1 s_{N-n-1} + t_2 s_{N-n+1}\right)}{E t_1 s_{N-n+1} - \Sigma_R\left(t_1 s_{N-n+1} + t_2 s_{N-n-1}\right)}\right]^{-1} & \text{for } n \text{ even} \end{cases} \tag{3.2.28}$$

For N even

$$G^{nn}_{\mathrm{SSH},\infty}(E) =$$

$$\begin{cases} \left[E + \dfrac{t_2^2 E s_{n-1} - t_2\Sigma_L\left(t_1 s_{n-3} + t_2 s_{n-1}\right)}{E\Sigma_L s_{n-1} - t_2\left(t_1 s_{n+1} + t_2 s_{n-1}\right)} + \dfrac{t_1 E\Sigma_R s_{N-n-1} - t_1 t_2\left(t_1 s_{N-n+1} + t_2 s_{N-n-1}\right)}{E t_2 s_{N-n+1} - \Sigma_R\left(t_1 s_{N-n-1} + t_2 s_{N-n+1}\right)}\right]^{-1} & \text{for } n \text{ odd} \\ \left[E + \dfrac{t_1\Sigma_L E s_{n-2} - t_1 t_2\left(t_1 s_n + t_2 s_{n-2}\right)}{E t_2 s_n - \Sigma_L\left(t_1 s_{n-2} + t_2 s_n\right)} + \dfrac{t_2^2 E s_{N-n} - t_2\Sigma_R\left(t_1 s_{N-n-2} + t_2 s_{N-n}\right)}{E\Sigma_R s_{N-n} - t_2\left(t_1 s_{N-n+2} + t_2 s_{N-n}\right)}\right]^{-1} & \text{for } n \text{ even} \end{cases} \tag{3.2.29}$$

Chapter 4

Decoherence Probe Results and Discussion

An important technological challenge in the field of quantum computing is maximizing the longevity of qubits - the foundation of any quantum memory architecture. For this reason, much effort is dedicated towards research aiming to improve technologies that can reduce the decoherence rate of qubit systems, allowing for longer run times and hence more powerful quantum computers. Increasing the longevity of qubits is therefore of paramount importance for quantum computing. In this context, the environment is viewed as a collection of perturbations negatively affecting qubits. That said, technology-driven research focusing only on preventing decoherence can lead one to overlook subtle and interesting physics. In particular, decoherence ensues from contact to an environment, but how can the dynamics of decoherence be used to study this environment? This viewpoint flips the conventional approach to the study of qubit decoherence, and will be the focus of the remainder of this thesis where we use a decohering qubit as a novel quantum sensor to probe materials. Specifically, we aim to probe interesting features such as topological and localized states in low-dimensional systems.

An expression for the decoherence rate of a TLS interacting with an arbitrary environment through a coupling parameter t_c was derived in Chapter 2 in the form of equation (2.5.12). To study decoherence dynamics, it is necessary to consider a particular environment in order to obtain a form of the self-energy Σ_R^{nn} for use in (2.5.12). In Chapter 3, a tripartite system was introduced. The derived Green's functions, (3.2.28) and (3.2.29) for SSH chains of odd and even length, respectively, directly lead to the self-energy $\Sigma_{\mathrm{SSH},\infty}^{nn}$, allowing for the study of the decoherence dynamics in the tripartite system. In this chapter, we investigate the explicit full form of the decoherence rate expression applied to the tripartite system, describe the proposed probe, and mention important details on edge state detection. We then discuss the influence of various system parameters on the probe as well as interesting open system properties to which the probe is sensitive.

4.1. Interpretation of the decoherence rate

The decoherence rate for a TLS coupled to an environment (2.5.12) can be written, for the specific case of the tripartite system studied in Chapter 3, as

$$(\tau_\phi^{nn})^{-1} \approx \min\Big(-\frac{1}{2}\mathrm{Im}\{\Sigma^{nn}_{\mathrm{SSH},\infty}(\lambda_\pm) \pm \delta'(\lambda_\pm)\}\Big), \tag{4.1.1}$$

where $\Sigma^{nn}_{\mathrm{SSH},\infty}(\lambda_\pm) = t_c^2 G^{nn}_{\mathrm{SSH},\infty}(\lambda_\pm)$ and

$$\delta'(\lambda_\pm) = \sqrt{\Big(\epsilon_1 - \epsilon_2 - \Sigma^{nn}_{\mathrm{SSH},\infty}(\lambda_\pm)\Big)^2 + 4\tau^2}\,. \tag{4.1.2}$$

Evidently, the first term in (4.1.1) is proportional to the negative imaginary part of a diagonal element of the Green's function. Recall from (2.2.13) that this implies a proportionality to the density of states at the n^{th} site and at the energies of the isolated TLS, $\lambda_\pm$. The term $-\mathrm{Im}\{\Sigma^{nn}_{\mathrm{SSH},\infty}\}$ is therefore directly proportional to the LDOS in the SSH chain. The second contribution $\pm\delta'(\lambda_\pm)$ is more complex. Evidently, there will be some proportionality to $\mathrm{Im}\{G^{nn}_{\mathrm{SSH},\infty}\}$ because we can always factor out $\Sigma^{nn}_{\mathrm{SSH},\infty}$ from the square root. Recalling that $\delta_0 = \epsilon_1 - \epsilon_2$;

$$\delta' = \Sigma^{nn}_{\mathrm{SSH},\infty}\sqrt{\left(1 - \frac{\delta_0}{\Sigma^{nn}_{\mathrm{SSH},\infty}}\right)^2 + \frac{4\tau^2}{{\Sigma^{nn}_{\mathrm{SSH},\infty}}^2}}. \tag{4.1.3}$$

That said, a linear proportionality $\mathrm{Im}\{\delta'\} \propto \mathrm{Im}\{\Sigma^{nn}_{\mathrm{SSH},\infty}\}$ depends on the relationship between the parameters of the TLS and $\Sigma^{nn}_{\mathrm{SSH},\infty}$. In practice, the TLS parameters δ_0 and τ are completely independent of the environment's self-energy and can be chosen small. It is not difficult to show, neglecting terms of second-order and taking $\Sigma^{nn}_{\mathrm{SSH},\infty} >> (\delta_0,\, \tau)$, that an expansion of the root in (4.1.3) yields

$$\delta' = \Sigma^{nn}_{\mathrm{SSH},\infty}\left(1 - \frac{\delta_0}{\Sigma^{nn}_{\mathrm{SSH},\infty}} + \mathcal{O}\left(\frac{1}{{\Sigma^{nn}_{SSH,\infty}}^2}\right) + \dots\right) \approx \Sigma^{nn}_{\mathrm{SSH},\infty}, \tag{4.1.4}$$

with small corrections of order δ_0. We can then write to good approximation that

$$-\mathrm{Im}\{\delta'\} \approx -\mathrm{Im}\{\Sigma^{nn}_{\mathrm{SSH},\infty}\}. \tag{4.1.5}$$

Note that the above line leads to a nearly perfect cancellation for the appropriate upper or lower sign in 4.1.1 for a given $\delta'(\lambda_\pm)$, showing that this near-cancellation is crucial in extracting the slower of the two decoherence rates. With the possibility of choosing TLS parameters δ_0 and τ small with respect to $\Sigma^{nn}_{\mathrm{SSH},\infty}$, we obtain an interesting interpretation for the decoherence rate:

$$\begin{aligned}(\tau_\phi^{nn})^{-1} &\approx \min\Big(-\frac{1}{2}\mathrm{Im}\{\Sigma^{nn}_{\mathrm{SSH},\infty}(\lambda_\pm) \pm \delta'(\lambda_\pm)\}\Big) \\ &\propto -\mathrm{Im}\{G^{nn}_{\mathrm{SSH},\infty}(\lambda_\pm)\}.\end{aligned} \tag{4.1.6}$$

The above bears a striking resemblance to the expression (2.2.13) for the LDOS; $n(E,\, x) = -\mathrm{Im}\{G(E,\, x)\}$.

$$(\tau_\phi^{nn})^{-1} \propto -\mathrm{Im}\{G^{nn}_{\mathrm{SSH},\infty}(\lambda_\pm)\} = n(\lambda_\pm, n) \tag{4.1.7}$$

Summing the decoherence rate over all sites of the probed SSH chain recovers the full DOS in the SSH chain:

$$\sum_n (\tau_\phi^{nn})^{-1} \propto \sum_n -\mathrm{Im}\{G^{nn}_{\mathrm{SSH},\infty}(\lambda_\pm)\} = \mathrm{DOS}(\lambda_\pm). \tag{4.1.8}$$

The proportionality to the LDOS of the environment as in (4.1.7) is quite reasonable in the context of decoherence dynamics as discussed in Ch. 2. Decoherence is the result of interactions with an environment, and couplings to densely-populated sectors of the environment's energy spectrum should lead to faster decoherence than couplings to an empty or sparse sector. Indeed, (4.1.7) indicates that decoherence will be rapid if $\lambda_\pm$ is chosen near energies populated by the environment at a given site n, with much slower decoherence for couplings at energies not populated by the environment. Lastly, recall that the LDOS explicitly depends on the probability density amplitude of states as seen in (2.2.11); the positional profiles of states can be extracted through a study of decoherence dynamics along the chain.

4.2. Decoherence probe method

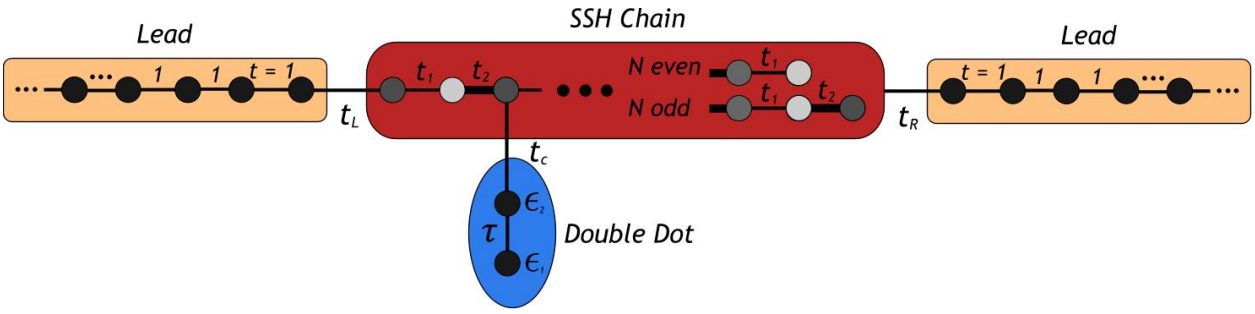

Figure 4.1 – Tripartite system consisting a qubit, an SSH chain, and two leads. Here, the SSH chain is the topological material of interest, where the coupling t_c can be taken on any n^{th} site of the SSH chain.

Unless explicitly stated otherwise in what follows, we consider the tripartite system (with two leads) as shown in Fig. 3.1 and shown again here in Fig. 4.1. We know the decoherence rate (4.1.1) is a function of the eigenvalues $\lambda_\pm$ of the isolated TLS and the coupling site n between the TLS and the SSH chain of length N. One can then study decoherence dynamics by varying the position and energy of the TLS; this will be the basis for the proposed probe.

The proportionality of the decoherence rate to the LDOS means a judicious choice of $\lambda_\pm$ can reveal information on the states of the environment. We propose the following steps to sweep along the chain and study the LDOS via our decoherence probe:

(1) Initialize a TLS coupled to a site n such that it possesses an eigenvalue λ_+ or λ_- tuned to an energy of interest in the SSH chain.

(2) Let nature run its course and allow the TLS to decohere, measuring the decoherence rate.

(3) Translate to site $n+1$ and repeat steps 1 & 2 to sweep through the entire SSH chain.

Such a dataset can be used to generate LDOS profiles of the probed environment at the probed energy by plotting the decoherence rate as a function of position. Additionally, summing over all positions leads to a DOS measurement at the probed energy, with the possibility of generating a DOS plot by repeating a sweep at various energies.

4.3. Probing SSH edge states

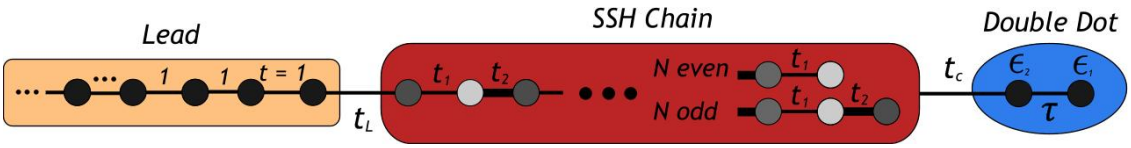

Figure 4.2 – Tripartite system with a surface TLS-environment coupling fixed at the N^{th} site.

Let us discuss the study of SSH edge states in various configurations by use of the decoherence probe, beginning with a review of a co-authored publication [5]. In this paper, *Detecting topological edge states with the dynamics of a qubit*, the decoherence rate of a double dot coupled to the end of an SSH chain with a single lead, as shown in Fig. 4.2, was studied. Only the surface component of the Green's function, $G^{NN} = G^S$ is required for a coupling to the end site of the SSH chain. As a single lead is considered, we need not distinguish the left and right sides and simply write Σ_∞ for the semi-infinite lead's self-energy. It is easy to verify that for $n = N$ and $\Sigma_R = 0$, the surface Green's functions

$$G^S_{\mathrm{SSH},\infty}(E) = \begin{cases} \dfrac{t_2(t_2 s_{N-1} + t_1 s_{N+1}) - E\Sigma_\infty s_{N-1}}{t_1 t_2 E s_{N+1} - t_1\Sigma_\infty(t_2 s_{N+1} + t_1 s_{N-1})} & \text{for } N \text{ odd} \\ \dfrac{E t_2 s_N - \Sigma_\infty(t_1 s_{N-2} + t_2 s_N)}{t_2^2(t_1 s_{N+2} + t_2 s_N) - E t_2 \Sigma_\infty s_N} & \text{for } N \text{ even} \end{cases} \tag{4.3.1}$$

follow from the more general expressions (3.2.11) and (3.2.27) for N odd and even, respectively. As (4.3.1) is for a fixed $n = N$, corresponding to the surface coupling, the probe method described in the previous section with translations along n makes little sense here.

Instead, the system is studied varying the length N of the SSH chain to obtain graphs of $(\tau_\phi)^{-1}$ vs N as in Fig. 7 and Fig. 8 of [5], reproduced below in Fig. 4.3. Since (4.1.1) is the minimum of two rates, we expect non-monotonous behaviour when the minimal contribution crosses over from λ_+ to λ_- (or λ_- to λ_+). As one expects from interpreting the decoherence rate expression, decoherence is significantly hastened when the LDOS is high. Tuning the qubit at $\lambda_- = 0$ permits a study of the decay rate of a qubit decohering via a coupling to edge states, if present. The case where λ_+ is resonant with the SSH chain bulk states is discussed in 4.4.4. Recall that for N even, a pair of edge states exists for $r < r_C$, while for N odd an edge state always exist but localizes on the left (right) for $r < 1$ ($r > 1$). From Fig. 4.3, we observe that when N is even (red), the TLS shows quick decoherence for $r < r_C$ when edge states are present. For $r > r_C$ when edge states no longer exist, decoherence is exponentially suppressed as a function of N for appreciably large N (starting around $N \approx$ 20-30). We expect this suppression because an SSH chain is a bulk insulator and increasing the length N of the chain corresponds to a large potential barrier preventing the TLS from decaying into the lead via tunneling through the SSH chain. This non-monotonous transition can be understood from (4.1.1) due to the crossover from a bulk frequency λ_+ to the mid-gap energy $\lambda_- = 0$ as yielding the slowest decay. For N odd, we observe rapid decoherence when the edge state is adjacent to the TLS ($r > 1$), but suppressed decoherence when the edge state is on the opposite end of the chain ($r < 1$). Even though an edge state is present for $r < 1$, its localization far from the TLS and its exponential fall-off in the bulk means the TLS effectively cannot *see* the edge state; the $E = 0$ LDOS near the TLS is near zero and the suppression as a function of N is attributed to the insulating properties of the SSH chain, as we observed for even N when $r > r_C$.

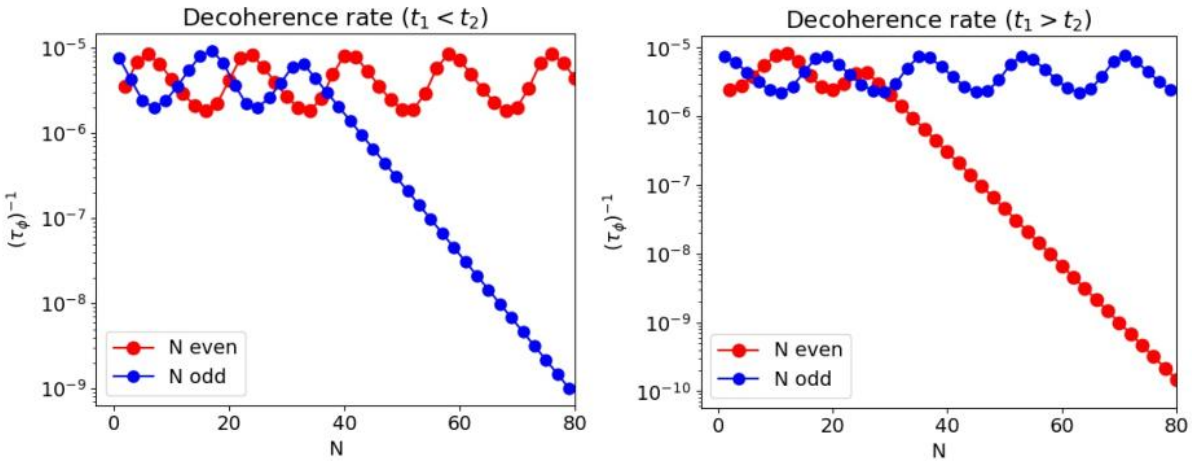

Figure 4.3 – Decoherence rate as a function of the SSH chain length, N. The above plots are for $(\epsilon_1, \epsilon_2, \tau) = (0.402235, 0.002235, 0.03)$, yielding $\lambda_- = 0$ and $\lambda_+ = 0.4044$. The SSH chain parameters are $t_1 = 1.1$, $t_2 = 1/t_1$ for $t_1 > t_2$ and $t_2 = 1.1$, $t_1 = 1/t_2$ for $t_1 < t_2$.

Ultimately, it is concluded that a TLS is sensitive to adjacent topological edge states, allowing one to infer the presence or absence of edge states based on the decoherence rate dynamics. We observe a large variation in decoherence rates based on the presence or absence of edge states for large N; for instance, there are approximately 5 orders of magnitude in decay rate suppression for $N \approx 100$. Additionally, the decoherence probe can differentiate the cases of the two distinct odd-N edge states and shows the ability to infer which boundary the edge state is present on, something conventional transmission probes cannot do.

4.3.1. Decoherence probe, N even

The probe coupled to the end of the SSH chain detects the presence or absence of edge states. We now see how, by moving the probe along the length of the SSH chain, one can map out the profile of edge states. Considering the decoherence of a TLS coupled at an arbitrary site n as per the $G^{nn}_{\mathrm{SSH},\infty}$ expressions (3.2.28) and (3.2.29), we apply the method described in Section 4.2 to obtain a full sweep of the SSH chain in the tripartite system. Prior to showing the decoherence plots, a quick refresher of edge states is given: for N even, edge states exist for the topological phase defined by $r < r_C$. These states come in near-zero-energy pairs and are localized at the boundaries of the SSH chain. These states *appear* confined to a given sublattice, with edge states near the left edge effectively existing on odd sites only, and on the right edge on even sites only as shown in Fig. 1.6. This is misleading because the edge states hybridize in the bulk, meaning they are not globally confined to any given sublattice. This is a result of chiral symmetry, where states tend towards sublattice confinement as $E \to 0$. Having energies very near zero also implies a profile which tends towards exponential localization (with purely exponential profiles possible only if $E = 0$). Fig. 4.4 shows the near-exponential envelope of the physical amplitude for an even-N SSH chain edge state decomposed into even and odd sites – note the sharper-than-exponential cutoff at the chain boundaries.

The TLS eigenvalues will dictate what energies we are probing in the LDOS of the environment, as was discussed in Section 4.1. With the objective of studying the topological edge states of an even-N SSH chain, we initialize the qubit such that it has eigenvalues corresponding to the edge states, including influence from the leads. As the Green's functions $G^{nn}_{\mathrm{SSH},\infty}(E)$ are symmetric, we need not worry about the sign of the edge state energy we input; these states come as chiral partners of equal and opposite energy with identical amplitudes $|\psi_{\mathrm{edge}}|^2$ and will yield identical decoherence rate measurements. A plot of the decoherence rate as a function n for the same configuration as Fig. 4.4 ($N = 82$, $r = 0.826$) is shown in Fig. 4.5. In order to understand different contributions to the decoherence rate, both $\lambda_\pm$ terms from (4.1.1), as well as the minimum of the two, will be displayed.

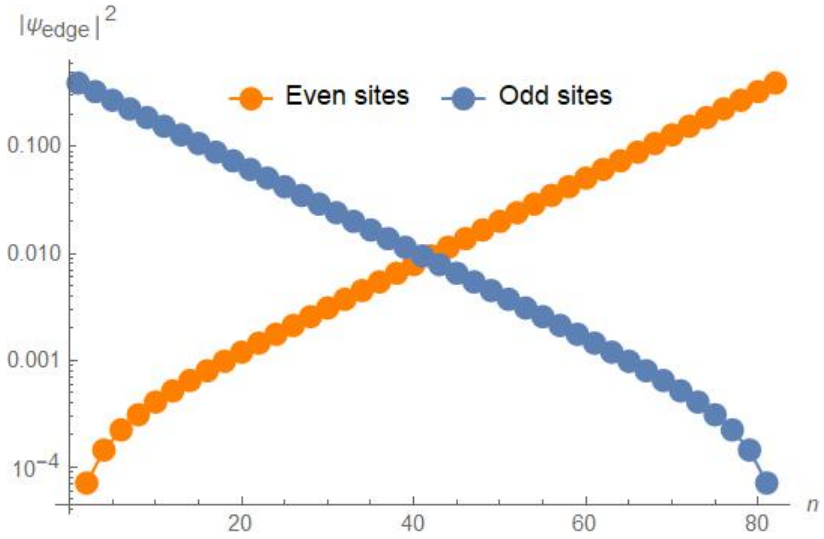

Figure 4.4 – Semi-log plot of the density of near-zero energy ($E_\pm \approx \pm 0.0001496$) edge states for a pure SSH chain of length $N = 82$. Edge states have the largest penetration into the bulk for r less than but close to r_C. The states shown above are for $r = 0.826$ where $r_C = 0.976$. This choice of r relatively near r_C is voluntary to show deviations from an exponential profile. For $r = 0.5$, for example, the profiles appear, at least visually, exponentially localized on the even/odd sublattices.

We note a stark contrast in the behaviour of both decay contributions, $\lambda_\pm$. This is expected because for $N = 82$ and $r = 0.826$, the bulk bands range from energies $\pm\{0.1909\text{-}2.009\}$. The $\lambda_+ = 0.4044$ contribution to the decay rate is then associated with the LDOS sampled in the bulk, which is oscillatory in nature. On the other hand, the $\lambda_- = 0$ term shows exponential behaviour as a function of n. The choice of $\lambda_- = 0$, rather than the expected near-zero energy for even-N edge states, is the result of including lead self-energies in our effective description of the SSH chain coupled to an environment. As we have discussed in Section 2.2.2, interactions broaden the peaks of the DOS. As can be seen in Fig 4.6, this broadening leads to a convolution of the two even-N edge states at $E = 0$, justifying our use of $\lambda_- = 0$. This choice of energy naturally causes a purely exponential behaviour, and we lose the beyond-exponential suppression visible in Fig. 4.4. Nonetheless, it remains possible to observe profiles corresponding to pure SSH states in certain system configurations, as will be discussed in Section 4.4.3. The influence of the semi-infinite leads on the SSH chain eigenvalues and DOS is discussed further in Section 4.5.

Returning to our analysis of the λ_- contributions in Fig. 4.5, we see that, near the left (right) edge, decoherence is rapid on odd (even) sites and gets suppressed as one moves into the bulk. Coupling the TLS to an edge state where it has a large amplitude leads to a faster decoherence. Additionally, even- (odd-) site decoherence is heavily suppressed in the vicinity of the left (right) edge. This is related to the fact edge states have near-zero amplitude on these sites. These behaviours are in agreement with edge states which tend

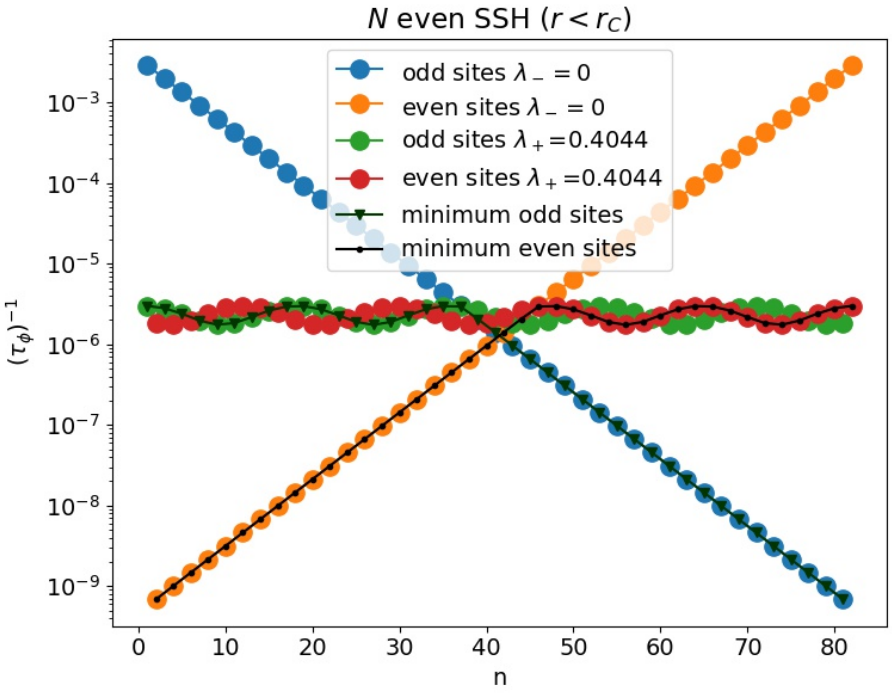

Figure 4.5 – Decoherence rate as a function of position along an SSH chain of length $N = 82$. The TLS is initialized with parameters $(\epsilon_1, \epsilon_2, \tau) = (0.402235, 0.002237, 0.03)$, yielding $\lambda_- = 0$ and $\lambda_+ = 0.4044$. Coupling parameters are taken $t_c = 0.035$ and $t_L = t_R = 0.65$. SSH parameters are taken such that $t_1 < t_2$ for $r < r_C$, with $t_2 = 1.1$ and $t_1 = 1/t_2$.

towards sublattice confinement as their energy becomes small. Ultimately, the decoherence rate expression for the long-time evolution is given by the minimum of both $\lambda_\pm$ rates, as shown by the dark solid lines with small circle/triangle markers. The probe decoheres too quickly and is therefore not sensitive to the edge states where their amplitude is maximal (i.e. at the edges), and instead samples bulk behaviour. It remains possible to detect these edge states by seeking out exponential decay of the LDOS deeper in the bulk where the lower amplitude of the edge states yields smaller decoherence rates. We conclude that the decoherence probe is sensitive to the topological edge states of an even-N SSH chain.

4.3.2. Decoherence probe, N odd

The decoherence probe is now used to study odd-N SSH chains. We begin by reviewing the properties of odd-length SSH chains for which there always exists an edge state. The localization of this edge state can vary, with a left (right) edge state for $r < 1$ ($r > 1$) as was shown in Fig. 1.8. Recall that these edge states are pinned to the mid-gap at $E = 0$ and are always confined to the odd sublattice with an exponential fall-off into the bulk as described

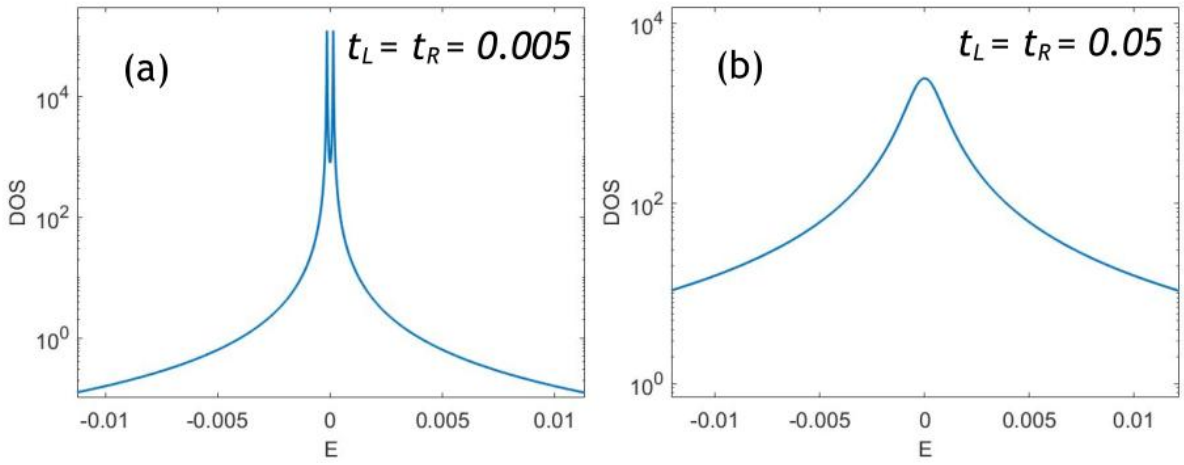

Figure 4.6 – Density of states plot around $E = 0$ for the SSH chain ($N = 82$, $t_2 = 1.1$, and $t_1 = 1/t_2$) coupled to two leads by coupling parameters t_L and t_R. (a) For small couplings, broadening takes place but the peaks corresponding to edge state eigenvalues remain defined. (b) Increasing external couplings causes further broadening and leads to a single coalesced peak at $E = 0$.

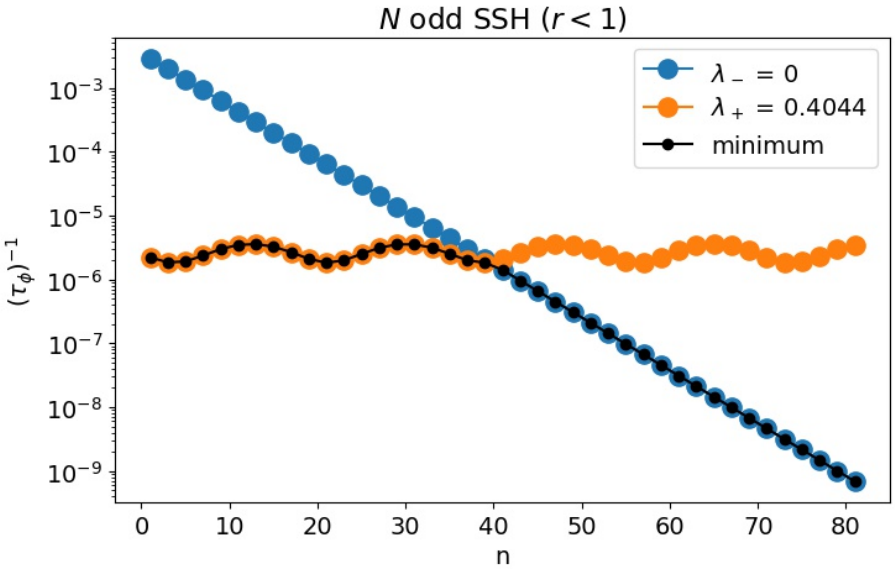

Figure 4.7 – Decoherence rate as a function of odd-site position along an SSH chain of length $N = 81$ with a left edge state. The TLS is initiliased with parameters (ϵ_1, ϵ_2, τ) = (0.402235, 0.002235, 0.03), yielding $\lambda_- = 0$ and $\lambda_+ = 0.4044$. Coupling parameters are taken $t_c = 0.035$ and $t_L = t_R = 0.65$. SSH parameters are taken such that $t_1 < t_2$ for $r < 1$, with $t_2 = 1.1$ and $t_1 = 1/t_2$.

by (1.1.32). As the edge state exists only on odd sites, we will consider a sweep of the odd sites of an SSH chain, tuning the TLS to $\lambda_- = 0$ to probe the edge state.

A decoherence plot for $N = 81$ and $r < 1$ is shown in Fig. 4.7. The λ_+ contribution to the decoherence rate is again oscillatory from coupling to bulk states. For the $\lambda_- = 0$ term, we observe fast decoherence on the left edge and an exponentially suppressed decoherence rate as one travels through the bulk on odd sites, indicative of a zero-energy state localized at the left edge.

The plot for the decoherence rate for $N = 81$ and $r > 1$ is shown in Fig. 4.8. Again, we see oscillatory contributions from the eigenvalue coupling to the bulk. The λ_- contribution here shows fast decoherence on the right side of the chain and a suppressed decoherence rate away from the right edge. This plot is, in all respects, simply a mirrored version of the case for $r < 1$ discussed above. We conclude that the decoherence probe is sensitive to the right edge state of an odd-N SSH chain.

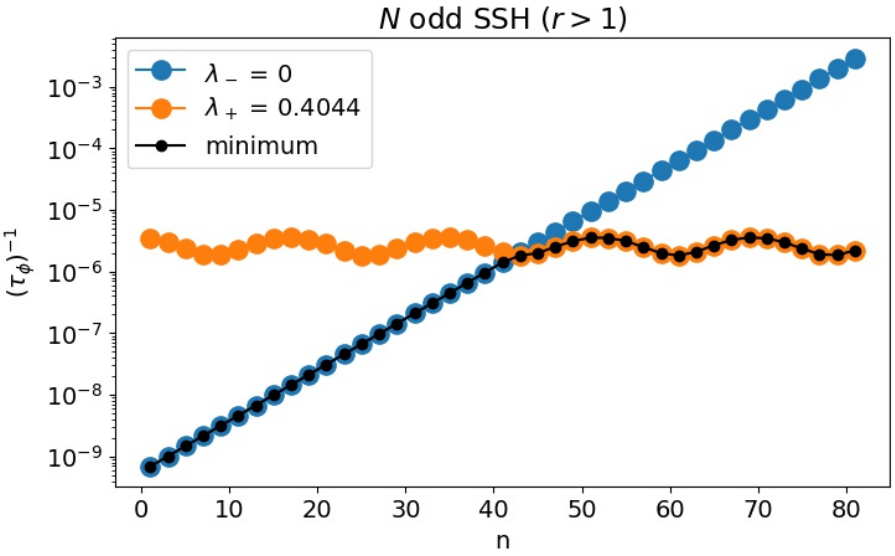

Figure 4.8 – Decoherence rate as a function of odd-site position along an SSH chain of length $N = 81$ with a right edge state. The TLS is initiliased with parameters (ϵ_1, ϵ_2, τ) = (0.402235, 0.002235, 0.03), yielding $\lambda_- = 0$ and $\lambda_+ = 0.4044$. Coupling parameters are taken $t_c = 0.035$ and $t_L = t_R = 0.65$. SSH parameters are taken such that $t_1 > t_2$ for $r > 1$, with $t_1 = 1.1$ and $t_2 = 1/t_2$.

We have seen that the probe can detect edge states that arise in various configurations of an SSH chain through a study of the probe's decoherence dynamics. This includes the ability to differentiate edges states from even-N and odd-N configurations, as well as the ability to know which boundary the state is localized on in the case of odd-N zero-modes. We note that it is also possible to distinguish topological zero modes from localized interface states using the sublattice confinement of near-zero energy states: Because the SSH model's topological modes are protected by chiral symmetry and chiral in nature, they are localized on a single sublattice. Non-topological interface states can then be discerned from the topological modes

on the basis of having strong support on both even and odd sites of the SSH chain. The direct link between the decoherence rate and the LDOS means the decoherence plots we are studying are proportional to the amplitude profiles of edge states, as shown in Fig. 4.9. This information shows how strongly the edge state is localized and reveals the penetration depth of the edge state into the bulk. This establishes our proposed decoherence probe as a powerful tool to spatially characterize and classify localized states. We stress here that these findings are applicable to a wide array of systems and are not exclusive to the specific system we have studied: the decoherence expression of a TLS (2.5.12) holds for a general environment. As such, other one-dimensional systems which feature localized states, such as the Kitaev chain hosting Majorana zero-modes [22], could be spatially characterized by means of our decoherence probe. Additionally, one could envision a generalization to the probe discussed here by allowing displacement of the probe in two dimensions. Two-dimensional topological materials, which feature edge modes along their perimeter, could then be scanned over their area to study the penetration depth of edge modes. Corner modes, which are topological excitations in 2-d materials confined not to the full edges but only the corners [49], should also be detectable by our decoherence probe. We hope that such probes can become practical tools for the spatial and topological characterisation of states in low-dimensional materials.

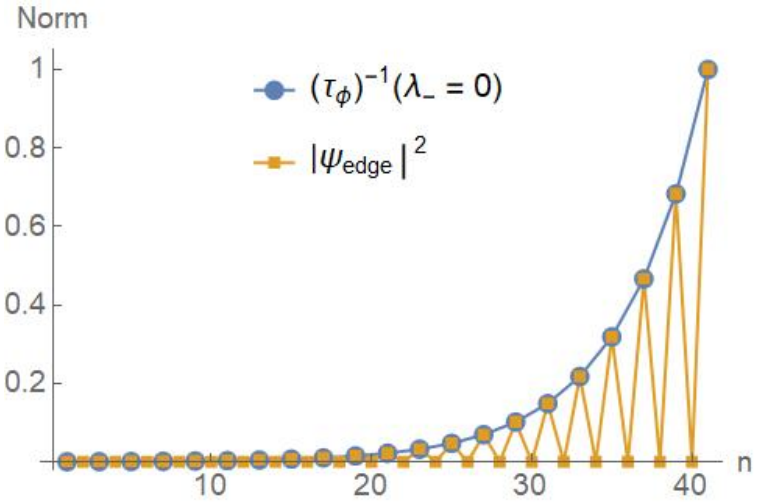

Figure 4.9 – Comparison of the exponential suppression of the decoherence rate at zero energy to the odd-N edge state for $N = 41$ and $r > 1$. Both curves are scaled such that their maximal amplitudes line up. As expected, the decoherence rate has the same decay constant as a function of n as the edge state's amplitude.

While we have interpreted these results from the point of view of quantum sensors aiming to study materials, there is still overlap with quantum computing technologies in this work. Decoherence of the qubit tuned near zero energy is accelerated by the presence of adjacent edge states and suppressed when no edge states are near or when the amplitude of the states is small. We note up to six orders of magnitude in difference in the decoherence rates. This

suppression, a result of the insulator between the qubit and the conducting channel, can be compromised if the insulator possesses edge modes. Localized modes, whether topological in nature or coming from an impurity, are therefore detrimental to the decoherence rate of a qubit. It should therefore be an important consideration when creating quantum computer architectures that no localized surface states be adjacent to qubit couplings. This conclusion, of course, does not affect quantum computing proposals which rely on topological edge states to store information.

4.4. Influence of system parameters

We have shown that the decoherence probe has the power to spatially characterize edge states, with the ability to infer the presence of edge states, to determine which boundary the state localizes on, and to obtain a profile of the decay envelope of the state into the bulk. With this important proof-of-concept out of the way, it can be valuable to study how the decoherence probe is affected by different system parameters.

4.4.1. Influence of coupling constant t_c

We begin by studying the simple influence of the probe-environment coupling at an n^{th} site, t_c. It comes as no surprise that the decoherence rate will vary with some proportionality to the coupling strength with the environment. This can be seen explicitly from (4.1.1) which is proportional to the self-energy,

$$(\tau_\phi)^{-1} \propto -\mathrm{Im}\{\Sigma^{nn}_{\mathrm{SSH},\infty}(\lambda_\pm)\} = -t_c^2\,\mathrm{Im}\{G^{nn}_{\mathrm{SSH},\infty}(\lambda_\pm)\}, \tag{4.4.1}$$

and reveals that $(\tau_\phi)^{-1}$ scales explicitly with t_c^2. Recalling that the decoherence rate approximation (4.1.1) requires $t_c^2 << 1$ to hold, coupling the TLS *strongly* leads to rapid decoherence while *small* couplings are favorable to lower the decoherence rate (see Fig. 4.10).

4.4.2. Impact of hopping parameters t_1 and t_2

Let us now see how the SSH chain parameters affect the decoherence probe. Obviously, the topological phase the system is in will dictate what edge states (if any) are detected by the probe as discussed in the previous section. Still, within a given topological phase, the parameters t_1 and t_2 can have a considerable impact on the probe measurement. Fig. 4.11 shows the $\lambda_- = 0$ contributions to the decoherence rate, the term proportional to the LDOS of a left edge state, for various values of $r < 1$ (the case of $t_2 = 1/t_1$) with $N = 81$.

Upon inspection of Fig. 4.11, we note steep envelopes for small r which gradually get less pronounced for larger r. This behaviour is in agreement with expression (1.1.32), and we expect the edge state will be more localized at small r. As r tends towards 1, the edge state is less confined and has a longer penetration depth into the bulk. In fact, choosing

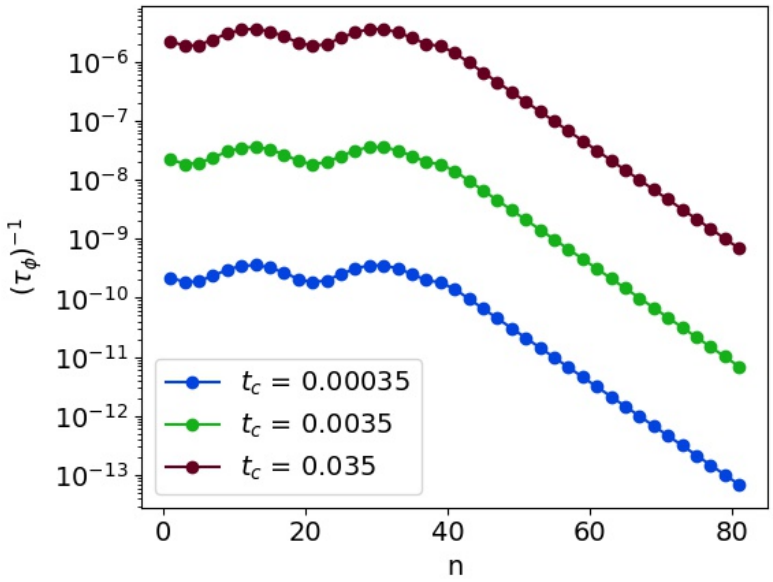

Figure 4.10 – Decoherence rate $(\tau_\phi)^{-1}$ for $N = 81$ and $r = 0.8$ with TLS parameters (ϵ_1, ϵ_2, τ) = (0.402235, 0.002235, 0.03), shown for three different values of t_c = (0.00035, 0.0035, 0.035).

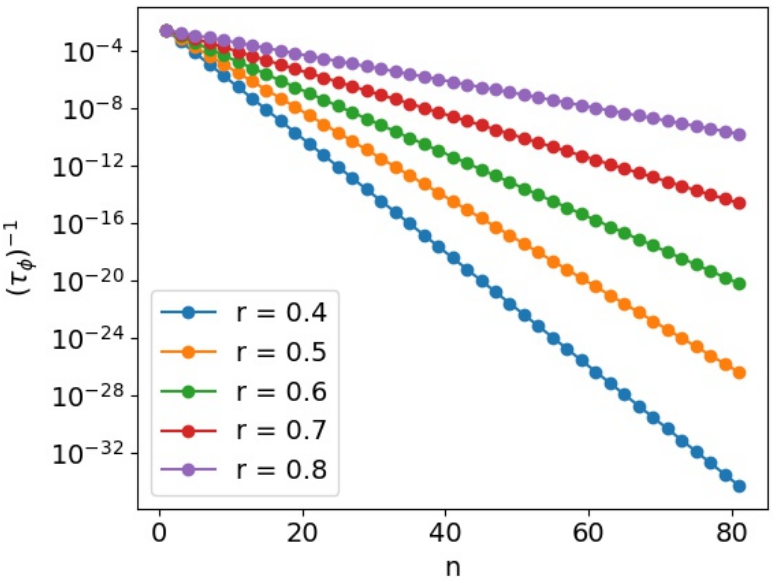

Figure 4.11 – Comparison of the various $\lambda_- = 0$ contributions to the decohrence rate for various values of $r < 1$.

$r = 1$ here would result in a constant decoherence rate at any position; the edge state fully delocalizes and the LDOS is flat along the length of the SSH chain. We conclude that the

hopping parameters' influence on the localization strength to the edges can be examined via the decoherence probe.

4.4.3. Single quantum dot compared to TLS

Thus far, we have made extensive use of a TLS to probe materials. This choice can be traced, in part, to the very natural context for discussing decoherence when working with qubits. Nonetheless, a TLS presents some challenges which we will now address; there are always two contributions to the decoherence rate coming from the two frequencies of the TLS. To deal with this, we have chosen to consider the minimal decay rate contribution as it describes the long-term evolution of the qubit, as discussed in Section 2.5.1. In certain configurations of the tripartite system, the frequency term of interest (often the TLS eigenvalue tuned at, or near, zero energy) corresponds to the faster decay rate and therefore never becomes the minimal contribution, rendering the probe insensitive to such decays. As was observed in Section 4.3.1, tuning the TLS to $\lambda_- = 0$ was necessary due to broadening from the environment which led to a loss of distinct edge state peaks in the DOS. Still, Fig. 4.6(a) shows there exist system configurations for which the edge state peaks remain visible in the DOS. It is perhaps surprising then that we did not consider such systems when probing the LDOS of localized modes in the SSH chain. Fig 4.12 shows the TLS decoherence probe for the same system parameters as Fig. 4.6(a). One notes the λ_- decoherence terms corresponding to the edge state energies now perfectly describe the $|\psi_{\text{edge}}|^2$ profile of the SSH chain edge states (see Fig. 4.4). Yet, these contributions are never the slowest rate and hence $(\tau_\phi)^{-1}$ is dependent only on the oscillatory λ_+ terms. Physically, this reveals that the edge states have large amplitude density and the TLS experiences rapid decoherence at $\lambda_- = 1.41 \times 10^{-4}$. This large amplitude is due to the weak environmental couplings of the SSH chain, $t_L = t_R = 0.005$, which imply minimal hybridization with lead states. Again, the influence of the lead coupling parameters will be discussed in detail in Section 4.5.

The ability to characterize the exact profiles of even-N edge states is of interest and a possible solution to this problem is to swap the TLS, or double quantum dot, for a single quantum dot (SD) as the probe. Indeed, one can consider the simple single-level Hamiltonian,

$$H_{\text{SD}} = \epsilon_1, \tag{4.4.2}$$

resulting in the following effective Hamiltonian for a SD in the tripartite system:

$$H'_{\text{SD}} = \epsilon_1 + \Sigma^{nn}_{\text{SSH},\infty}(E). \tag{4.4.3}$$

Applying the same method used to derive the approximate analytical form for the decoherence rate in Section 2.5.1, we find

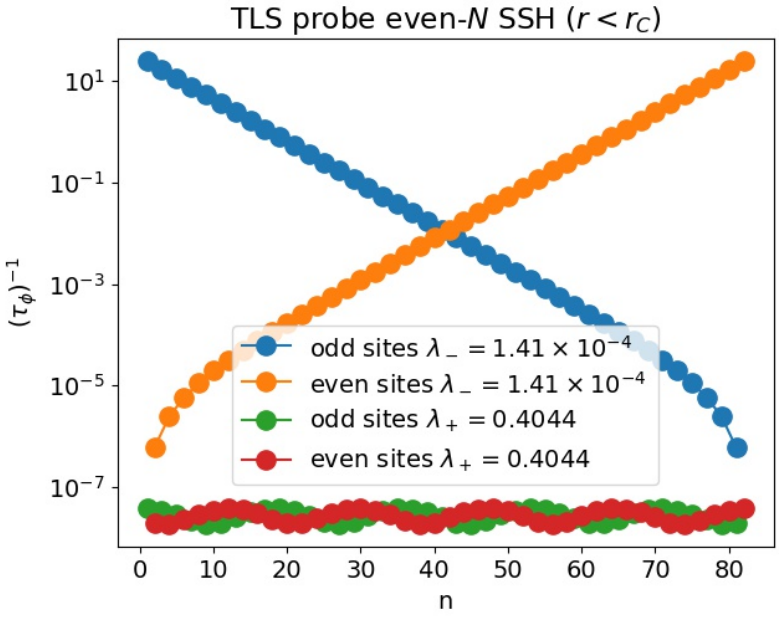

Figure 4.12 – TLS decoherence probe tuned at the eigenvalue of an edge state when broadening does not dominate near $E = 0$. The tripartite system parameters above are (N, t_1, t_2, t_c, t_L)=(82, 1/1.1, 1.1, 0.035, 0.005), where we have used symmetric lead couplings $t_L = t_R$.

$$(\tau_\phi)^{-1} = -\mathrm{Im}\{\Sigma^{nn}_{\mathrm{SSH},\infty}(\epsilon_1)\}. \tag{4.4.4}$$

In some respects, namely the direct proportionality to the LDOS, the SD probe is very similar to the previously discussed TLS probe. On the other hand, it differs in two important ways; first, the δ' term is absent from the rate expression such that the direct proportionality of $(\tau_\phi)^{-1}$ to the LDOS is now always applicable. Secondly, the almost trivial nature of the Hamiltonian implies a single eigenvalue, ϵ_1. This eliminates the necessity to consider the slowest of two decays as was the case for the TLS; the probe will be sensitive to the LDOS at the energy ϵ_1 only. For example, selecting $\epsilon_1 = 0$ would yield an identical decoherence plot to the $\lambda_- = 0$ contribution in a TLS probe without any competition from the bulk oscillatory term λ_+. The SD probe is then of value if sensitivity to the LDOS at a given energy over the entire SSH chain length is desired. This is useful for the study of the LDOS of edge modes at the boundary of the SSH chain, where the bulk term usually dominates. A plot of the SD probe, featuring the complete $|\psi_{\mathrm{edge}}|^2$ profiles, is shown in Fig. 4.13.

We conclude the discussion of the SD probe by addressing how it differs from the TLS probe on a physical level. In our presentation of the TLS probe, we justified decoherence as the dynamical process allowing characterization of the material. We say decoherence occurs due to electrons leaking out from the TLS and carrying correlations out to infinity

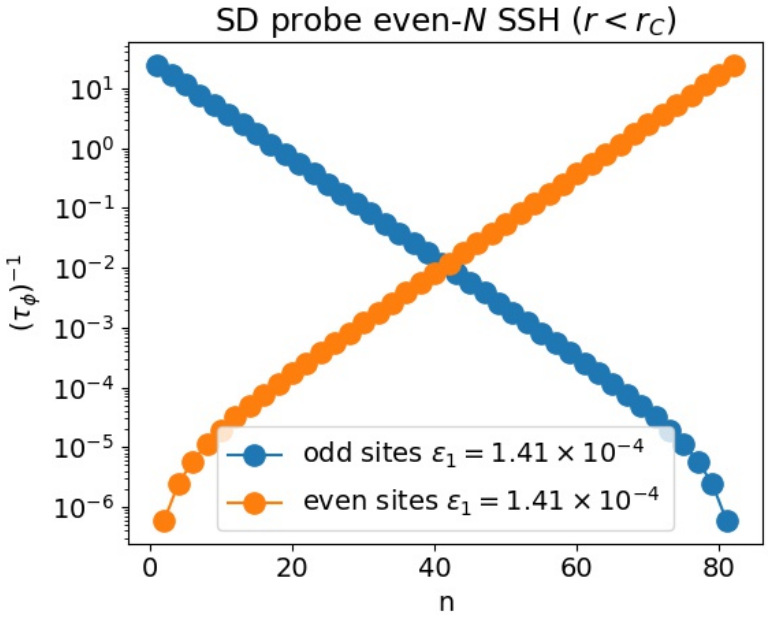

Figure 4.13 – Single quantum dot probe tuned at the eigenvalue of an edge state when broadening does not dominate near $E = 0$. The tripartite system parameters above are identical to Fig. 4.12.

through the leads, delocalizing superpositions and resulting in a suppression of transition probabilities in the TLS. In the case of the SD probe, it is inaccurate to speak of decoherence this way because a suppression in level-transition probability makes little sense for a single-level system. Still, viewing decoherence as the loss of correlations into the environment gives a hint in the right direction; $(\tau_\phi)^{-1}$ for the SD probe is the decay rate associated to the outgoing electron flux leaving the SD.

4.4.4. Fine-tuning of the TLS

Alternatively, it is possible to retain the TLS probe and to accentuate a desired $\lambda_\pm$ contribution within certain limits. This is achieved by appropriately tuning the TLS eigenvalues. Near-zero-energy TLS probes decohere very rapidly near edge states where the LDOS is high. This frequently leads to situations where the edge state contribution is hidden, in part or fully, by the bulk oscillations attributed to λ_+ which decohere at a slower rate, as was shown in Fig. 4.12. Previously, we arbitrarily initialized the TLS such that $\lambda_+ = 0.4044$. A more judicious choice can be made by tuning λ_+ in resonance to a bulk band eigenvalue where the DOS and LDOS is high, such that the λ_+ decay rate competes with the λ_- rate. We reproduce Fig. 4.12 tuning $\lambda_+ = 0.3135$, corresponding to a densely-populated eigenvalue of the SSH chain, in Fig. 4.14. This resonant tuning manipulation is not possible in all system configurations and requires knowledge of the DOS of the coupled SSH chain but

provides, when possible, the ability to obtain accurate even-N edge state profiles with the TLS decoherence probe.

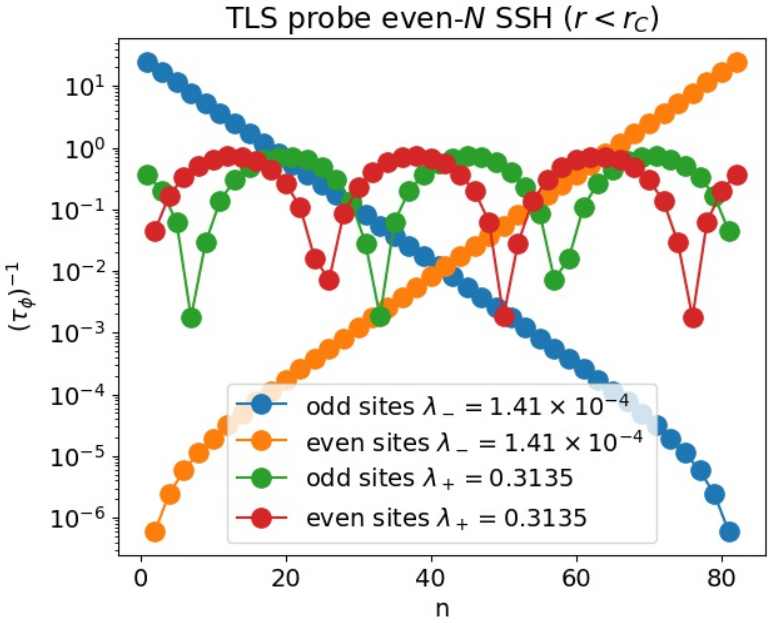

Figure 4.14 – Fine-tuned TLS probe with λ_+ tuned to a densely populated sector of the bulk bands such that the λ_+ and λ_- contribute comparably to the decoherence rate.

4.5. Open system considerations and the influence of lead couplings t_L and t_R

Thus far, we have frequently referred to the influence of the environment on the SSH chain as the cause of level broadening and state suppression through the hybridization of states at the lead interfaces. In this section, we discuss in detail the significant impact the lead coupling parameters have on the nature of the tripartite system. The leads naturally influence the decoherence probe but their form hints at something deeper; the self-energies $\Sigma_{L,R}(E)$ in our effective Hamiltonian open the door to non-Hermitian quantum mechanical effects. We stress here this effective description remains exact in the subspace of the SSH chain. The aim in this final section is to make sense of various quirky behaviours that arise from lead couplings.

The effective Hamiltonian for an SSH chain coupled to a lead at each end is given by

$$H_{\mathrm{SSH},\infty}(E) = \begin{pmatrix} \Sigma_L(E) & t_1 & 0 & \cdots & 0 \\ t_1 & 0 & t_2 & \ddots & \vdots \\ 0 & t_2 & \ddots & \ddots & 0 \\ \vdots & \ddots & \ddots & 0 & t \\ 0 & \cdots & 0 & t & \Sigma_R(E) \end{pmatrix}, \tag{4.5.1}$$

where $\Sigma_{L,R}(E)$ are the self-energies of the left and right leads, respectively, which take the form of complex on-site potentials in the tight-binding Hamiltonian. Recall that the final hopping parameter t in (4.5.1) is t_1 for an even chain and t_2 for an odd chain. A schematic representation of this on-site potential for N even is shown in Fig. 4.15. We note other works have used similar approaches to consider complex on-site potentials on an SSH chain [50, 51, 52, 53]. Unless explicitly stated otherwise in what follows, we will consider two leads with symmetric couplings $t_L = t_R$ and will simply refer to t_L when discussing the lead coupling parameters.

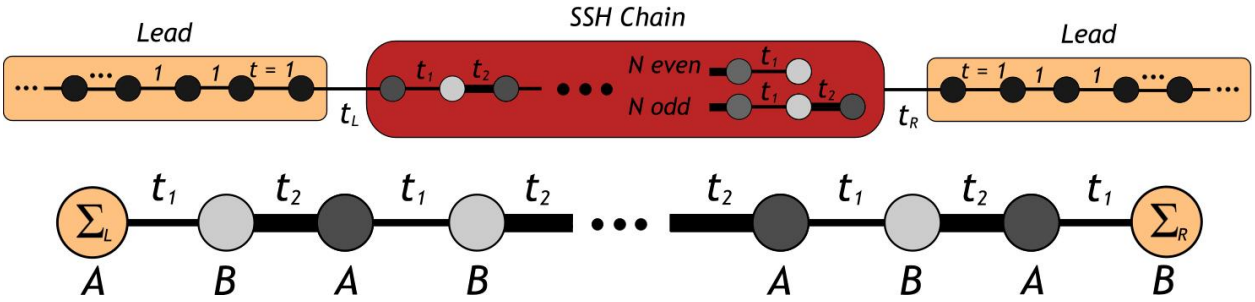

Figure 4.15 – SSH chain featuring complex on-site potentials at each boundary. A visualization of the full (infinite) system is juxtaposed to the finite (for N even) effective description of the system.

We previously paid little attention to the full implications of such a non-Hermitian Hamiltonian. Note that $H_{\mathrm{SSH},\infty}(E)$ is now energy-dependent. As such, the solution of the eigenvalue problem $H(E)|\psi\rangle = E|\psi\rangle$ is no longer linear and self-consistent eigenvalues must be found numerically. Additionally, the Hamiltonian contains complex terms from the self-energies which produce complex eigenvalues. Evidently, the complex self-energies make it such that $H_{\mathrm{SSH},\infty}(E)$ is non-Hermitian. This non-Hermitian description proves useful in the study of open quantum systems, often called dissipative quantum systems.

To address the issue of an energy-dependent Hamiltonian, we simply resort to numerical solutions of the determinant relation

$$\det\left(H_{\mathrm{SSH},\infty}(E) - E\right) = 0, \tag{4.5.2}$$

to find self-consistent energy solutions. For the finite systems we consider, this calculation remains reasonably efficient. The closed system ($t_L = 0$) is Hermitian and features a real spectrum, while the open system ($t_L \neq 0$) has energies taking on complex values. We note that the structure of the energy spectrum along the real axis remains mostly the same for both systems; we principally observe a shift towards imaginary values in the non-Hermitian case. More exotic behaviour, such as bifurcations as a function of the environmental coupling t_L, that can bring about important deformations of the energy spectrum are currently being investigated and are left for future work.

It is useful, for conceptual reasons, to understand what complex energies imply with respect to the physics of our system and we now introduce the concept of resonant states in open systems. Consider a segment Ω of length L on which a nonzero potential exists. A resonant state can be defined as a solution to the Schrödinger equation such that only outgoing waves can exist outside of the segment Ω. Defined in this manner, resonant states are an appropriate form to study dissipation in open systems. Some important features of resonant states which we now mention are derived in [54].

First, the number of particles in a resonant state is conserved if one accounts for an expanding volume; decays are problematic to probabilities only if one considers states solely in the segment Ω. Quantum mechanics requires the conservation of probabilities and one is always able to obtain this by looking at the full system particles are decaying out to. It is only in a local subsystem basis where the Hamiltonian is characterized by non-Hermiticity that dissipative effects can manifest as non-conserved probabilities. Of great importance to us, it is shown that the imaginary component of the energy is proportional to the outgoing momentum flux for arbitrary wavefunctions. In the case of an individual resonant state, this reduces to the lifetime (or the half-width) of the state. Resonant states are outgoing waves by definition and have strictly negative imaginary energy components. States with positive imaginary energies can be classified as anti-resonant and corresponds to states with only incoming waves at the segment Ω boundaries.

In our context, the open system consists of an SSH chain coupled to two semi-infinite leads via effective potentials. In reality, the full system, described by an infinite-dimensional Hamiltonian, is a closed system where probabilities are conserved and energies are real. Open system solutions feature both positive and negative imaginary components, corresponding to anti-resonant and resonant states, respectively. This allows us to draw an interesting parallel to the DOS discussion of Section 2.2.2; the broadening observed in the DOS can be directly linked to the complex-valuedness of the eigenvalues, where the widths of the broadened DOS peaks are proportional to the magnitude of the imaginary parts of the energy of a given state. We note that the edge states ($\mathrm{Re}\{E\} = 0$) have large $\mathrm{Im}\{E\}$. This implies that edge states undergo significant hybridization at the interface and will be strongly broadened due to proximity effects from the leads.

4.5.1. *Ghost* states and lead hybridization

We now return to how the lead parameters modify the SSH chain and, hence, modify the LDOS probed by the TLS (or SD). It may seem surprising that, after an in-depth discussion of the decoherence probe tuned with purely real energies, we reveal that the energy solutions to the open SSH system are actually complex. This *conundrum* is resolved by recalling the weak-coupling approximation we imposed on the TLS and the SSH chain to obtain our analytical expression for $(\tau_\phi)^{-1}$ in Section 2.5.1; the decoherence rate effectively samples the LDOS at the energies of the isolated TLS, given that $t_c^2 << 1$. The isolated TLS eigenvalues, $\lambda_\pm$, are real by construction and so tuning $\lambda_\pm$ to $\mathrm{Re}\{E\}$ when $E \in \mathbb{C}$ is the appropriate approach. Furthermore, we have seen that the interpretation of an imaginary energy is akin to an outgoing momentum flux or a decay lifetime, making it an intimately related yet distinct concept to the real energy. While the non-Hermiticity and complex nature of the eigenvalues do not invalidate previous results, these features can cause variations in the decoherence probe response which are important to understand.

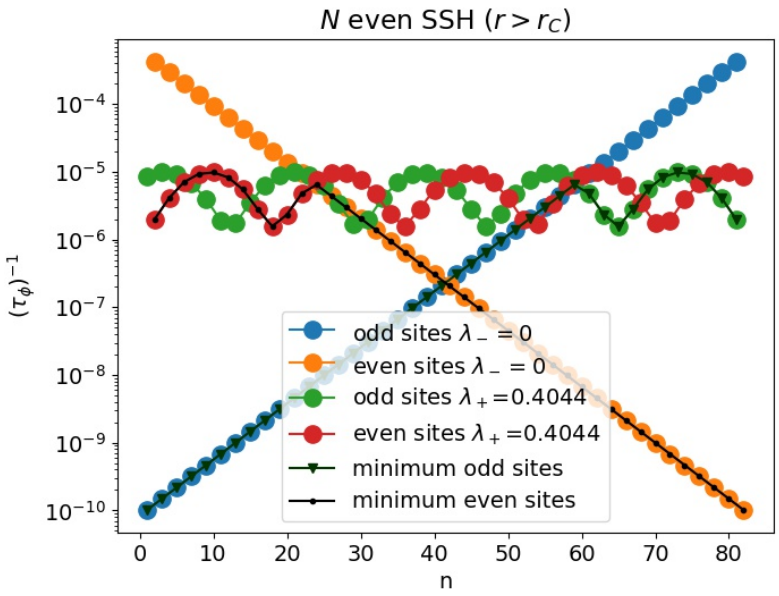

Figure 4.16 – Decoherence rate as a function of position along an SSH chain of length $N = 82$. The TLS is initialized with parameters $(\epsilon_1, \epsilon_2, \tau) = (0.402235, 0.002237, 0.03)$, yielding $\lambda_- = 0$ and $\lambda_+ = 0.4044$. Coupling parameters are taken $t_c = 0.035$ and $t_L = t_R = 0.65$. SSH parameters are taken such that $t_1 > t_2$ for $r > r_C$, with $t_1 = 1.1$ and $t_2 = 1/t_1$.

Recall that in our analysis of the even-N SSH chain decoherence probe, the topological phase $r < r_C$ was the only phase shown. This choice was logical as $r < r_C$ is required for an even length SSH chain to host edge states. Still, a full description of the probe should also include what is measured when no edge states are present, that is, in the non-topological

$r > r_C$ phase. On the other hand, the SSH chain with odd N was previously studied with the decoherence probe for its two topological phases $r > 1$ and $r < 1$ which both feature a single edge state. As the edge state is of zero energy, it is confined to a single sublattice – the odd sites. Note how previous decoherence plots only probed the odd-site LDOS (Figs. 4.7, 4.8) to highlight the edge state. Considering a realistic probe applied to the study of a material, it is not necessarily reasonable to sample only a given sublattice; the probe would be swept continuously and we expect contributions from both even and odd sites.

With this motivation for *realism* in mind, we now study the non-topological phase of the even-N SSH chain as well as the even sublattice in an odd-N SSH chain by means of our decoherence probe. Beginning with the even-N chain, Fig. 4.16 shows the decoherence probe measurement of the non-topological phase $r > r_C$. Inspecting this plot superficially, we observe similar behaviour to Fig. 4.5, with the $\lambda_- = 0$ contributions describing exponentially localized modes. This is unsettling, as no topological edge states should exist in this phase of the SSH model. Upon closer review, we note an important difference to Fig. 4.5; the zero-energy localized modes of Fig. 4.16 are located on the *wrong* sublattice and reach their maximal amplitude one site away from the SSH chain boundary (maximal at $n = 2$ and $n = N - 1$). We know the topological edge states are maximal at the SSH chain boundaries ($n = 1$ and $n = N$); decoupling the even and odd site LDOS should therefore lead to the odd site amplitudes as localized on the left edge, and the even site amplitudes as localized on the right of the SSH chain yet we see the opposite for $r > r_C$. Overall, the decoherence probe reveals surprising behaviour for $r > r_C$ and hints at the existence of localized states that appear confined to the wrong sublattice. Analogous emergent localized features will be detailed for odd-N SSH chains before we analyze and interpret these behaviours.

The decoherence probe applied to all sites for the odd-N SSH chain yields Figs. 4.17 and 4.18 corresponding to the $r < 1$ and $r > 1$ phase, respectively. The odd-site decoherence rates are unchanged from those of Figs. 4.17 and 4.18, showing a bulk oscillatory term and a state exponentially confined to the right (left) edge for $r > 1$ ($r < 1$). The inclusion of even sites to the probe measurement introduces a zero-energy localized feature which resides near the boundary opposite to the edge state. This zero-energy localized mode is maximal at $n = 2$ for $r > 1$ or $N - 1$ for $r < 1$. Recall that for an isolated SSH chain, chiral symmetry enforces that zero-energy states are confined to a single sublattice of the chain. In other words, the even sites of the isolated odd-N SSH chain at zero energy are forbidden and should have strictly null amplitudes.

To understand how and why these localized zero-energy modes arise, it is useful to recall the schematic representation of the effective open system as in Fig. 4.15. We will consider two values of the lead coupling parameter which shed some light on the observed zero-energy modes, as was done in [53]. First, we consider $t_L \to 0$ which causes the on-site self-energy term to tend to zero and we recover an isolated SSH chain of length N as in Fig. 4.19(a). This

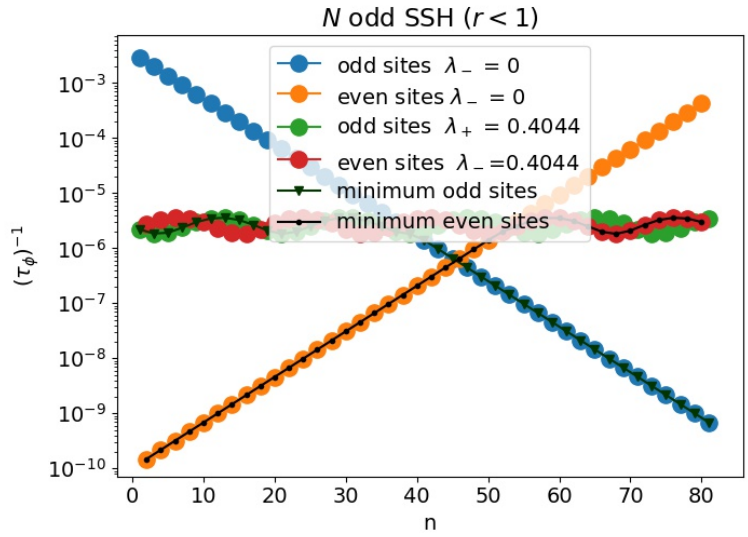

Figure 4.17 – Decoherence rate as a function of position along an SSH chain of length $N = 81$. The TLS is initialized with parameters $(\epsilon_1,\ \epsilon_2,\ \tau) = (0.402235,\ 0.002237,\ 0.03)$, yielding $\lambda_- = 0$ and $\lambda_+ = 0.4044$. Coupling parameters are taken $t_c = 0.035$ and $t_L = t_R = 0.65$. SSH parameters are taken such that $t_1 < t_2$ for $r < 1$, with $t_2 = 1.1$ and $t_1 = 1/t_2$.

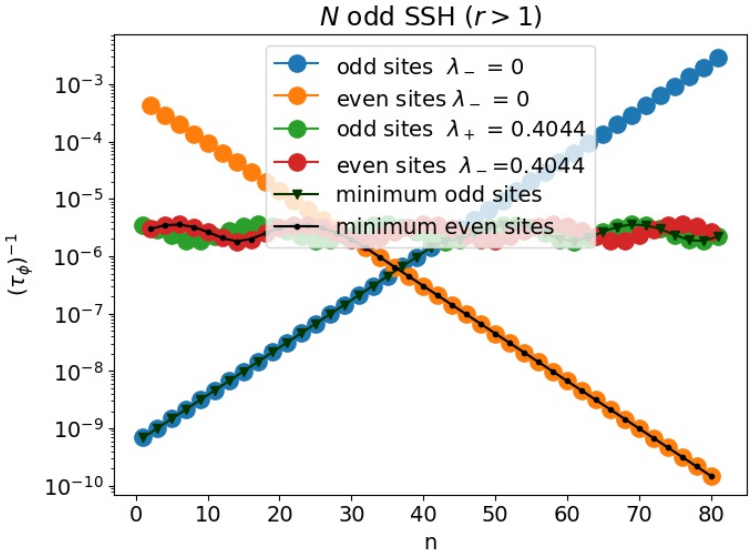

Figure 4.18 – Decoherence rate as a function of position along an SSH chain of length $N = 81$. The TLS is initialized with parameters $(\epsilon_1,\ \epsilon_2,\ \tau) = (0.402235,\ 0.002237,\ 0.03)$, yielding $\lambda_- = 0$ and $\lambda_+ = 0.4044$. Coupling parameters are taken $t_c = 0.035$ and $t_L = t_R = 0.65$. SSH parameters are taken such that $t_1 > t_2$ for $r > 1$, with $t_1 = 1.1$ and $t_2 = 1/t_1$.

states the obvious; removing the lead terms, we recover an isolated SSH chain and expect to see only the SSH chain edge states. Next, let us consider $t_L \to \infty$. This is equivalent to infinite on-site potentials at each end site of the SSH chain. This strong potential effectively

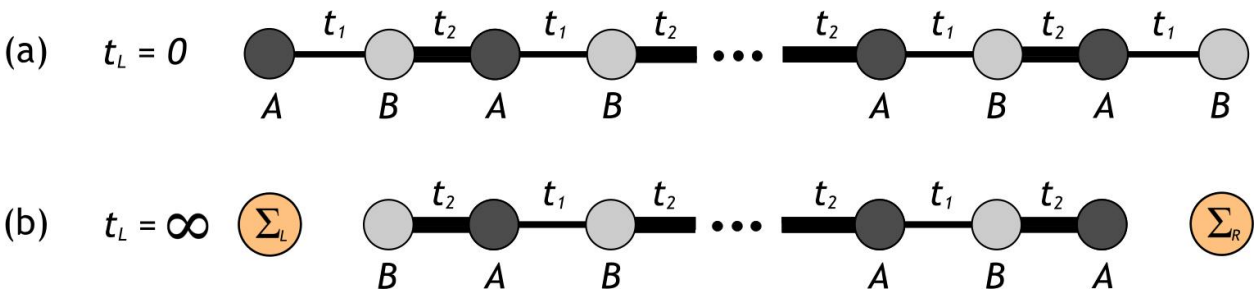

Figure 4.19 – Schematic of two limiting cases of the coupling parameter to the leads, t_L. (a) Shows the trivial coupling $t_L = 0$ leading to an isolated SSH chain. (b) Shows the effective isolated SSH chain of length $N-2$ of opposite topology to (a).

decouples an SSH chain segment from the two infinite potentials resulting in an isolated SSH chain of length $N-2$ as shown in Fig. 4.19(b). Upon removing the first and last site of the N-site SSH chain, the $N-2$ isolated segment will feature a reversed topology.

From this, we gain a qualitative picture on how the interface, mediated by t_L, affects the localized modes in the tripartite system; the leads perturb the boundaries of the SSH chain, resulting in localized states which can exist in sub-regions of an SSH chain, even when the full chain is in a non-topological phase. Returning to Fig. 4.16, we explain the localized modes for $r > r_C$ as edge states with support on the shortened SSH segment of length $N-2$ which has an effective topological phase $r' = 1/r < r_C$. This explains both how these edge states have support on the topologically trivial full-length SSH chain, and additionally justifies why we observe these states on the *wrong* sublattice; the states are indeed maximal at the boundaries of the $N-2$ chain, where the first site is $n = 2$ and the last site $n = N-1$. The even-N system leads to a pair of edge states on either the full SSH chain for $r < r_C$ at small $t_L < 1$ or a pair of edge states that arise on the $N-2$ central segment of the chain for $r > r_C$ at large $t_L > 1$. Similarly, we note that the even-site zero modes in the odd-N decoherence plots shown in Figs. 4.17 and 4.18 are also explained by considering the interplay of two simultaneous topological phases due to boundary effects. We will refer to these unexpected emergent states on the $N-2$ segment as *ghost states*. These states can alternatively be viewed as a hybridization with lead states about a defect junction with a disordered sequence of couplings ($t = 1$, t_L, t_1, t_2...). This hybridization can lead to the loss of topological edge states at strong coupling t_L for $r < 1$ and lead to the emergence of ghost states for $r > 1$. In this context, the ghost states can be understood as the topological-like edge states that arise when zero energy continuum states leak into the topological structure of the $N-2$ SSH chain.

These localized modes were observed in [53], where a real potential V was applied at the boundaries rather than the complex potential, $\Sigma^{nn}_{\mathrm{SSH},\infty}(E)$. Additionally, similar states are briefly mentioned in [52] as arising from a pair of $\mathcal{PT}$-symmetric defects at the boundary sites. Of course, our system is not $\mathcal{PT}$-symmetric, but it is easy to see that it can reduce to

one if $\Sigma_L = -\Sigma_R$ act as gain and loss $\pm i\gamma$ terms for a given energy. As such, it is unsurprising we observe similar states in the tripartite system which can be seen as a relaxation of the $\mathcal{PT}$-symmetric system restrictions. Although it is perhaps not yet abundantly clear that these localized modes correspond to actual states, we will offer further justification in what follows. An important difference between the even-N and odd-N case is that, for even-N, there exists either a pair of edge states or a pair of ghost states, while for odd-N one always observes an edge state on the N-length chain with an emergent ghost state on even sites.

To be more quantitative on the behaviour of ghost states, we can study how the LDOS is affected by the SSH chain's external coupling to the environment at $\mathrm{Re}\{E\} = 0$. For any N and n, the Green's functions $G^{nn}_{\mathrm{SSH},\infty}(E = 0)$ are purely imaginary and are then directly proportional to the LDOS. Studying the case of N odd from our analytical expressions for $G^{nn}_{\mathrm{SSH},\infty}(E)$ as given in Section 3.2.5, we find

$$\text{for } N \text{ odd} \quad \begin{cases} G^{nn}_{\mathrm{SSH},\infty}(0) \propto 1/t_L^2 & \text{for } n \text{ odd}, \\ \\ G^{nn}_{\mathrm{SSH},\infty}(0) \propto t_L^2 & \text{for } n \text{ even}. \end{cases} \tag{4.5.3}$$

As the DOS is simply the sum of the diagonal elements, we see from the above that the DOS contributions from odd sites are suppressed as $1/t_L^2$ while the DOS grows as t_L^2 on even sites. This brings up an interesting point; while the coupling to the leads suppresses the amplitude of the topological edge states confined to odd-n sites, it also promotes the presence of ghost states on even sites where no SSH states typically have support. This is in line with our interpretation of ghost states as coming from shifted interfaces. For $t_L \to 0$, the even sites have no ghost states and for odd sites the DOS diverges, corresponding to the discrete delta peaks associated to an isolated SSH chain edge state. For $t_L \to \infty$, odd-site edge states tend to zero while the even-site DOS diverges, confirming that we recover a zero-energy state on the effectively isolated SSH chain of length $N - 2$. We note that the simple proportionalities in (4.5.3) are attributed to the symmetric left and right lead terms in (3.2.11) and (3.2.17). To gain further appreciation of this interplay of the two localized modes, we numerically evaluate the LDOS over the entire spectrum in Fig. 4.20 for a few key values of t_L. Specific system parameters can be found in the figure caption but it is worth pointing out that the scaled leads have a spectrum range $-2 < E < 2$, and we have chosen the SSH chain parameters such that the full energy spectrum is bound between $-1 < E < 1$. Fig. 4.20(a) shows the expected zero-energy left edge state for $r < 1$ with support on odd sites. The presence of a highly broadened right ghost state, maximal on the $(N-1)^{th}$ site and localized on the even sublattice, is already noticeable at small coupling $t_L = 0.05$ in Fig. 4.20(a). Increasing the coupling to $t_L = 0.15$ as in Fig. 4.20(b), we note increased broadening of the left edge state with an increase in the intensity of the ghost state. Next, Fig. 4.20(c) considers $t_L = 1$. This value is special only with respect to the energy scaling

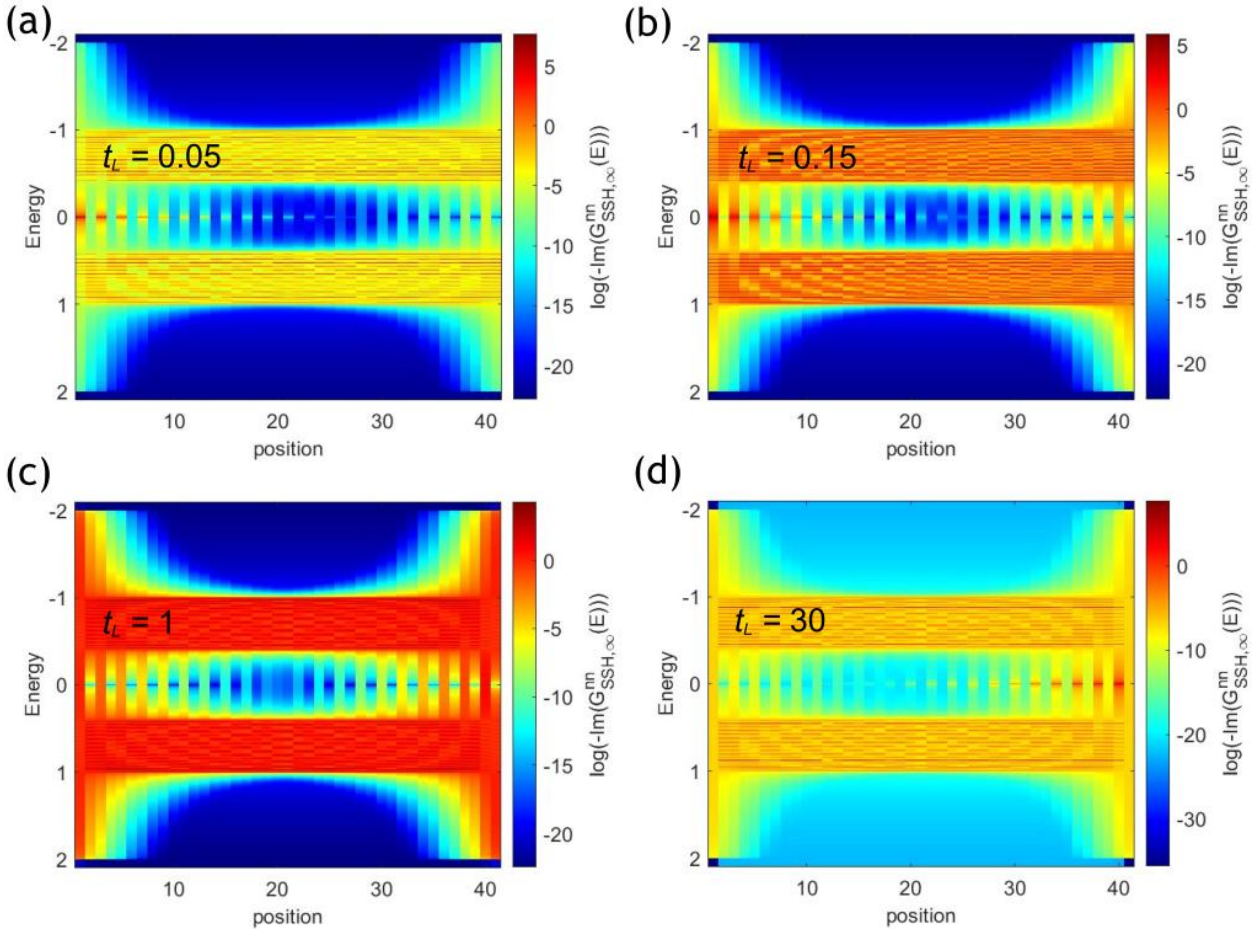

Figure 4.20 – LDOS over the spectrum of the SSH chain with two semi-infinite leads. Note the colormap is scaled to the logarithm of the LDOS to heighten contrasts. The SSH chain length is $N = 41$ with hopping parameters $t_1 = 0.3$ and $t_2 = 0.7$. The SSH chain edge state is localized on the left of the chain on odd sites, while the ghost state is localized on the right side and on even sites. Four subplots are shown for lead coupling strengths (a) $t_L = 0.05$, (b) $t_L = 0.15$, (c) $t_L = 1$, (d) $t_L = 30$.

we have imposed on the system; the lead hopping terms were normalized to unity. At this value of the coupling parameter, the edge state and ghost state have identical amplitudes as expected from (4.5.3). Finally, Fig. 4.20(d) shows suppression of the edge state in favor of the ghost state at large t_L. Note that, for large t_L, the ghost state is significantly less broadened and actually takes the form of an edge state at the mid-gap.

The proportionality of the LDOS to t_L for N even is much more complex because the left and right lead terms are of *inverse* proportionality to one another in (3.2.29). We find,

$$\text{for } N \text{ even} \quad \begin{cases} G^{nn}_{\text{SSH},\infty}(0) \propto \left[f_L\left(t_L^2\right) + f_R\left(1/t_L^2\right) \right]^{-1} & \text{for } n \text{ odd}, \\ G^{nn}_{\text{SSH},\infty}(0) \propto \left[f_L\left(1/t_L^2\right) + f_R\left(t_L^2\right) \right]^{-1} & \text{for } n \text{ even}, \end{cases} \tag{4.5.4}$$

where $f_{L,R}$ are terms originating from the left or right lead, respectively. Difficulties arise from the dependence on N, n, t_1, and t_2 in the full treatment of $f_{L,R}$. Qualitatively, the even-N Green's functions have diagonal elements that behave proportionally to t_L^2 up to a maximum before tapering as $1/t_L^2$. The DOS near zero energies is plotted in Fig. 4.21(a) for various t_L, and Fig. 4.21(b) shows the overall form of the DOS at $E = 0$ for continuous t_L. We can see from Fig. 4.21(a) that increasing the lead coupling initially increases the population density at $E = 0$. Simultaneously, we observe broadening of the DOS peaks. After the maximum is reached, the individual edge state peaks are no longer visible and only a wide broadened peak exists centered on $E = 0$. Increasing t_L further, we see a suppression of the DOS at $E = 0$ as expected. It is true that the explicit dependency of the localized mode amplitudes on t_L is complicated, yet the qualitative behaviours of edge states and ghost states is simpler than the odd-N case: In the $r < r_C$ phase, a pair of topological edge states exist $\forall\ t_L < 1$, and for $r > r_C$ a pair of ghost states exist $\forall\ t_L > 1$.

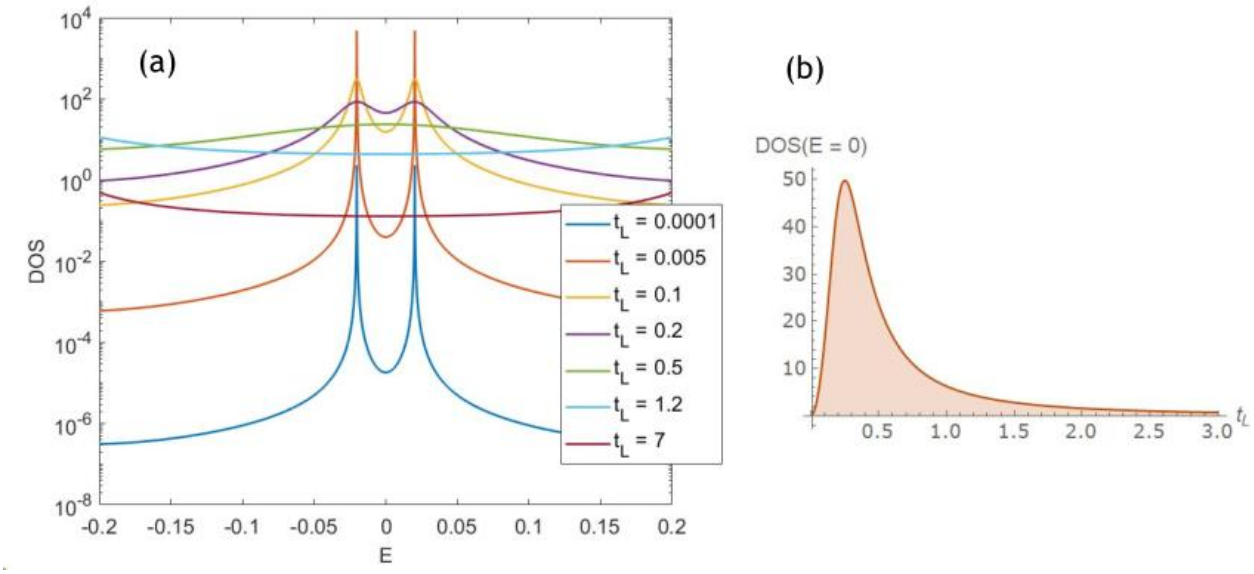

Figure 4.21 – Density of states as a function of the lead coupling parameters t_L for $N = 30$, $t_1 = 1/1.1$ and $t_2 = 1.1$. (a) shows the numerical DOS in the vicinity of $E = 0$ while (b) shows the magnitude of the DOS at $E = 0$ from the analytical expression for the Green's function.

This chapter has demonstrated the sensitivity of the decoherence probe to various localized modes that arise in our tripartite system. Through its rate proportionality to the LDOS, the decoherence probe can infer the presence of topological edge states while providing a complete spatial description of the state revealing the localization boundary and the penetration depth into the bulk of the edge state. We subsequently carried out an in-depth analysis of various system parameters and their impact on the probe, showing that it is possible to increase the sensitivity of the probe by fine-tuning the TLS eigenvalues or

by considering a single quantum dot probe, eliminating bulk-oscillatory contributions to the decay rate. A full treatment of the tripartite system prescribes a non-Hermitian description from the complex on-site potentials, leading to open system behaviours. We have seen how lead parameters t_L directly impact broadening of the DOS and, of notable importance, we have seen that interactions with leads resulted in the emergence of a nested $N-2$ subregion of the SSH chain featuring a distinct topology to the full SSH chain. Localized states on this segment have been dubbed *ghost* states in this work. We note that similar states were observed in [52, 53], although the authors do not discuss them.

Chapter 5

Conclusion and Outlook

This work began with a thorough review of the SSH model through a discussion and derivation of the model's solutions to the Schrödinger equation. We argued that the existence of localized modes, dubbed edge states, is necessary for a complete set of solutions and further went to demonstrate the topological nature of these states. Through the use of invariants, of which the SSH model has two ($\nu = 0,\ 1$), it is possible to predict the number of topological edge states in a system. We further discussed the implications of chiral symmetry on the model. Of importance to us were the following results: the energy spectrum is symmetric and zero-energy solutions are confined to a sublattice within the chain. The SSH model was chosen as a toy model for a topological material, serving as a proof of concept for a quantum sensor we have dubbed the decoherence probe.

In the second chapter of this work, we briefly discussed the notions of decoherence and Green's functions in order to derive an approximate expression for the time evolution of a double quantum dot (or TLS) decohering due to coupling to a general tight-binding environment. This involved the inclusion of self-energy terms to describe the exact dynamics within a finite region of an infinite system. Furthermore, the final expression for the decoherence rate (2.5.12) was derived in a weak-coupling approximation which was found necessary due to the energy dependence in a Fourier integral passing from frequency- to time-space for the Green's function. In order to study the decoherence rate expression, it became necessary to obtain an explicit form for the self-energy of an environment of interest. We then constructed a tripartite system consisting of a TLS coupled to a finite SSH chain sandwiched between semi-infinite leads. The energy-dependent Green's functions, and hence the self-energies, for the four possible configurations of the tripartite system were found in the third chapter.

With these analytical forms for the self-energies, a case study of the decoherence dynamics of a TLS coupled to an SSH chain environment was carried out in Chapter 4. Here, it was demonstrated that there exists a direct proportionality between the decoherence rate of

the TLS and the LDOS within the SSH chain of the tripartite system. Sweeping the topological material of interest with a TLS probe of appropriately tuned energy, we demonstrate the ability to characterize topological edge states of the SSH model through decoherence dynamics. The decoherence probe is sensitive to the presence (or absence) of edge states and determines the localization boundary of edge states as well as their spatial profile. We hope this novel quantum sensor can become a powerful platform for studying localized states in low-dimensional materials. Decoherence probe responses to variations in system parameters were subsequently studied. Of note, emergent localized states, dubbed ghost states, were observed corresponding to the simultaneous interplay of distinct topological phases due to lead-induced boundary effects. This last point is of interest for realistic systems as it hints at the ambiguity of topological invariant predictions when working in finite systems with interface effects. This concludes the material presented in this work. Future work and open questions are discussed below.

The probe's success at detecting edge states has been demonstrated in this work. A straightforward generalization of the probe's application could involve the study of an SSH chain featuring a topological defect, or soliton. It is expected that localized modes can exist in such a chain, with states localizing at the chain boundaries and at the domain wall, providing a rich variety of states to study. Preliminary work analyzing solutions to SSH chains with a central soliton has been carried out with predictions in agreement with an analogous topological spin-chain model [55]. Interesting considerations also arise in trying to reconcile the localized features of the finite and infinite SSH chain with a central soliton. We stress again that this probe is applicable to a wide array of systems from the general form of (2.5.12) which describes the decoherence rate for couplings to a generic environment with self-energy Σ_R^{nn}. As such, the probe should be sensitive to localized states in other one-dimensional models such as the Kitaev chain. Furthermore, the probe easily generalizes to two-dimensional materials. In such systems, a scan of the area by way of the probe would allow for the characterization of edge modes and their penetration depth into the bulk, with the possibility of probing more exotic topological excitations such as corner modes.

Absolutely critical to explore following this work are the multiple questions that have arisen from open system considerations. While it is true only real values of energy are relevant for input to the decoherence probe, accurately predicting the states that arise in our tripartite system requires an understanding of the full non-Hermitian dynamics of the open system. Preliminary explorations hint at the existence of bifurcations and exceptional points with coalescing eigenstates observed as a function of the coupling of the SSH chain to the leads, $t_{L,R}$. Similar features were studied and documented in works on dissipative extensions to the SSH model [51, 56, 57]. A surprising feature of this open system we have studied is the existence of ghost states. These ghost states are not predicted by the topological invariants of the standard periodic SSH model even though they behave similarly

to the pure SSH chain edge states. This highlights the importance of considering topological invariants which can be applied to finite and open systems. At the very least, it shows the importance of being cautious in applying rigorous bulk-periodic topological invariants to finite open systems. Recent work on the bulk-boundary correspondence of non-Bloch and non-Hermitian systems can be found in [58, 59]. We stress here that the only non-Hermitian terms in the tripartite system arise at the boundaries and the bulk SSH Hamiltonian is Hermitian. Due to this, there is no clear non-Hermitian topological invariant that arises from the bulk. More specifically, there exist works on the topological invariants of dissipative SSH models: considering non-Hermitian staggered hopping parameters [60, 61], and for finite open system featuring boundary potentials [51, 56]. Importantly, we note that the similar systems studied in [51, 56] differ from the tripartite system in an important way: boundary terms are taken as gain and loss sites $\pm i\gamma$, while our dissipative description is energy-dependent and considers the exact self-energy of the semi-infinite leads. There is hope that the field of topological photonics, being inherently non-Hermitian, will propel our knowledge of non-Hermitian topological phases of matter. In the near future, the inclusion of these open system topological invariants should allow for a complete topological phase classification of the localized states we observe through the decoherence probe. Simultaneously, this should inform us whether ghost states are novel topological features or if they represent a migration of the conventional SSH chain edge states as a result of boundary interactions.

In working on this project, it became evident that the decoherence probe shares some important similarities with scanning tunneling microscopy (STM), with both methods probing the LDOS of a sample. It would be interesting to determine if certain experimental contexts favor a decoherence probe over an STM setup. Additionally, it will be important to elaborate further on differences between the two techniques to truly appreciate what additional information can be gained from the decoherence probe. Notably, it would be interesting to see if configurations of the TLS parameters such that $(\tau_\phi)^{-1}$ is no longer strictly proportional to the LDOS can lead to new observable phenomena (i.e. when δ' contributions are no longer linearly proportional to $\mathrm{Im}\{\Sigma^{nn}_{\mathrm{SSH},\infty}\}$; see Section 4.1). Another approach to diversifying the probe's utility could involve some form of periodic driving of the TLS or charge pumping [62]. The decoherence probe, in any case, remains a fascinating means of exploring quantum-classical transitions to extract information on the decohering subsystem's environment.

References

[1] A. J. Leggett et al. "Dynamics of the dissipative two-state system". In: *Rev. Mod. Phys.* 59 (1 Jan. 1987), pp. 1–85. DOI: 10.1103/RevModPhys.59.1. URL: https://link.aps.org/doi/10.1103/RevModPhys.59.1.

[2] C.-K. Chiu et al. "Classification of topological quantum matter with symmetries". In: *Rev. Mod. Phys.* 88 (3 Aug. 2016), p. 035005. DOI: 10.1103/RevModPhys.88.035005. URL: https://link.aps.org/doi/10.1103/RevModPhys.88.035005.

[3] S. Bohling et al. "Thermoelectric performance of topological boundary modes". In: *Phys. Rev. B* 98 (3 July 2018), p. 035132. DOI: 10.1103/PhysRevB.98.035132. URL: https://link.aps.org/doi/10.1103/PhysRevB.98.035132.

[4] M. P. Anantram, M. S. Lundstrom, and D. E. Nikonov. "Modeling of Nanoscale Devices". In: *Proceedings of the IEEE* 96.9 (2008), pp. 1511–1550. DOI: 10.1109/JPROC.2008.927355.

[5] M. Zaimi et al. "Detecting topological edge states with the dynamics of a qubit". In: *Physics Letters A* 388 (2021), p. 127035. ISSN: 0375-9601. DOI: https://doi.org/10.1016/j.physleta.2020.127035. URL: https://www.sciencedirect.com/science/article/pii/S0375960120309026.

[6] N. R. Cooper, J. Dalibard, and I. B. Spielman. "Topological bands for ultracold atoms". In: *Rev. Mod. Phys.* 91 (1 Mar. 2019), p. 015005. DOI: 10.1103/RevModPhys.91.015005. URL: https://link.aps.org/doi/10.1103/RevModPhys.91.015005.

[7] T. Ozawa et al. "Topological photonics". In: *Rev. Mod. Phys.* 91 (1 Mar. 2019), p. 015006. DOI: 10.1103/RevModPhys.91.015006. URL: https://link.aps.org/doi/10.1103/RevModPhys.91.015006.

[8] F. Klauck, M. Heinrich, and A. Szameit. "Photonic two-particle quantum walks in Su–Schrieffer–Heeger lattices". In: *Photon. Res.* 9.1 (Jan. 2021), A1–A7. DOI: 10.1364/PRJ.409005. URL: http://www.osapublishing.org/prj/abstract.cfm?URI=prj-9-1-A1.

[9] P. St-Jean et al. "Lasing in topological edge states of a one-dimensional lattice". In: *Nature Photonics* 11 (10 2017), pp. 651–656. DOI: 10.1038/s41566-017-0006-2. URL: https://doi.org/10.1038/s41566-017-0006-2.

[10] A. Ghatak et al. “Observation of non-Hermitian topology and its bulk–edge correspondence in an active mechanical metamaterial”. In: *Proceedings of the National Academy of Sciences* 117.47 (2020), pp. 29561–29568. ISSN: 0027-8424. DOI: 10.1073/pnas.2010580117. eprint: https://www.pnas.org/content/117/47/29561.full.pdf. URL: https://www.pnas.org/content/117/47/29561.

[11] W. P. Su, J. R. Schrieffer, and A. J. Heeger. “Solitons in Polyacetylene”. In: *Phys. Rev. Lett.* 42 (25 June 1979), pp. 1698–1701. DOI: 10.1103/PhysRevLett.42.1698. URL: https://link.aps.org/doi/10.1103/PhysRevLett.42.1698.

[12] W. P. Su, J. R. Schrieffer, and A. J. Heeger. “Soliton excitations in polyacetylene”. In: *Phys. Rev. B* 22 (4 Aug. 1980), pp. 2099–2111. DOI: 10.1103/PhysRevB.22.2099. URL: https://link.aps.org/doi/10.1103/PhysRevB.22.2099.

[13] A. J. Heeger et al. “Solitons in conducting polymers”. In: *Rev. Mod. Phys.* 60 (3 July 1988), pp. 781–850. DOI: 10.1103/RevModPhys.60.781. URL: https://link.aps.org/doi/10.1103/RevModPhys.60.781.

[14] S.A. Kivelson. “Electron fractionalization”. In: *Synthetic Metals* 125.1 (2001). Celebrating the year 2000 Nobel prize in Chemistry for the discovery and development of conducting polymers, pp. 99–106. ISSN: 0379-6779. DOI: https://doi.org/10.1016/S0379-6779(01)00516-1. URL: https://www.sciencedirect.com/science/article/pii/S0379677901005161.

[15] J. K. Asbóth, L. Oroszlány, and Pályi A. *A Short Course on Topological Insulators*. Springer International Publishing, 2016, pp. 1–39.

[16] R. E. Peierls. *Quantum Theory of Solids*. Oxford : Clarendon Press, 1955.

[17] P. Delplace, D. Ullmo, and G. Montambaux. “Zak phase and the existence of edge states in graphene”. In: *Phys. Rev. B* 84 (19 Nov. 2011), p. 195452. DOI: 10.1103/PhysRevB.84.195452. URL: https://link.aps.org/doi/10.1103/PhysRevB.84.195452.

[18] K. v. Klitzing, G. Dorda, and M. Pepper. “New Method for High-Accuracy Determination of the Fine-Structure Constant Based on Quantized Hall Resistance”. In: *Phys. Rev. Lett.* 45 (6 Aug. 1980), pp. 494–497. DOI: 10.1103/PhysRevLett.45.494. URL: https://link.aps.org/doi/10.1103/PhysRevLett.45.494.

[19] W. Jing and S.-C. Zhang. “Topological states of condensed matter”. In: *Nature Materials* 16 (2013), pp. 1062–1067. DOI: https://doi.org/10.1038/nmat5012.

[20] M.G. Vergniory et al. *All Topological Bands of All Stoichiometric Materials*. 2021. arXiv: 2105.09954 [cond-mat.mtrl-sci].

[21] M.G. Vergniory et al. “A complete catalogue of high-quality topological materials”. In: *Nature* 566 (2019), pp. 480–485. DOI: https://doi.org/10.1038/s41586-019-0954-4.

[22] A. Kitaev. "Unpaired Majorana fermions in quantum wires". In: *Physics-Uspekhi* 44.10S (Oct. 2001), pp. 131–136. DOI: 10.1070/1063-7869/44/10s/s29. URL: https://doi.org/10.1070/1063-7869/44/10s/s29.

[23] J. Cayssol. "Introduction to Dirac materials and topological insulators". In: *Comptes Rendus Physique* 14.9 (2013), pp. 760–778. ISSN: 1631-0705. DOI: https://doi.org/10.1016/j.crhy.2013.09.012. URL: https://www.sciencedirect.com/science/article/pii/S163107051300145X.

[24] B.-H. Chen and D.-W. Chiou. "An elementary rigorous proof of bulk-boundary correspondence in the generalized Su-Schrieffer-Heeger model". In: *Physics Letters A* 384.7 (2020), p. 126168. ISSN: 0375-9601. DOI: https://doi.org/10.1016/j.physleta.2019.126168. URL: https://www.sciencedirect.com/science/article/pii/S0375960119311028.

[25] C. Kittel. *Introduction to Solid State Physics*. 8th ed. Wiley, 2004. ISBN: 9780471415268. URL: http://www.amazon.com/Introduction-Solid-Physics-Charles-Kittel/dp/047141526X/ref=dp_ob_title_bk.

[26] M. V. Berry. "Quantal phase factors accompanying adiabatic changes". In: *Proceedings of the Royal Society of London. Series A, Mathematical and Physical Sciences* 392.1802 (1984), pp. 45–57.

[27] Y. Aharonov and D. Bohm. "Significance of Electromagnetic Potentials in the Quantum Theory". In: *Phys. Rev.* 115 (3 Aug. 1959), pp. 485–491. DOI: 10.1103/PhysRev.115.485. URL: https://link.aps.org/doi/10.1103/PhysRev.115.485.

[28] M. Atala et al. "Direct measurement of the Zak phase in topological Bloch bands". In: *Nature Physics* 9 (12 2013), pp. 795–800. DOI: 10.1038/nphys2790. URL: https://doi.org/10.1038/nphys2790.

[29] R. S. K. Mong and V. Shivamoggi. "Edge states and the bulk-boundary correspondence in Dirac Hamiltonians". In: *Phys. Rev. B* 83 (12 Mar. 2011), p. 125109. DOI: 10.1103/PhysRevB.83.125109. URL: https://link.aps.org/doi/10.1103/PhysRevB.83.125109.

[30] I. Mondragon-Shem et al. "Topological Criticality in the Chiral-Symmetric AIII Class at Strong Disorder". In: *Phys. Rev. Lett.* 113 (4 July 2014), p. 046802. DOI: 10.1103/PhysRevLett.113.046802. URL: https://link.aps.org/doi/10.1103/PhysRevLett.113.046802.

[31] B. Michen, T. Micallo, and J. C. Budich. "Exceptional non-Hermitian phases in disordered quantum wires". In: *Phys. Rev. B* 104 (3 July 2021), p. 035413. DOI: 10.1103/PhysRevB.104.035413. URL: https://link.aps.org/doi/10.1103/PhysRevB.104.035413.

[32] H. Bruus and K. Flensberg. *Many-body quantum theory in condensed matter physics : an introduction*. Oxford University Press, 2004.

[33] A. Ludwig. "Topological phases: classification of topological insulators and superconductors of non-interacting fermions, and beyond". In: *Physica Scripta* T168 (Dec. 2015), p. 014001. DOI: 10.1088/0031-8949/2015/t168/014001.

[34] T. Liu and H. Guo. "Topological phase transition in the quasiperiodic disordered Su–Schriffer–Heeger chain". In: *Physics Letters A* 382.45 (2018), pp. 3287–3292. ISSN: 0375-9601. DOI: https://doi.org/10.1016/j.physleta.2018.09.023. URL: https://www.sciencedirect.com/science/article/pii/S0375960118309836.

[35] L. Li, Z. Xu, and S. Chen. "Topological phases of generalized Su-Schrieffer-Heeger models". In: *Phys. Rev. B* 89 (8 Feb. 2014), p. 085111. DOI: 10.1103/PhysRevB.89.085111. URL: https://link.aps.org/doi/10.1103/PhysRevB.89.085111.

[36] M. Scollon and M. P. Kennett. "Persistence of chirality in the Su-Schrieffer-Heeger model in the presence of on-site disorder". In: *Phys. Rev. B* 101 (14 Apr. 2020), p. 144204. DOI: 10.1103/PhysRevB.101.144204. URL: https://link.aps.org/doi/10.1103/PhysRevB.101.144204.

[37] A. Kitaev. "Fault-tolerant quantum computation by anyons". In: *Annals of Physics* 303.1 (2003), pp. 2–30. ISSN: 0003-4916. DOI: https://doi.org/10.1016/S0003-4916(02)00018-0. URL: https://www.sciencedirect.com/science/article/pii/S0003491602000180.

[38] L. Landau. "Das D¨ampfungsproblem in der Wellenmechanik". In: *Z. Phys.* 45 (1927), pp. 430–441. URL: http://verga.cpt.univ-mrs.fr/pdfs/Landau-1927.pdf.

[39] N. F. Mott. "The wave mechanics of α-Ray tracks". In: *Royal Society London A* 126 (1929), pp. 79–84.

[40] D. J. W. Giulini et al. *Decoherence and the Appearance of a Classical World in Quantum Theory*. Springer-Verlag Berlin Heidelberg, 2003.

[41] E. Joos and H.D. Zeh. "The emergence of classical properties through interaction with the environment". In: *Z. Physik B - Condensed Matter* 59 (1985), pp. 223–243. DOI: 10.1007/BF01725541.

[42] W. H. Zurek. "Decoherence, einselection, and the quantum origins of the classical". In: *Rev. Mod. Phys.* 75 (3 May 2003), pp. 715–775. DOI: 10.1103/RevModPhys.75.715. URL: https://link.aps.org/doi/10.1103/RevModPhys.75.715.

[43] C. Kiefer and E. Joos. "Decoherence: Concepts and examples". In: *Quantum Future From Volta and Como to the Present and Beyond*. Ed. by P. Blanchard and A. Jadczyk. Berlin, Heidelberg: Springer Berlin Heidelberg, 1999, pp. 105–128. ISBN: 978-3-540-49482-9.

[44] E. N. Economou. *Green's Functions in Quantum Physics*. 3rd ed. Springer-Verlag Berlin Heidelberg, 2006. ISBN: 9783540-288411.

[45] V. S. Vladimirov. *Equations of Mathematical Physics*. Marcel Dekker INC, 1971. ISBN: 0-8247-1713-9.

[46] J. H. Davies. *The Physics of Low-dimensional Semiconductors: An Introduction*. Cambridge University Press, 1997. DOI: 10.1017/CBO9780511819070.

[47] S. Datta. *Quantum Transport: Atom to Transistor*. Cambridge University Press, 2005. DOI: 10.1017/CBO9781139164313.

[48] H. Eleuch, M. Hilke, and R. MacKenzie. "Probing Anderson localization using the dynamics of a qubit". In: *Phys. Rev. A* 95 (6 June 2017), p. 062114. DOI: 10.1103/PhysRevA.95.062114. URL: https://link.aps.org/doi/10.1103/PhysRevA.95.062114.

[49] Z. Yan. "Majorana corner and hinge modes in second-order topological insulator/superconductor heterostructures". In: *Phys. Rev. B* 100 (20 Nov. 2019), p. 205406. DOI: 10.1103/PhysRevB.100.205406. URL: https://link.aps.org/doi/10.1103/PhysRevB.100.205406.

[50] S. Garmon, M. Gianfreda, and N. Hatano. "Bound states, scattering states, and resonant states in $\mathcal{PT}$-symmetric open quantum systems". In: *Phys. Rev. A* 92 (2 Aug. 2015), p. 022125. DOI: 10.1103/PhysRevA.92.022125. URL: https://link.aps.org/doi/10.1103/PhysRevA.92.022125.

[51] F. Dangel et al. "Topological invariants in dissipative extensions of the Su-Schrieffer-Heeger model". In: *Phys. Rev. A* 98 (1 July 2018), p. 013628. DOI: 10.1103/PhysRevA.98.013628. URL: https://link.aps.org/doi/10.1103/PhysRevA.98.013628.

[52] L. Jin, P. Wang, and Z. Song. "Su-Schrieffer-Heeger chain with one pair of $\mathcal{PT}$-symmetric defects." In: *Scientific Reports* 7 (2017), p. 5903. DOI: 10.1038/s41598-017-06198-9.

[53] A. M. Marques and R. G. Dias. "Multihole edge states in Su-Schrieffer-Heeger chains with interactions". In: *Phys. Rev. B* 95 (11 Mar. 2017), p. 115443. DOI: 10.1103/PhysRevB.95.115443. URL: https://link.aps.org/doi/10.1103/PhysRevB.95.115443.

[54] N. Hatano et al. "Some Properties of the Resonant State in Quantum Mechanics and Its Computation". In: *Progress of Theoretical Physics* 119.2 (Feb. 2008), pp. 187–222. ISSN: 0033-068X. DOI: 10.1143/PTP.119.187. eprint: https://academic.oup.com/ptp/article-pdf/119/2/187/5299805/119-2-187.pdf. URL: https://doi.org/10.1143/PTP.119.187.

[55] M. Estarellas, I. D'Amico, and T. Spiller. "Topologically protected localised states in spin chains". In: *Scientific Reports* 7 (42904 2017). DOI: 10.1038/srep42904.

[56] B. Ostahie and A. Aldea. "Spectral analysis, chiral disorder and topological edge states manifestation in open non-Hermitian Su-Schrieffer-Heeger chains". In: *Physics Letters A* 387 (Jan. 2021), p. 127030. ISSN: 0375-9601. DOI: 10.1016/j.physleta.2020.127030. URL: http://dx.doi.org/10.1016/j.physleta.2020.127030.

[57] D. Leykam et al. “Edge Modes, Degeneracies, and Topological Numbers in Non-Hermitian Systems”. In: *Phys. Rev. Lett.* 118 (4 Jan. 2017), p. 040401. DOI: 10.1103/PhysRevLett.118.040401. URL: https://link.aps.org/doi/10.1103/PhysRevLett.118.040401.

[58] K.-I. Imura and Y. Takane. “Generalized Bloch band theory for non-Hermitian bulk–boundary correspondence”. In: *Progress of Theoretical and Experimental Physics* 2020.12 (Sept. 2020). 12A103. ISSN: 2050-3911. DOI: 10.1093/ptep/ptaa100. eprint: https://academic.oup.com/ptep/article-pdf/2020/12/12A103/35611802/ptaa100.pdf. URL: https://doi.org/10.1093/ptep/ptaa100.

[59] K. Yokomizo and S. Murakami. “Non-Bloch Band Theory of Non-Hermitian Systems”. In: *Phys. Rev. Lett.* 123 (6 Aug. 2019), p. 066404. DOI: 10.1103/PhysRevLett.123.066404. URL: https://link.aps.org/doi/10.1103/PhysRevLett.123.066404.

[60] F. K. Kunst et al. “Biorthogonal Bulk-Boundary Correspondence in Non-Hermitian Systems”. In: *Phys. Rev. Lett.* 121 (2 July 2018), p. 026808. DOI: 10.1103/PhysRevLett.121.026808.

[61] S. Yao and Z. Wang. “Edge States and Topological Invariants of Non-Hermitian Systems”. In: *Phys. Rev. Lett.* 121 (8 Aug. 2018), p. 086803. DOI: 10.1103/PhysRevLett.121.086803.

[62] M. Kurzyna and T. Kwapiński. “Electron Pumping and Spectral Density Dynamics in Energy-Gapped Topological Chains”. In: *Applied Sciences* 11.2 (2021). ISSN: 2076-3417. DOI: 10.3390/app11020772. URL: https://www.mdpi.com/2076-3417/11/2/772.